# Atomistic modelling of dislocation glide and pinning in iron and carbon steel

Arnaud Allera

N°d'ordre NNT : 2021LYSE1293

**THESE de DOCTORAT DE L'UNIVERSITE DE LYON**
opérée au sein de
**l'Université Claude Bernard Lyon 1**

**Ecole Doctorale** N° 52
**Physique et Astrophysique**

**Spécialité de doctorat** : Physique

Soutenue publiquement le 15/12/2021, par :
**Arnaud Allera**

---

# Modélisation atomistique du glissement et de l'ancrage des dislocations dans les aciers ferritiques Fe-C

---

Devant le jury composé de :

| | | |
|---|---|---|
| Becquart, Charlotte | Professeure, Université de Lille | Rapporteure |
| Clouet, Emmanuel | Chercheur CEA, CEA-SRMP | Rapporteur |
| Colombani, Jean | Professeur, Université Lyon 1 | Examinateur |
| Curtin, William | Professeur, EPFL | Examinateur |
| Varvenne, Céline | Chargée de recherche, Aix-Marseille Université | Examinateur |
| Ribeiro, Fabienne | Chercheure IRSN, PSN-RES/SEMIA/LSMA | Examinateur |
| | | |
| Rodney, David | Professeur, Université Lyon 1 | Directeur de thèse |
| Perez, Michel | Professeur, INSA Lyon | Co-directeur de thèse |

# Atomistic modelling of dislocation glide and pinning in iron and carbon steel

Arnaud Allera

2021

# Contents

# Sur les épaules de géants...

Avoir l'opportunité de rédiger une thèse sur un sujet scientifique pointu (et passionnant) est un privilège rare, rendu possible par un environnement exceptionnel. Je suis reconnaissant envers ces inconnus qui sans le savoir m'ont soutenu (et financé) dans un parcours vers le métier qui m'attirait, et m'ont fait confiance pendant trois ans pour tâcher de découvrir quelque chose d'utile. D'autres m'ont fait le privilège supplémentaire de m'y aider sciemment, en me donnant de leur temps, de leur savoir ou de leur soutien ; je veux les remercier dans ces quelques lignes.

En la matière, ma première pensée va à mes encadrants, qui m'ont formé, conseillé, encouragé —et plus encore qui m'ont aidé à tenir la barre face à la pandémie. David : sans surprise, cette thèse contient beaucoup de ce qui fait ton ADN et je suis fier d'avoir fait ce chemin avec toi. Merci pour ta patience et ton courage face à cette thèse qui ne marchait *jamais* comme on l'attendait, face à ces potentiels qui ne sont *jamais* là où on les attend. Merci aussi pour ta pédagogie grâce à laquelle j'ai tant appris, ta rigueur à laquelle n'échappe aucun détail et aucun indice, ton envie de toujours aller plus loin. Michel : celui par lequel tout a commencé, qui voit de vraies personnes là où d'autres ne voient que des étudiants un peu perdus. Il est clair que tu as été là à tous les moments clés depuis mes premiers pas dans le supérieur, et que tu as cru en moi dès le début. Tu m'as appris à prendre de la hauteur, à savoir lever la tête du guidon (sans venir aux sorties vélo), à toujours rester humble. Je te dois beaucoup. Fabienne : merci de nous avoir accompagnés tout au long de ce projet. Nos discussions ont été des jalons indispensables, l'occasion de prendre du recul, de se recentrer, de trouver de nouvelles pistes grâce à tes fameuses questions, exigeantes mais toujours pertinentes. Je me souviendrai aussi de la bienveillace dont tu as toujours fait preuve. Je tiens également à remercier Tom, pour ton aide sur une partie aussi imprévue que passionnante, que j'ai beaucoup aimé explorer. Merci d'être venu enrichir cette thèse avec tes idées (et ton humour !) et d'avoir donné de ton temps pour m'aider avec PAFI !

Je souhaite ensuite remercier les membres de mon jury, dont les travaux ont m'ont beaucoup inspiré et qui m'ont fait l'honneur d'évaluer mon travail.

Je remercie également mes collègues de l'IRSN, de toutes disciplines, pour les échanges

très enrichissants (et trop rares !).

Je veux aussi remercier Sébastien et ses collègues du CCIN2P3 pour leur aide et leurs conseils très précieux.

Viennent ensuite les compagnons de galère. Merci à mes co-bureaux ; Antoine, qui m'a appris à gravir les paysages énergétiques (comme l'alpiniste de la photo), Manon et Ce pour les souvenirs de notre repas de Noël, Maxime, qui fait toujours des bêtises : *arigato* pour le scooter et la fanfare asiatique ; Theophile, certifié résistant aux ouragans, merci pour les Jacobins et les paquitos. Merci Laurabelle d'avoir partagé un été de rédaction dans le confort des Algeco. Je dois aussi remercier une bande de docteurs partis avant moi : Alexis, pour les potins sur tu-sais-qui, Aurélien pour les posters, Gwenaëlle pour les galettes des rois et pour ses conseils charte graphique (que je n'ai pas suivi), Alexandre pour les invitations à l'escalade et Justine pour sa bonne humeur inébranlable. Merci à tous ceux qui font de MétAl une équipe si agréable, et pour ne citer qu'eux, à Pierre-Antoine, Patrice et à Jean-Yves (tes mails me manquent déjà), Éric, et aussi aux lutins de Noël. Merci aussi aux inombrables copains dans les autres équipes de MATÉIS , et en particulier à Mathilde qui a tant fait pour nous, et à Carmen, trois mois c'était trop court !

Merci à mes amis qui ne font *pas* de thèse d'avoir été là pour me rappeler que le monde ne s'est pas arrêté de tourner pendant ce temps. Merci à John pour les water-polo, à Numa pour les flams (et les blattes), à Thibaut pour le duo de sauces, à Camille pour les déguisements, à Alexandre pour la règle des tiers, à Majda pour les chocolats chauds, à Audrey pour les guêpes, et à Clarisse pour le phénix. Merci aussi à Pierre et Romain (sans qui je n'aurais jamais appris Python) d'être là depuis si longtemps, et d'avoir été mes encadrants dans ma 2ème thèse, celle sur le Covid. Merci à Solen pour le harcèlement téléphonique, pour les recettes *healthy*, et d'être toujours de mon côté (même quand on n'est pas d'accord).

Pour finir, je remercie bien-sûr ma famille. Merci à mes parents d'avoir toujours cultivé notre curiosité, de l'avoir aidée à mûrir, et d'avoir toujours été là pour m'épauler. Je veux remercier aussi ma sœur, qui me montre la voie dans le monde des grands depuis le début et avec qui je continue de grandir (je te rattraperai !). Merci enfin Marco pour tes conseils ; sur la thèse, mais aussi sur l'extraction du café qui m'a permis de l'écrire.

# Summary

Ferritic steels, made of a body-centered cubic (bcc) iron matrix with interstitial carbon solutes, are widely-used structural materials. However, the atomic-scale mechanisms which control their plasticity are still only partially understood. At low temperature, the plastic deformation of bcc metals is controlled by the mobility of the screw dislocations, which is hindered by both a strong resistance of the lattice itself, and the presence of other crystal defects, among which are solute atoms.

Atomic-scale models of dislocation mobility based on the Transition State Theory (TST) constitute a useful framework to model plastic flow in pure metals and in alloys. However, the approximations often used (harmonic approximation, constant activation entropy) yield poor predictions in iron. We used the recent *projected average force integrator* method to compute the activation free enthalpy for kink pair nucleation, including anharmonic effects. The data show that the harmonic regime is limited to very low temperatures, below 20 K. Non-linearities remain small below 100 K, allowing to compute an effective activation entropy, which increases when the activation enthalpy decreases, corresponding to an inverse Meyer-Neldel behavior. Integrating these effects in dislocation mobility models greatly improves the agreement with direct molecular dynamics (MD) simulations.

Extensions to Fe-C alloys are limited by the realism of the interatomic potentials available for this system. To address this issue, we combined two existing empirical potentials for Fe and Fe-C to reproduce both the Peierls mechanism and the carbon-induced screw dislocation core reconstruction found in *ab initio* calculations. Using this hybrid potential, MD simulations of the glide of screw dislocations in random solid solutions confirm a strong solute strengthening, caused by complex short-ranged interaction processes. We also considered an idealized geometry where a screw dislocation interacts with a row of carbon atoms. Combining MD simulations and saddle-point search methods, we unveil a very strong pinning when the solute separation is below about 100 Burgers vectors. This effect is due to the necessity to nucleate two consecutive kink pairs on the screw dislocation, with the second kink pair having a markedly increased activation enthalpy. We developed a harmonic TST model of this process that also integrates the entropic effects observed in pure iron, which yields a

good agreement with MD simulations conducted up to 300 K. This work provides elementary processes and parameters that will be useful for larger-scale models and in particular kinetic Monte Carlo simulations.

# Résumé

Les aciers ferritiques, constitués d'une matrice de fer cubique centré (CC) avec des solutés de carbone interstitiels, sont des matériaux de structure largement utilisés. Pourtant, les mécanismes qui contrôlent leur plasticité à l'échelle atomique ne sont encore que partiellement compris. A basse température, la déformation plastique des métaux CC est contrôlée par la mobilité des dislocations vis, qui est limitée à la fois par une forte résistance du réseau lui-même, et par la présence d'autres défauts cristallins, dont notamment les atomes de soluté.

Les modèles de mobilité des dislocations à l'échelle atomique basés sur la théorie de l'état de transition (TET) fournissent un cadre pour modéliser la déformation plastique des métaux purs et de leurs alliages. Cependant, les approximations couramment utilisées pour appliquer ces modèles (approximation harmonique, entropie d'activation constante) donnent de médiocres résultats dans le fer. Nous avons calculé l'enthalpie libre d'activation pour la nucléation de paires de crans grâce à la récente méthode *projected average force integrator*, qui permet de prendre en compte les effets anharmoniques. Les données indiquent que le régime harmonique est limité à des températures très basses, inférieures à 20 K. Les non-linéarités restent faibles en dessous de 100 K, permettant de calculer une entropie d'activation effective, qui augmente lorsque l'enthalpie d'activation diminue, ce qui correspond à un comportement Meyer-Neldel inverse. L'intégration de ces effets dans les modèles de mobilité des dislocations améliore considérablement l'accord avec les simulations de dynamique moléculaire (DM).

L'application de ces approches aux alliages Fe-C demeure limitée par le réalisme des potentiels interatomiques disponibles pour ce système. Pour résoudre ce problème, nous avons combiné deux potentiels empiriques existants pour Fe et Fe-C afin de reproduire à la fois le mécanisme de Peierls et la reconstruction des coeurs de dislocation vis en présence de carbone mise en évidence par des calculs *ab initio*. Des simulations de DM du glissement d'une dislocation vis dans une solution solide aléatoire utilisant ce potentiel confirment un fort durcissement, causé par des processus complexes d'interaction à courte distance entre dislocation et solutés. Nous avons également étudié une géométrie idéalisée où une dislocation vis interagit avec une rangée d'atomes de carbone. En combinant des simulations de DM et des méthodes de recherche de point-col, nous dévoilons un très fort ancrage lorsque

la séparation des solutés est inférieure à environ 100 vecteurs de Burgers. Cet effet est dû à la nécessité de nucléer deux paires de cran consécutivement sur la dislocation, la deuxième paire ayant une enthalpie d'activation nettement augmentée. Nous avons développé un modèle de ce processus basé sur la TET harmonique, qui intègre également les effets entropiques observés dans le fer pur, en bon accord avec les simulations de DM menées jusqu'à 300 K. Ce travail fournit des processus et des paramètres élémentaires qui seront utiles pour des modèles à plus grande échelle et en particulier des simulations Monte Carlo cinétique.

# 0 Introduction

## 0.1 Ageing of nuclear reactor vessels

Nuclear power is widely regarded as a low-carbon emission method of electricity generation (Lenzen, 2008; Warner and Heath, 2012). Compared to fossile fuels, which are used for 60% of worldwide electricity production (see Fig. 0.1) and account for a large part of global greenhouse gas emissions, nuclear energy could contribute to the mitigation of global climate change and air pollution (Kharecha and Hansen, 2013). While the benefit of new investments in nuclear power compared to renewable energies is still debated (Sovacool et al., 2020), it has become clear that leveraging existing nuclear power capacity can help reach greenhouse gas reduction goals. However, this might be challenged by the limited lifetime of nuclear reactors, often estimated as 50–60 years (Ballesteros et al., 2012). In France for example, existing reactors have been exploited for 19 to 41 years, with a median age of 36 years (IAEA, 2019). Reactor closure would result in a reduction in electric production capacity, likely compensated by a massive use of fossile fuels —which would in turn increase greenhouse gas emissions. Instead, operation should be prolonged to more than 50 years to buy time as energetic transition and renewable deployment are ramping up (Mainsant, 2018). The possiblity of extending the lifetime of existing nuclear power plants has thus become a burning issue in the face of climate change emergency (Pachauri et al., 2014) and ubiquitous calls to cut greenhouse gas emissions.

The main component of pressurized water reactors (PWR) is their vessel, made of 330–520 tons of ferritic steel (depending on the generation of the reactor) and housing the reactor core, which cannot be replaced at a reasonable cost. The integrity of the vessel can therefore be the limiting feature for the PWR operation lifetime. The vessel is also an essential safety component, as it acts as the second barrier of containment of radioactive material. One key aspect is thus to make sure that safety margins used for PWRs design remain valid, including in the conditions of an accident. Material properties can be computed experimentally and their evolution monitored, but investigating all relevant conditions is costly and difficult, es-

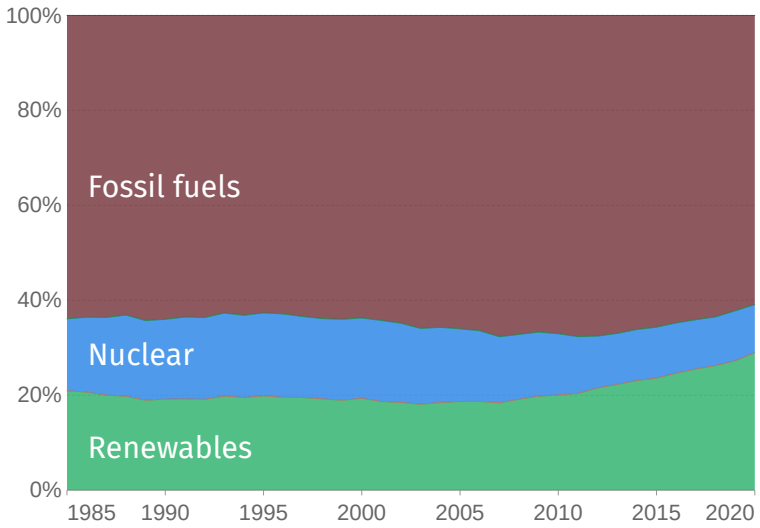


Figure 0.1: **Share of the world total electricity production from fossil fuels, nuclear and renewables**. Source: Our World in Data based on BP Statistical Review of World Energy & Ember (2021)

pecially for accidental conditions. The use of physical models to extend empirical approaches is therefore growing (CEA-DEN, 2014).

Vessel steel is subject to thermal ageing and irradiation during operation, which cause strengthening, *i.e.* an increase of the yield stress, and an embrittlement that reduces its ability to deform plastically under a high mechanical load. The yield stress increase and loss of ductility that characterize irradiation hardening are illustrated in Fig. 0.2. The creation of irradiation defects involves a number of mechanisms at the atomic scale: the impact of an energetic particule results in a cascade of atomic displacements, and the formation of residual point defects (*i.e.* the *primary damage*) (Becquart et al., 2021); new defects interact with existing microstructural defects (*e.g.* dislocations, solutes), possibly affecting their mobility (Zamzamian et al., 2019); and the accumulation or diffusion of these defects can create strong obstacles to dislocation motion (*e.g.* precipitates, dislocation loops) that cause hardening (Tipping, 2010). On the other hand, thermal ageing allows the diffusion of interstitial solutes, such as carbon in iron, to crystal defects and notably to dislocations, where they form Cottrell atmospheres (Cottrell and Bilby, 1949; Wilde et al., 2000) that limit dislocations mobility (Berns and Theisen, 2008). While Cottrell atmosphere modelling has a long history (Cottrell and Bilby, 1949; Zhao et al., 2000), and their formation in steels has been studied by several authors at the atomic scale (Veiga et al., 2013; Waseda et al., 2017; Candela et al., 2020), an atomistically-informed model of strengthening by interstitial solutes is still lacking. Understanding the processes by which strengthening emerges is especially relevant

in order to prevent failure in accidental conditions. Important modelling efforts are therefore devoted to their integration in plasticity models, which involves various techniques at different scales (Lu and Kaxiras, 2004).

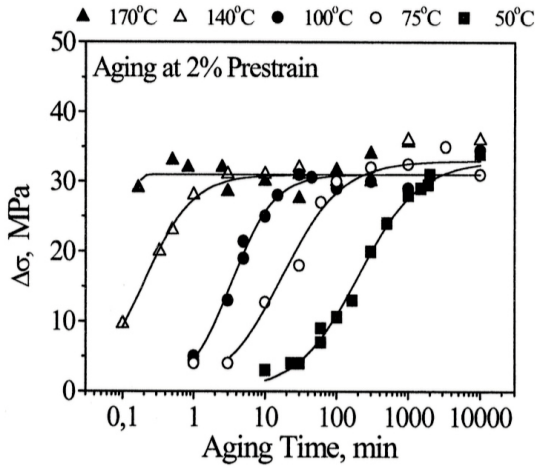


(a) Yield stress augmentation associated with thermal ageing for different times and temperatures. Reproduced from De et al. (2000).

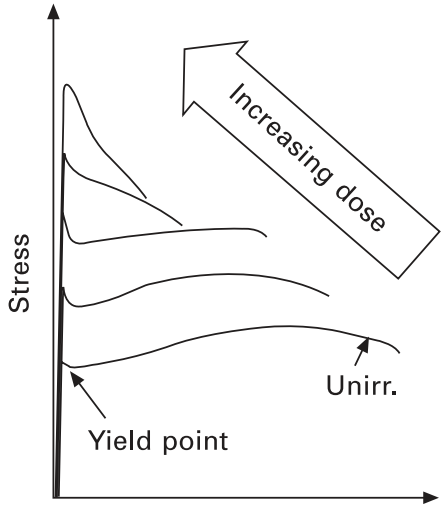


(b) Stress-strain curves for different irradiation conditions. *Unirr.* refers to the unirradiated material. Reproduced from Tipping (2010)

Figure 0.2: **Effect of thermal ageing and irradiation on ferritic steels.**

## 0.2 Multi-scale modelling approach of plasticity

The development of plasticity models aims at understanding the relations between the microstructure and mechanical properties of metals. Continuous models of crystal plasticity (CP), often based on the Finite-Element Method (FEM), are widely-used engineering tools, able to predict the mechanical properties in conditions that were not necessarily tested experimentally using general *constitutive laws*. But the accuracy of such approaches can be limited (Pinna et al., 2015; Mello et al., 2016) and they remain phenomenological (Tipping, 2010).

To improve the reliability of these models, connections should be drawn with lower-scale plasticity models (van der Giessen et al., 2020) which are based on the deformation mechanisms allowed by crystal defects —among which are dislocations, which control plastic deformation under most conditions (Kubin, 2013). As dislocation physics spans a wide range of length and timescales, there is no unique technique able to model dislocations from the scale

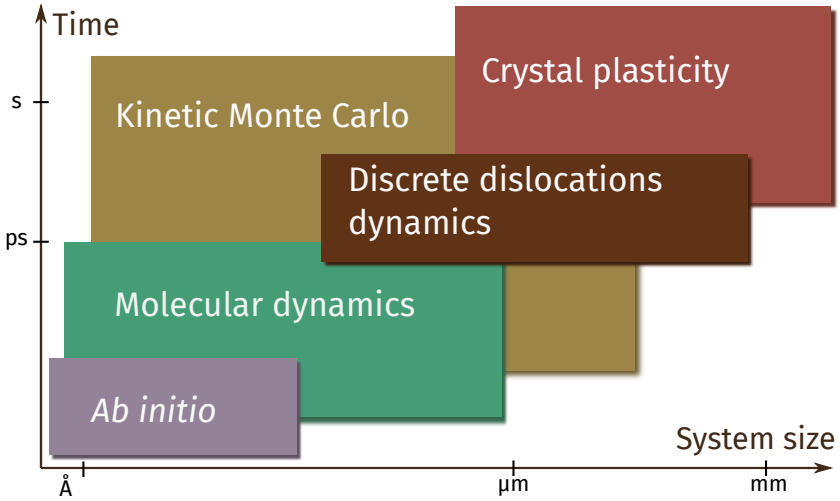


Figure 0.3: **Multi-scale mapping of the main techniques used in metals plasticity modelling.**

of their core up to the polycrystalline microstructural scale, but a set of discrete and continuous numerical methods which together form a multi-scale scheme, presented in Fig.0.3. It is to be noted that several of these methods can be coupled within a single simulation, *e.g.* using continuous methods in some regions to reduce the computational load and number of degrees of freedom associated with discrete methods. Prominent examples of coupling methods include the quasicontinuum method (Shenoy et al., 1999; Miller and Tadmor, 2002; Kochmann and Amelang, 2016), Coupled Atomistic/Discrete-Dislocation (CADD) models (Shilkrot et al., 2002, 2004) or the Macroscopic, Atomistic, *Ab initio* Dynamics (MAAD) method (Abraham et al., 1998).

At the mesoscopic scale, Discrete Dislocations Dynamics (DDD) methods represent dislocations as discrete lines, while Continuous Dislocations Dynamics (CDD) methods model a continuous dislocation density field. Both can be used to model dislocation networks, explaining collective phenomena such as strain hardening (Sills et al., 2018), and to propose constitutive laws usable in CP models. The velocity of dislocations in these simulations is classically given by laws derived from atomistic simulations of dislocations conducted with classical Molecular Dynamics (MD). As MD simulations operate at a much lower scale and with up to $10^{10}$ times more degrees of freedom than DDD (Bertin et al., 2020), velocity laws are obtained from simulations of single dislocations —with an already large computational load— and the interaction between dislocations is thus not taken into account at the atomistic level. Yet, by leveraging important computational resources, it has become possible to use MD to simulate $\sim 10^3$ times larger systems than single dislocations, to compare the

predictions of DDD and MD at the same scale ($\approx$ 1µm) (Zepeda-Ruiz et al., 2021), by identification of the dislocation network from atom positions using "*in silico* microscopy" techniques (Stukowski and Albe, 2010). But beyond the scarcity of High Performance Computing (HPC) platforms suited for this kind of approach, the treatment of the much more complex dislocations-obstacles interaction mechanisms would require extravagant computational resources.

Instead, a more classical approach uses a limited set of atomistic simulations of dislocations in either pure metals or alloys and/or in the presence of other defects to parameterize lightweight analytical (Rodney, 2007; Domain and Monnet, 2005; Maresca and Curtin, 2020) or Monte Carlo (Stukowski et al., 2015; Zhao and Marian, 2018) mesoscale kinetic models of dislocation velocity. Putting the different mechanisms identified at the atomic scale in competition in mesocale models is especially useful to discriminate the most important ones, which should then be integrated in DDD or CP models (Cereceda et al., 2016). The accuracy of atomistically-informed models is fundamentally limited by the interatomic potential (IP) used to compute forces in atomistic simulations (Bulatov and Cai, 2006; van der Giessen et al., 2020), which can be only partially validated on experimental data (Alexander et al., 2020) and has to be built on large *ab initio* databases (Cereceda et al., 2013) to achieve good accuracy and transferability.

The widely-used Density Function Theory method (DFT) is capable of modelling atomic interactions at the electronic level. It was used to model dislocations in a number of metals and semiconductors (Rodney et al., 2017), shedding light on small-scale processes in the region of the core that are crucial for dislocation mobility in pure metals (Woodward and Rao, 2002; Itakura et al., 2012; Ventelon et al., 2013; Dezerald, 2014; Dezerald et al., 2016; Kraych et al., 2019) and in alloys, including the Fe-C system and other interstitials (Ventelon et al., 2015; Lüthi et al., 2017, 2018; Hachet et al., 2020; Romaner et al., 2010), which have to be transferred to larger scales. Indeed, the scale accessible to DFT calculations lies under a thousand atoms in static simulations, and some elementary processes of dislocation motion —such as the kink pair nucleation in b.c.c. metals (Proville and Rodney, 2020)— cannot be captured with this method; dynamical simulations (i.e. *ab initio* molecular dynamics) are also not applicable. One option is to parameterize higher scale models from DFT, such as line tension models Proville et al. (2013); Dezerald et al. (2015); Hachet et al. (2020), velocity laws (Hachet et al., 2022), or kinetic Monte Carlo models (Zhao et al., 2020). Classical MD simulations can also be used, while ensuring they are meaningfully connected to other scales, i.e. that the IP used has a reasonable accuracy compared to *ab initio* data, and that the obtained predictions are transferable to larger scales and other conditions (temperature, deformation rate,

defects concentration,...), for example with the help of an analytical model based on rate theory (Pollak and Talkner, 2005). The connections between different simulation techniques used for modelling plasticity are illustrated in Fig. 0.4, with transfers of information between techniques.

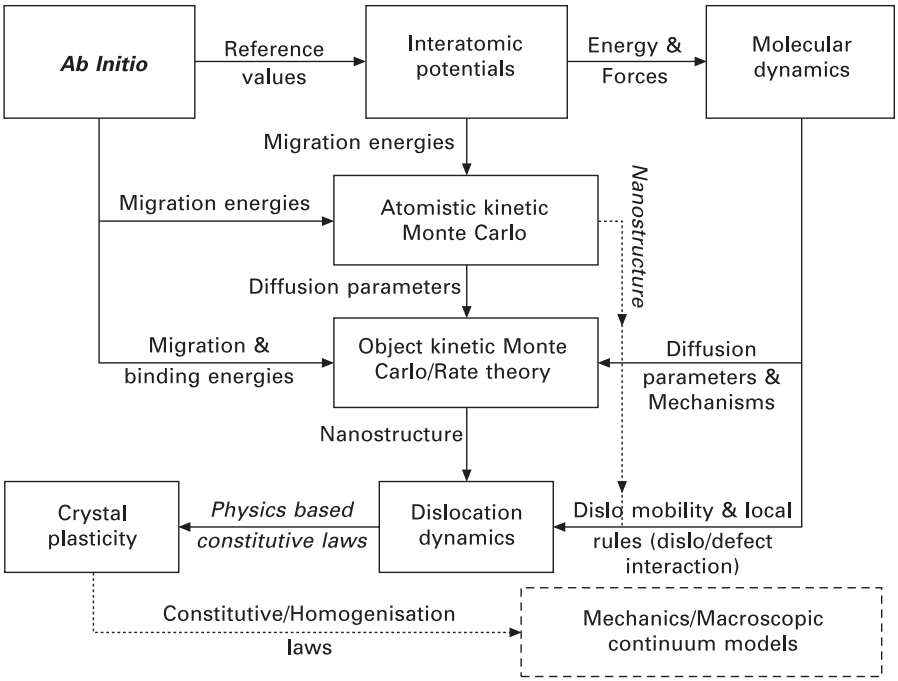


Figure 0.4: **Flowchart of the multi-scale modelling approach illustrating information transfer between techniques.** Reproduced from Tipping (2010).

## 0.3 Towards a mobility law for dislocations in aged steel

Recent DFT results on the interaction between interstitials and dislocations mentioned above offer promising perspectives to better understand how solutes (either in a Cottrell atmosphere or a solid solution) can affect the mobility of dislocations, and ultimately the mechanical properties of steel. However, the results obtained in DFT simulations are limited to the case of high solute concentrations, while the random case of dilute interstitial alloys cannot be treated with DFT, notably because large simulation cells are needed to model kink pairs. The adaptation of existing models of solute strengthening developed for substitutional alloys (Varvenne et al., 2017; Maresca and Curtin, 2020; Rao et al., 2021) to the case of interstitial bcc alloys with large solute-dislocation interaction energies also remains difficult, as an underlying assumption is that solutes do not significantly distort the dislocation

core (Varvenne et al., 2017), while the opposite is suggested by DFT calculations in interstitial alloys (Ventelon et al., 2015; Lüthi et al., 2018). The treatment of interstitials diffusion close to the dislocation core at high temperature also remains inaccessible to such models.

This motivates a detailed investigation of solute-dislocation interactions at the atomic scale in the Fe-C system, to include *ab initio* insights into mesoscale dislocation dynamics models. The aim is to develop a dislocation mobility law in the presence of C, and to extract local rules of interaction with the defects from atomistic simulations (see Fig. 0.4). To achieve this, a number of challenges must be overcome:

**Atomic interactions** The need of an accurate IP for the transfer of information from *ab initio* to atomistic simulations constitutes a first barrier. A survey of existing IPs for Fe and Fe-C presented in Chap. 2 exposes the lack of a Fe-C potential with satisfying dislocation properties. We propose a novel Fe-C EAM potential, based on two potentials of the litterature, which best reproduces dislocation properties in iron compared to DFT, and unlocks the simulation of dislocation pinning by C.

**Dislocation mobility in pure iron** In pure bcc metals, dislocation mobility is strongly limited by the resistance of the lattice, which has to be well understood before integrating the effect of solutes. In Chap. 3, we show that existing models of dislocation glide fail to reproduce the flow stress obtained from low-temperature MD simulations in pure iron. We compare different models and classical assumptions used within the harmonic transition state theory to anharmonic Gibbs energy calculations by leveraging the recent *projected average force integrator* method. Our results unveil strong entropic effects, usually overlooked in dislocation glide models, and anharmonicity especially at high temperature. We propose a model of dislocation glide in Fe in excellent agreement with MD observations, setting the fundation for a model of dislocation glide in the Fe-C system.

**Effect of pinning by interstitial solutes** In Chap.4, the effect of carbon atoms on dislocation mobility is studied atomistically. MD simulations of dislocation glide in a random solid solution confirm a powerful solute strengthening caused by complex processes. We analyse it using a model geometry, where a row of aligned carbon atoms is inserted in the dislocation core. We use a combination of MD simulations, minimum-energy path calculations and extend a stochastic model validated in iron to explain the strengthening induced by carbon. We unveil that carbon disrupts the glide process, as unpinning necessitates the successive nucleation of two kink-pairs, with an activation enthalpy

markedly increased compared to iron at low C-C separations.

# 1 Methods

## 1.1 Atomistic simulations

In this project, our goal is to use molecular dynamics (MD) to simulate the motion of screw dislocations in bcc Fe and Fe-C alloys, with a $\vec{b} = \frac{1}{2}[111]$ Burgers vector, gliding in a $(\bar{1}10)$ plane. Due to the usual tradeoff between model size and computational time in atomistic simulations, the simulation of dislocations, which are extended line defects able to interact at long range, involves many technical concerns. General issues regarding the construction of the dislocation model are discussed in this chapter. Chap. 2 is devoted to a discussion of interatomic potentials.

All atomic system visualizations were produced using the Ovito software (Stukowski, 2010). Dislocation line positions were obtained from atomic positions using the DXA algorithm available in Ovito (Stukowski and Albe, 2010).

### 1.1.1 Molecular dynamics simulations

To run MD simulations, we use the widely-adopted LAMMPS package (Plimpton, 1995), as it offers numerous capabilities, has great parallel performance on CPU and GPU hardwares and is a standard in the community.

All dynamical simulations are conducted in the NVE ensemble, *i.e.* using the `fix nve` LAMMPS command. During dislocation motion, a temperature rise of a few kelvins is therefore observed due to the plastic work, and is included in our reported data. Dynamical simulations are run using the GPU package of LAMMPS (Brown et al., 2011) to accelerate force evaluations. For dynamical simulation, LAMMPS was built based on the 19 Sep. 2019 release, with MANYBODY, REPLICA and GPU packages enabled and support for the GZIP library and `openmpi`. For static benchmarking of potentials (Chap. 2), we built the 4 Jan. 2019 release with the REPLICA, MANYBODY and USER-MEAMC packages.

### 1.1.2 Static simulation of dislocations

As the DFT method is highly computationally expensive, the number of simulated atoms must not exceed a few hundred. Different methods that allow static simulations of dislocations in small systems can be used (Rodney et al., 2017).

The most straightforward approach, called the *cluster approach*, consists in defining a cylinder of atoms, oriented along the [111] direction of the crystal. A screw dislocation is inserted in the same direction at the centre of the crystal, with periodic boundaries along the line direction. The dimension in this direction can be set to 1 Burgers vector for an infinite straight dislocation. This method has several issues due to the limited size of the simulated domain, notably regarding the elastic field of the core, the change of boundary conditions seen by the dislocation when it moves, and the numerical efficiency due to the presence of vacuum around the cylinder. More sophisticated approches use a combination of elasticity and interatomic potentials to implement flexible boundary conditions, where atoms simulated by DFT are surrounded by a wider domain where other simulation methods are applied. But this introduces several technical complications, and does not allow to extract dislocation energies (see Ref. (Rodney et al., 2017) for a detailed discussion).

Instead, to avoid external boundary issues, a method allowing the use of a tri-periodic cell was developed (Bigger et al., 1992; Ismail-Beigi and Arias, 2000). To have fully periodic conditions, a dislocation dipole of opposed Burgers vectors is inserted to obtain a null total Burgers vector. By periodicity, it is representative of a 2D square lattice of dislocations quadrupoles. This arrangement has the advantage to cancel the Peach-Koehler image force on the dislocations. The quadrupolar simulation cell is illustrated in Fig. 1.1. To construct this square arrangement of dislocations of opposed burgers vectors, inserted in two equivalent crystallographic positions (denoted as *easy* and described in Chap. 3), periodicity vectors should respect geometrical constraints as described in Refs. (Ventelon and Willaime, 2007; Ventelon et al., 2013). A setup that matches these constraints and typically used in *ab initio* simulations is a cell of length $n \times b$ in the [111] direction, which contains $n \times 135$ atoms, with $n$ being an integer. By construction, the dimensions in $[\bar{1}\bar{1}2]$ and $[1\bar{1}0]$ directions are respectively $15 \times \sqrt{2/3}a_0$ and $9 \times \sqrt{2}/2a_0$. If a dislocation of the dipole moves (*e.g.* in simulations of dislocation glide), the elastic energy is affected by both the elastic interaction of the dipole, and the deformation associated with the motion of the dislocation. Elastic corrections based on anisotropic linear elasticity can be used to deduce these effects from the total energy, and can be applied using the Babel package[1]. The interested reader is referred to Clouet (2020)

[1] Available at `http://emmanuel.clouet.free.fr/Programs/Babel/index.html`

for a review on *ab initio* methods for the modelling of dislocations. This simulation setup will be used to compare properties computed with interatomic potentials to *ab initio* results in representative conditions.

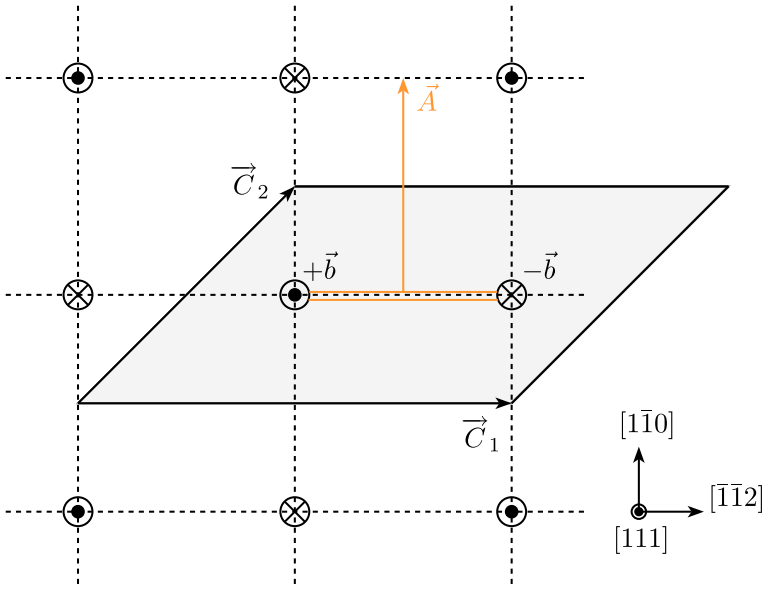


Figure 1.1: **Quadrupolar arrangement of dislocations typically used in DFT simulations.** The simulation cell (grey shape) contains two dislocations of burgers $+\vec{b}$ and $-\vec{b}$. Figure extracted from (Ventelon, 2008).

### 1.1.3 Dynamical simulation of dislocations

For dynamical simulations, it is preferable to avoid fully periodic simulation cells, as the strong attraction between the dislocations of the dipole may result in cross-slip and dislocation annihilation.

Instead, we used a cell represented in Fig. 1.2, where we introduced a single screw dislocation along the $\vec{x} = [111]$ direction using the isotropic elastic displacement solution (Hirth and Lothe, 1982) followed by an energy minimization. Periodic boundary conditions are applied in the $xy\,(\bar{1}10)$ glide plane. Free surfaces are created by extending the cell dimension in the $\vec{z} = [\bar{1}10]$ direction by more than the cutoff radius of the interatomic potential in use, such that atoms in opposite boundaries do not interact. An additional tilt of $b/2$ is applied in the $\vec{y}$ direction, to account for the plastic strain of the dislocation, resulting in a triclinic cell. These conditions generate a periodic array of dislocations (PAD) (Rodney, 2004; Bacon et al., 2009).

Different dimensions in the $\vec{x}$ direction $L_x$ were tested, while dimensions along $\vec{y}$ and $\vec{z}$ and refered as $L_y$ and $L_z$ were set to (138 Å, 159 Å) in dynamic simulations (corresponding to 192000 atoms if $L_x = 40b$) and (138 Å, 80 Å) at zero kelvins (96000 atoms). At finite temperature, a larger $z$ dimension is necessary to lower the attractive effect of free $z$ surfaces on the dislocation, which induces cross-slip.

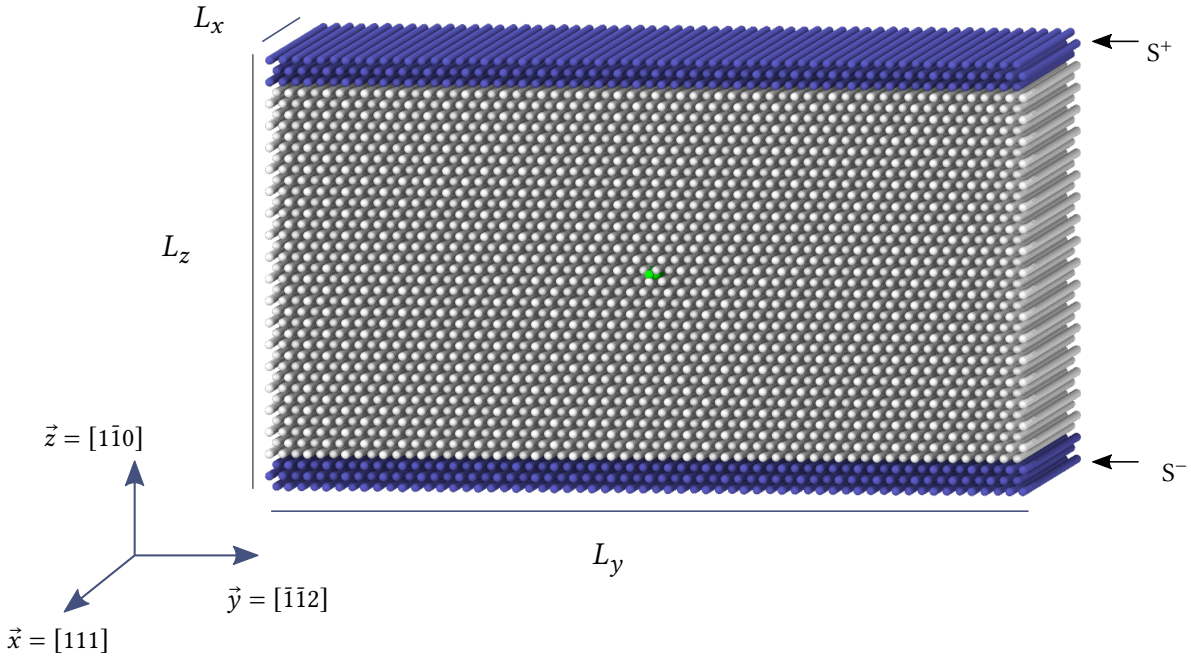


Figure 1.2: **Simulation cell used for dynamical simulations.** A screw dislocation (indicated by a green line) is inserted along the [111] direction in the middle of a crystal of bcc iron. Two regions denoted $S^{\pm}$ are used to shear the crystal (in blue). Atoms visualization was obtained with Ovito.

Dynamical simulations were performed under constant strain rate, using the flexible boundary conditions as presented in Rodney (2007). For this purpose, two slabs of atoms denoted $S^+$ and $S^-$ are defined underneath the top and bottom $z$-surfaces, with a thickness larger than the interatomic potential cut-off radius (approximately 6 Å for classical EAM potentials). An initial velocity is applied to all atoms of each slab, depending on the desired $xz$ shear rate $\dot{\gamma}$:

$$v_{0,x}^{\pm} = \pm\dot{\gamma}\frac{L_z}{2}. \tag{1.1}$$

At every time step, the force in the $\vec{x} = [111]$ direction on each atom $i$ in $S^{\pm}$ is corrected

in order to ensure that the total force in $S^+$ and $S^-$ is zero:

$$F_x^i \leftarrow F_x^i - \langle F_x \rangle^{\pm}, \tag{1.2}$$

where $\langle F_x \rangle^{\pm}$ refers to the average force in $S^{\pm}$ in the $\vec{x}$ direction. In this way, the centres of mass of the slabs move at a constant velocity, thus imposing a constant strain rate, while allowing atoms in $S^{\pm}$ to adapt to the motion of the dislocation (Rodney, 2007). A code example using LAMMPS (version 2 Jul 2021) is given in List. 1.1.

```
# atoms slab 1 is a group of atoms
# CRYSTAL_LZ is the crystal dimension along z
variable avg_velocity_s1 equal vcm(atoms_slab_1,x)
variable vx_init    equal v_gamma_dot*${CRYSTAL_LZ}/2-
   v_avg_velocity_s1
velocity atoms_slab_1 set v_vx_init  0.0 0.0 sum yes

compute average_fx_s1 atoms_slab_1 reduce ave fx
variable fx_to_add_s1 equal -c_average_fx_s1
fix move_s1 atoms_slab_1 addforce v_fx_to_add_s1 0 0
```

Listing 1.1: LAMMPS code snipppet used to apply a constant shear rate on a slab of atoms.

A caveat of this type of simulation cell is the use of different boundary conditions in the $x$, $y$ (both periodic) and $z$ (free surfaces) directions. As the crystal is allowed to change its $L_z$ dimension while $L_x$ and $L_y$ are constrained, thermal expansion is possible along $z$ and blocked along other directions, resulting in an anisotropic residual stress.

Remark The standard procedure presented above might be improved by imposing the $z$ coordinate of the centre of mass of $S^{\pm}$, enabling an equivalent treatment of the thermal expansion in the $x$, $y$, and $z$ directions. This can be done by susbstracting the average force in the atoms group to each atom of the group:

$$F_z^i \leftarrow F_z^i - \langle F_z^{\pm} \rangle. \tag{1.3}$$

Which corresponds to the following LAMMPS snippet:

```
compute average_fz_s1 atoms_slab_1 reduce ave fz
variable fz_to_add_s1 equal -c_average_fz_s1
```

```
fix freeze_s1_z atoms_slab_1 addforce 0 0 v_fz_to_add_s1
```

Listing 1.2: LAMMPS code snipppet used to prevent atoms movement in z direction.

## 1.2 Computational techniques

The rate at which a system transits from one minimum energy state to the next by thermal activation (*e.g.* a dislocation moving through a bcc lattice) is the key component for a thermally activated velocity law, but its computation is notoriously difficult and requires assumptions (Ásgeirsson and Jónsson, 2020).

The transition state theory (TST) (Wigner, 1938) allows to express the transition rate $p$ between minimum energy states (MES). In its most common form, it writes:

$$p \propto \exp\left(\frac{-\Delta G}{kT}\right), \tag{1.4}$$

where the Gibbs energy of activation $\Delta G$ is the difference between the Gibbs energy of the initial state $G_0$ and the transition state $G^\dagger$.

Within the widely used harmonic approximation of atom vibrations (Vineyard, 1957), the temperature dependence of the enthalpy $\Delta H$ and entropy $\Delta S$ is neglected. $\Delta G$ can then be decomposed as $\Delta G = \Delta H - T\Delta S$, yielding:

$$p \propto \exp\left(\frac{\Delta S}{k}\right)\exp\left(-\frac{\Delta H}{kT}\right), \tag{1.5}$$

$\Delta H$ and $\Delta S$ can be computed separately at zero Kelvin using the techniques described in sections 1.2.1 and 1.3 respectively.

While the harmonic approximation is well verified at low temperature, the behaviour at higher temperature can strongly differ from the harmonic prediction due to *anharmonic* effects (Swinburne, 2021; Sato et al., 2021). A recently developed technique (Swinburne and Marinica, 2018) allows the direct computation of the Gibbs energy of activation and is usable on systems containing millions of atoms, with no assumption on thermal vibrations. This method is described in Section 1.3.1 and applied to the case of dislocation glide in iron in Chap 3.

### 1.2.1 Harmonic enthalpy calculation

Saddle-point search techniques are a class of numerical methods used to localise TS and compute their activation enthalpy. In the case where the TS is located between two known MES, double-ended search techniques can be used to find the minimum energy paths (MEP) connecting both[2]. This is the case for the study of dislocation glide in the $(\bar{1}01)$ plane, where the known MES are adjacent Peierls valleys.

#### The CI-NEB method

The Nudged Elastic Band (NEB) method (Henkelman et al., 2000) allows the convergence to the MEP that is closest to an initial guess. This initial path is discretized in a series of successive atomic states called *replicas*, which are usually obtained by linear interpolation of atoms positions in cartesian coordinates between two known MES, designated as initial and final. This simple approach is sufficient to provide an initial guess that is close to a MEP in many cases, but is not optimal for the kink-pair mechanism. In this case, MES are infinite straight dislocation lines in two adjacent Peierls valleys, symmetrical in the direction of the line (*i.e.* the [111] direction). A linear interpolation between the two states preserves this symmetry, which then has to be broken during the NEB calculation, thus increasing the number of steps.

A more efficient approach is to explicitly provide an initial path where the transition goes through the formation of a kink pair, as shown in Fig. 1.3. To do so, we slice the cell in three regions, defined by cutting planes that are perpendicular to the $\vec{x} \equiv [111]$ direction. The first region has a thickness $i/R \times L$, where $i$ is the index of the replica starting at 0, R the total number of replicas and L the cell dimension along $\vec{x}$. In this region, atomic positions are taken from the final state, corresponding to the screw segment that has crossed the barrier. A buffer region of thickness $l_0$ makes a smooth transition to the rest of the cell where the dislocation is in its initial position. In the presence of carbon atoms along the dislocation line, a linear interpolation between the initial and final state is sufficient, as kinks are present in either of both states (see Chap. 4 and especially Fig. 4.10 for more details).

After the initial path is defined, the replicas are relaxed iteratively in the direction of the energy gradient projected in the hyperplane perpendicular to the path, allowing the convergence to the MEP. In order to control the distribution of replicas along the MEP, an harmonic bias spring force is added between adjacent images (Henkelman et al., 2000). This procedure,

[2]When only the initial state is known, single-ended techniques such as the Activation Relaxation Technique presented in this section can be used to sample the accessible saddle states.

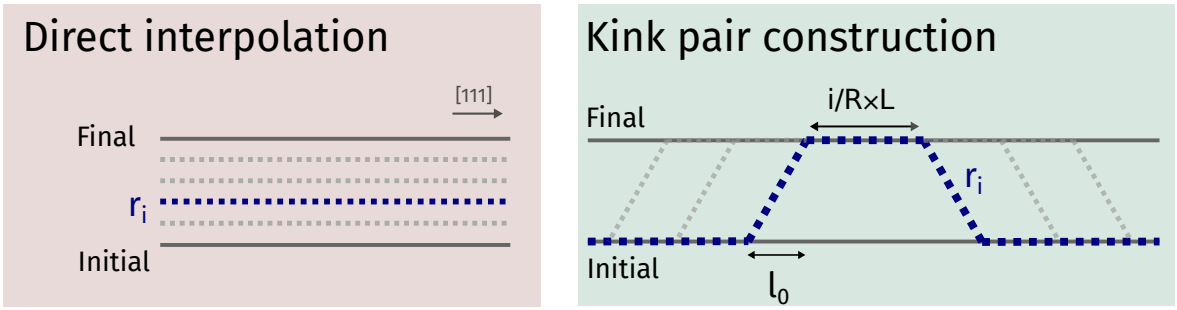


Figure 1.3: **Creation of an initial "guessed" NEB path that explicitly contains a kink pair.** Direct interpolation (left) is compared to our approach (right). With direct interpolation, atoms positions $X$ are linearly interpolated between the initial and final state. In our approach, for replica $r_i$ (with $1 \leq i \leq R-1$), a zone of length $i/R \times L$ in [111] direction has the same atoms coordinate as the final state. A buffer zone of size $l_0 = 5$ Å makes a linear transition to the rest of the cell, where atoms positions are those of the initial state.

reffered to as the classical NEB method, necessitates a lot of iterations to reach an accurate estimate of the energy of a state of interest, which is usually the activated state (*i.e.* the local energy maximum). As forces are evaluated on all replicas at each iteration, this results in a high computational workload to obtain the value of this state of interest. This issue is addressed in the climbing-image NEB method (CI-NEB), available in LAMMPS, which allows to converge more efficiently to the saddle. After a limited number of classical NEB iterations, the replica with the highest energy is selected as the best activated state candidate. It is then forced to climb to the local maximum by reversing the component of the force in the direction of the path tangent. The climbing force is thus:

$$F_c = -\nabla E + 2(\nabla E \cdot \hat{\tau}_c) \cdot \hat{\tau}_c \tag{1.6}$$

where $\nabla E$ is the energy gradient with respect to atoms coordinates and $\hat{\tau}_c$ a normalized vector tangent to the path. A classical optimization algorithm is then used until the force has converged.

Some of the limitations of the CI-NEB method are the sensitivity of the final MEP to the strength of the bias spring force (Kolsbjerg et al., 2016), the high computational cost of increasing the number of replicas along the path, or the addition of the bias force, which makes the force convergence ill-defined. In the case of dislocation unpinning from carbon presented in Chap. 4, complications arise for defining the position of carbon final state. We therefore preferred to use CI-NEB in combination of a single-end search method, the ARTn technique

described below, to automatically determine a final state which is connected by a simple barrier to the initial state. The correct determination of the final state is especially important in this case as we used it as the initial state of another calculation (see Chap. 4 for details).

#### NEB under an applied stress

The NEB method can be used to compute the enthalpy barrier between two positions of a dislocation, under an applied stress. For this, the LAMMPS command `fix addforce` can be used to add an arbitrary force on a group of atoms. Plastic work is produced as the dislocation moves along the $y$ coordinate, which must be included in the total energy to obtain the enthalpy. This is done by using the `fix_modify energy` keyword. A snippet illustrating how to impose an external stress on a slab of atoms (as of `LAMMPS ver. 2 Jul 2021`) is given in Listing 1.3.

```
# -- group definition --
region     slab block EDGE EDGE EDGE EDGE ${bound} EDGE
group      atoms_slab region slab
variable   n_top equal count(atoms_slab)

# -- force and energy computation --
variable   surface equal ly*lx
# stress in MPa
variable   fx_slab equal -v_stress*-v_surface/v_n_top*6.242e-6
compute    disptop atoms_slab displace/atom
variable   enperat_slab atom -c_disptop[1]*v_fx_slab

# -- force and energy fixes --
fix        stress_slab atoms_slab addforce v_fx_slab 0 0 energy
   v_enperat_slab
fix_modify stress_slab energy yes
```

Listing 1.3: LAMMPS code snipppet used to apply an external stress on a slab of atoms, before defining a `fix neb` and using the `neb` command.

When performing such calculations, we faced difficulties due to a bug in the NEB routine of LAMMPS. When loading pre-defined atomic replicas (`neb ... each` command), the periodic boundary conditions were not enforced, resulting in energy jumps when atoms crossed

the cell boundaries. After we identified the bug, it was corrected in the main LAMMPS distribution in its 30 Nov. 2020 version[3]. As a workaround before the bug was corrected, we used an in-house MD code ("MERLIN") which provides an alternative implementation of standard MD techniques, including the NEB method. The code was previously used in several studies on dislocations (Rodney, 2007; Proville et al., 2012). In the case of enthalpy barriers computed under an applied stress, we present the results obtained with this implementation to avoid re-running computationally intensive calculations. To allow the reproduction of our results, the equivalent LAMMPS directives presented in Listing 1.3 can be used in the patched version of the package. In our calculations using the MERLIN code, we used the ARTn technique (presented below) in addition to the CI-NEB method, to avoid difficulties in the definition of the final state.

### The ARTn method

The activation relaxation technique *nouveau* (ARTn) technique (Barkema and Mousseau, 1996; Malek and Mousseau, 2000) is often used to explore the energy landscape around a known MES (Mousseau et al., 2012), searching for saddle-points that connect to unknown MES. It thus requires the knowledge of only one MES, which is highly valuable when final states cannot be easily guessed. This method consists in three main steps:

1. Starting from the MES, the system is iteratively pushed in a random direction in order to leave the harmonic bassin. After each iteration, a relaxation in the hyperplane perpendicular to the random direction is performed, and the lowest eigenvalue $\lambda_0$ of the Hessian matrix is computed using the Lanczos method (Malek and Mousseau, 2000). The system is considered to have left the harmonic basin when $\lambda_0$ is negative (or inferior to a negative threshold set by the user).

2. The activation step, or minimum mode following step, is then performed to converge to the activated state. The system is pushed in the direction of the saddle point following the direction of the eigenvector $\hat{e}_0$ associated with $\lambda_0$, and then relaxed in the hyperplane perpendicular to $\hat{e}_0$. This operation is repeated until the total force is below a preset force tolerance.

3. Starting from the found saddle state, the system is pushed in the direction of $\hat{e}_0$ and then fully relaxed to obtain the final state. In order to verify that the saddle state is

[3] See the relevant pull-request on LAMMPS public development repository: `https://github.com/lammps/lammps/pull/2486#pullrequestreview-540994609`

directly connected to the initial state, the saddle state system is also pushed along $-\hat{e}_0$ and relaxed.

When using the MERLIN code (*i.e.* only for enthalpy calculations under an applied stress), we used the ARTn technique in combination to the NEB method, as follows. CI-NEB was first performed under an applied stress to obtain an estimate of the direction of the saddle state and the overall shape of the barrier, using 250 NEB integration steps. The estimated direction of the saddle state is used to push the system out of the harmonic bassin in the first step of the ARTn technique, instead of a random vector. The ARTn method is then used as described above to determine the saddle point with a force tolerance set to $2.5 \times 10^{-5}$ eV Å$^{-1}$.

## 1.3 Harmonic entropy calculation

The effect of entropy is taken into account by TST models, but computing its value is often difficult. Within the harmonic approximation, the vibrational entropy can be linked to the frequency of each vibration mode $i$ in the initial $\nu_i^0$ and the activated state $\nu_i^\dagger$, obtained by diagonalizing the Hessian matrix in the initial and activated states. The transition rate is then written (Vineyard, 1957):

$$p = \nu^\star \frac{\prod^D \nu_i^0}{\prod^{D-1} \nu_i^\dagger} \exp\left(\frac{-\Delta H}{kT}\right), \tag{1.7}$$

where $\nu^\star$ is a constant that accounts for the attempt frequency (of the order of the Debye frequency), and the configurational entropy for the considered transition event. It can be a function of other variables, such as the number of possible nucleation sites, the temperature or an applied stress, but these dependencies are neglected here. The activated state is characterized by a unique unstable mode which has a negative eigenvalue that should be excluded from the calculation, as the system does not oscillate along this mode. There is therefore one less vibration mode at the denominator.

Evaluating the terms $\nu_i$ requires the diagonalization of the Hessian matrix, i.e. the matrix of the second-order derivatives of atoms cartesian coordinates scales by the atomic masses. For each atom, the Hessian matrix has a $3 \times 3$ dimension, as there are three degrees of freedom for atoms movement, resulting in a matrix of dimension $3n \times 3n$ for a system of $n$ atoms. After diagonalization, the eigenmodes frequencies are obtained from the real strictly positive eigenvalues $\xi_i$ as:

$$\nu_i = \frac{1}{2\pi}\sqrt{\xi_i}, \tag{1.8}$$

and the associated eigenvectors are also obtained. The diagonalization must be conducted at both the initial state and the activated state, which can be obtained by the CI-NEB or ARTn methods.

The main drawback of this approach is the high computational cost of diagonalizing the Hessian matrix that scales cubically with the number of atoms, often leading authors to neglect the effect of vibrational entropy in large systems. To reduce the size of the matrix, we performed the calculation in a cylinder around the dislocation in a PAD cell (as used by Barvinschi et al. (2014)), with a radius of $\sim 28$ Å containing about $N_d = 17 \times 10^3$ atoms. The negligible effect of the finite size of the cylinder was checked by performing a few full diagonalizations in collaboration with M.C. Marinica, which required considerable CPU time and advanced shared-memory linear algebra routines (Proville et al., 2012).

### 1.3.1 Free energy calculation

The use of harmonic enthalpy and entropy calculations has been ubiquitous over the last two decades, and helped solve many problems in materials science. But the harmonic assumption only holds at low temperatures (Lesar et al., 1989; Gilbert et al., 2013; Sato et al., 2021) and a discrepancy can appear for temperatures as low as 10% of the melting temperature (Swinburne, 2021). To account for anharmonic effects, several free energy calculation methods are available. Among them, collective variable-based methods are able to reduce the dimensionality of phase space (Laio and Gervasio, 2008), and have found enormous successes in studies of molecular systems. But collective variables suited for the study of dislocation glide cannot be identified (Swinburne and Marinica, 2018), making this method inapplicable for this problem. A path-based thermodynamic integration method from Cheng and Ceriotti (2018) requires the full diagonalization of the Hessian matrix, resulting in a prohibitive computational cost for large systems. Another popular method is the finite temperature string method (E et al., 2005), which features a linear scaling of the computational time, but requires an *ad-hoc* parameterization (Swinburne and Marinica, 2018).

The projected average force integrator (PAFI) method recently introduced by Swinburne and Marinica (2018) enables free energy calculations with a linear scaling of the computation time and no assumption on the nature of thermal vibrations. In this method, a MEP is obtained by the CI-NEB method, and a series of hyperplanes perpendicular to the path are defined, as represented in Fig. 1.4. Then, constrained molecular dynamics is performed in each hyperplane, consisting in a thermalization followed by a sampling by overdamped Langevin dynamics, which allows the system to move towards a minimum free energy posi-

tion. Note that the sampling can be repeated independently (*i.e.* with perfect parallelism) in order to localize the minimum free energy position more accurately: the number of repetitions therefore provides a simple way of adjusting the precision of PAFI calculations. Under the locality assumption —*i.e.* assuming the temperature pathway remains close to the MEP, a common condition in path-based methods (E et al., 2005)— the free energy gradient can be calculated (Swinburne and Marinica, 2018). By integrating the free energy gradient along the path, the true free energy profile is finally obtained. Due to the sampling at finite temperature and the numerical treatment to extract results, free energy data computed using PAFI have an uncertainty[4], which increases with the temperature, as systems are then able to visit states that are far from the minimum free energy position, and which can be directly reduced by performing more sampling.

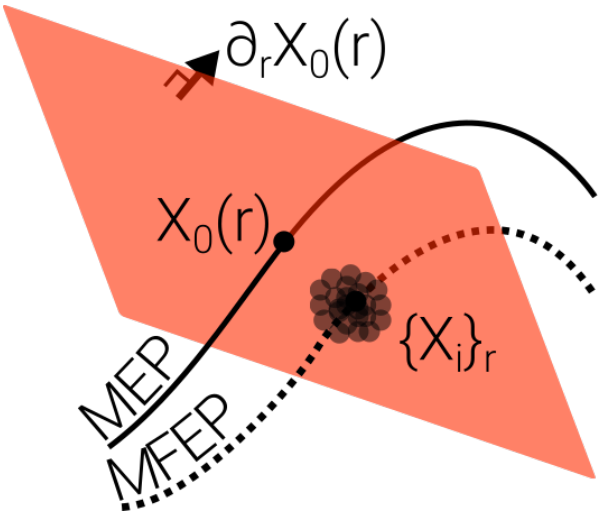


Figure 1.4: **Illustration of the sampling performed by PAFI.** Starting from an initial minimum energy path (MEP) $X_0(r)$, the system is thermalized and constrained MD is performed in hyperplanes that are perpendicular to the MEP (shown in orange), resulting in a global displacement towards a minimum free energy position. An estimate of the minimum free energy position is obtained by repeating the thermalization and constrained MD several times. Following the same approach in a series of hyperplanes along the MEP, the minimum free energy path is determined. (Courtesy of TD Swinburne.)

A C++/MPI implementation of PAFI is freely available to the community and maintained by T.D. Swinburne[5] It uses LAMMPS as its backend, with the `fix pafi` directive[6], and is

[4]For a discussion on uncertainty in PAFI, see: `https://github.com/tomswinburne/pafi/blob/master/error_analysis.pdf`

[5]Online access at: `https://github.com/tomswinburne/pafi`. The code version used in this work and presented in this section is available at: `https://github.com/tomswinburne/pafi/tree/fa82b82c73`.

[6]Online documentation at: `https://docs.lammps.org/fix_pafi.html`

thus fully compatible with all LAMMPS pair styles or settings, allowing *e.g.* Gibbs energy calculations under an external applied stress.

Gibbs energy barrier calculations under an applied stress with PAFI raise several technical issues and require a specific methodology described in the next paragraph. PAFI supports the execution of arbitrary LAMMPS code before the thermalization/sampling starts. To apply an external stress, we use the LAMMPS directives used to perform NEB under an applied stress (see Listing 1.3) in the `PreRun` section of the PAFI configuration file. As multiple LAMMPS runs are performed by PAFI, the different `fix`, `compute` and `region` defined in `PreRun` must all be discarded in the `PostRun` section using the `unfix`, `uncompute` and `region delete` commands, respectively. The PAFI configuration used in our simulations is available at `https://github.com/arn-all/phd-thesis`.

### Construction of the MEP

To start with, a candidate for the MEP between two Peierls valleys is computed using the CI-NEB method under an applied stress $\tau$ (as presented in Sec. 1.2.1), with a $1 \times 10^{-5}$ eV Å$^{-1}$ force tolerance and 16 replicas (or *knots*). The obtained enthalpy profile is characterized by an energy difference between the initial and final states due to the plastic work: $\tau bdL$ ($L$ is the dislocation length, $d$ the distance between Peierls valleys). The activation enthalpy $\Delta H$ is also affected by the applied stress, and decreases as the stress increases. As a result, the ratio between $\tau bdL$ and $\Delta H$ rapidly increases with the stress (it is close to 10 when 500 MPa are applied) and the NEB knots distribution between the initial and activated states tends to be sparse (see Fig. 1.5 (a)).

While this MEP candidate could in principle be used as a reference pathway in PAFI, a spline interpolation between knots with a large energy difference is likely to result in both poor integration accuracy, as the free energy gradient would experience large variations, and a poor estimate of the MEP tangent, which is used for the projection. This would in turn lead to erroneous projections of the reaction coordinate of thermalized systems, and in a large error in the integration of the Gibbs energy. In addition, performing the PAFI sampling in hyperplanes located after the activated state is useful to identify the maximum of the free energy profile, but it represents an additional computational cost that can be important if many knots are located after the saddle state. To increase the knots density in the zone of interest —*i.e.* between the initial and activated states— and remove unnecessary knots, a *remeshing* is performed[7], as represented in Fig. 1.5.

[7] See `https://github.com/arn-all/phd-thesis` for the Python implementation used for our calcula-

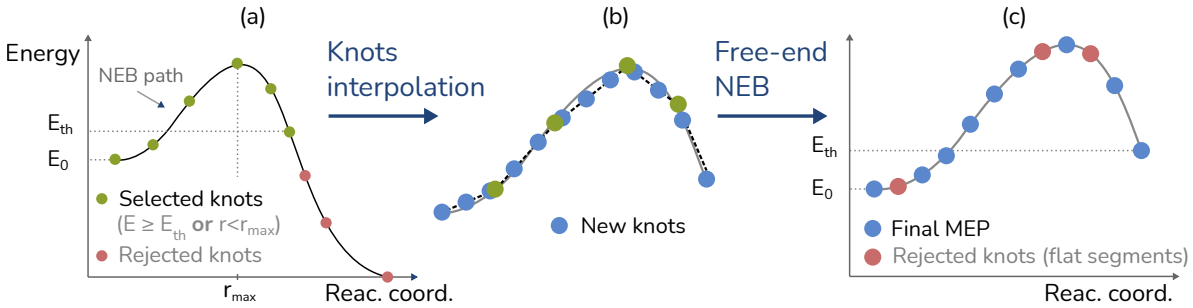


Figure 1.5: **Strategy used to prepare a MEP for PAFI, based on a NEB path with sparse knots density along the barrier.** (a) Knots located after the saddle state ($r > r_{max}$) and below an energy treshold ($E_{th}$) are eliminated. (b) A series of evenly spaced knots (in blue) is obtained by linear interpolation of atoms position between the selected knots (in green). (c) The path created in (b) is relaxed to a MEP using the "free-end NEB" method (see List. 1.4). Flat segments are then eliminated to avoid spline issues when interpolating the MEP in PAFI.

After a series of knots is constructed (Fig. 1.5 (b)), a "free-end NEB" relaxation is performed, using options of the LAMMPS `fix neb` command as shown in List. 1.4. The difference with a regular CI-NEB is that the last knot is not necessarily an equilibrium position. On the last knot, a spring force is applied perpendicularly to the energy path, preventing it from falling in neighbouring energy bassins.

```
1       variable spring equal 0.4
2       variable       u uloop 16
3       fix nebfix all neb ${spring} perp ${spring} end last ${spring}
4       neb 0.0 1e-5 10000 10000 50 each neb_pos_file.$u
```

Listing 1.4: LAMMPS code snipppet used to perform "free-end NEB".

The spline interpolation of the MEP between knots that is performed by PAFI can be inaccurate on flat segments, where splined functions tend to oscillate. To avoid flat segments, we remove knots that have an absolute energy difference to the previous knot that is less than 1% of the activation enthalpy. If the knot that should be removed is the one with the maximum energy, the previous knot is removed instead. To avoid interpolation errors between knots, the PAFI `Rediscretize` option is disabled, such that hyperplanes used by PAFI are located at the position of the knots, instead of allowing arbitrary positions along the interpolated MEP. The number of sampled hyperplanes is therefore the same as the number of knots along the MEP.

tions.

Following this procedure, we obtain a candidate MEP whose stability can be tested using a tool provided in PAFI (`pafi-test-path`), which produces a report based on a 0 K PAFI run which allows to identify flat energy segments, large energy jumps or large deviations between the MEP and the MFEP caused by interpolation issues.

### Computational load and parallelism

A single PAFI run requires about $1 \times 10^6$ force evaluations, and supports parallelism. The full parallelization scheme of PAFI is represented in Fig. 1.6. For each hyperplane along the path, several independent groups of CPUs (called *workers*) perform a MD sampling simultaneously to improve statistical significance, without augmenting the total wall clock time and with perfect parallelism. Each sampling consists in $\sim 10^3$ thermalization steps and $\sim 10^3$–$10^4$ sampling steps (Swinburne and Marinica, 2018). When limited by the number of available CPUs, each worker can be instructed to successively perform several independant samplings (called repeats) in the same hyperplane. Each worker is constituted of one or several CPUs, which allows to accelerate their tasks by providing more CPUs per worker *e.g.* for faster forces evaluation in large systems. These CPUs are made available to LAMMPS's own MPI implementation, with excellent but unperfect parallelism. Ressources allocation is handled through MPI, such that CPUs used by a worker can be distributed accross any number of computing nodes.

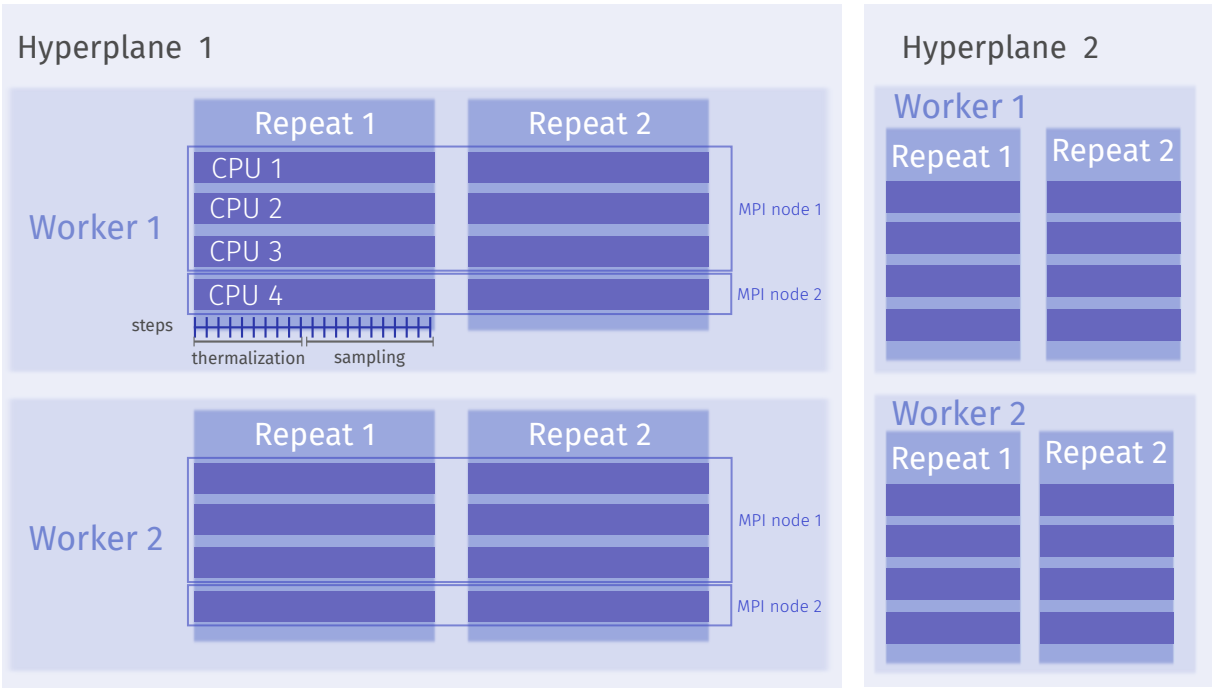


Figure 1.6: **Parallel scheme as implemented in the PAFI code.** Here, the first two hyperplanes are sampled by 2 workers, with 2 repetitions, with 4 CPUs per worker.

# 2 Assessment of interatomic potentials for Fe and Fe-C

The accuracy of MD simulations is highly dependent on the quality of the interatomic potential used, and a careful choice of the potential is thus crucial.

Among the vast range of properties that can be tested, we chose to focus on the most relevant for our study, which are dislocation properties in pure iron, and dislocation-carbon interactions in dilute solutions. In iron, two main features of screw dislocations are their core structure and their Peierls barrier, both known from DFT calculations (Ventelon and Willaime, 2007; Rodney et al., 2017). Even if it has been widely studied in the last decades, reproducing these properties with interatomic potentials while keeping an accurate description of other crystal properties remains difficult (Barvinschi et al., 2014; Alexander et al., 2020; Starikov et al., 2021). In the next section, a litterature survey allows us to compare both properties for the most used potentials for Fe. In the opposite, dislocation properties of Fe-C potentials were often overlooked, and had to be computed.

We tested interatomic potentials for Fe-C alloys available on the NIST interatomic potentials repository (Becker et al., 2013; Hale et al., 2018), listed in Table 2.1. The potentials are based on different formalisms, namely Embedded Atom Method (EAM), Modified Embedded Atom Method (MEAM) and Tersoff, all implemented in the LAMMPS MD package (Plimpton, 1995). The Fe-C potentials from Becquart, Veiga and Hepburn use the Fe interaction proposed by Ackland, and therefore share the same properties in pure iron. While dislocation properties of the Ackland potential are known (Gordon et al., 2010), the Fe part of Liyanage, Lee and Henriksson potentials, which were respectively developed in Refs. (Lee et al., 2012), (Lee et al., 2001) and (Müller et al., 2007a) were never tested for dislocation properties. Table 2.1 also includes information about two EAM potentials for pure iron as well as *ab initio* DFT data, used for benchmarking.

Following our tests, the poor dislocation properties of Fe-C potentials motivated the construction of a new interatomic potential, denoted as "Hybrid", which is an hybridization of the potentials of Proville (Fe) and Becquart (Fe-C) aimed at improving the dislocation properties

of the Becquart potential. Details on the construction of the Hybrid potential can be found in Sec. 2.4, while its properties are presented in comparison to other potentials throughout this chapter.

**Notation**

For clarity, we refer to the interatomic potentials by the name of the first author of the associated publication, *e.g.* "Ackland potential".

| Name | Type | Species | Ref. |
|---|---|---|---|
| Hepburn | EAM | Fe, C | Hepburn and Ackland (2008) |
| Veiga | EAM | Fe, C | Veiga et al. (2014) |
| Becquart | EAM | Fe, C | Becquart et al. (2007) |
| Lee | MEAM | Fe, C | Lee (2006) |
| Henriksson | Tersoff | Fe, C | Henriksson and Nordlund (2009) |
| Liyanage | MEAM | Fe, C | Liyanage et al. (2014) |
| DFT | *ab initio* | Fe, C | Becquart et al. (2007); Ventelon et al. (2013) |
| Ackland | EAM | Fe | Ackland et al. (2004) |
| Proville | EAM | Fe | Proville et al. (2012) |

Table 2.1: **List of interatomic potentials and *ab initio* data used in this study.**

A comprehensive evaluation of the performance of interatomic potentials (i.e. beyond dislocation properties) is a heavy task that is out of the scope of the present work, and rather calls for a collective effort. Several online collaborative projects (Becker et al., 2013; Hale et al., 2018; Elliott and Tadmor, 2011) aim at giving a comprehensive and reproductible assessment of all available potentials, and provide readily-available properties to help potential selection. But at the time of writing, only some classical potentials were available on these platforms; tested properties were limited to basic crystal properties such as the linear thermal expansion coefficient or the elastic constants; and the vacancy migration energy (Li, 2018) was the only implemented test related to defects using the NEB method.

## 2.1 Dislocation core structure

### 2.1.1 Pure iron

The structure of dislocation cores drives many features of dislocation mobility in bcc metals (Rodney et al., 2017). Dislocation core structures can be visualized using "differential dis-

placement" (DD) maps (Vítek et al., 1970) which represent atomic displacements between the perfect crystal taken as a reference, ($s_0$) and the relaxed dislocation ($s_1$). Maps are obtained by projecting the position of atoms in cells with a thickness of 1 $b$ along the [111] direction (i.e. the $x$ axis), so each atom on the map represents an atomic column by periodicity, and their positions in $s_1$ are marked by circles. Although the $(y, z)$ atom positions are generally similar in $s_0$ and $s_1$ in pure metals, where edge displacements are neglgible compared to displacements directed in the [111] direction, representing the positions in $s_1$ is useful in the presence of C which can cause important displacements in the $(y, z)$ plane. To analyse dislocation cores in the presence of carbon, the reference system $s_0$ used is a perfect iron crystal. The filling color of circles (greyscale) represents the $x$ coordinate of atoms in $s_0$ modulo $b$, which is either 0, $b/3$ or $2b/3$. Arrows represent the relative displacement between two adjacent atomic columns, scaled such that an arrow joining two atomic columns represents a relative displacement of $b/3$, and any shorter arrow represents a fraction of this displacement. DD maps presented here were obtained with the `atomman.defect.differential_displacement` funtion implemented in the `1.3.6` version of the `atomman` package. In the presence of solutes, red circles are then added to the plot according to their coordinates in $s_1$.

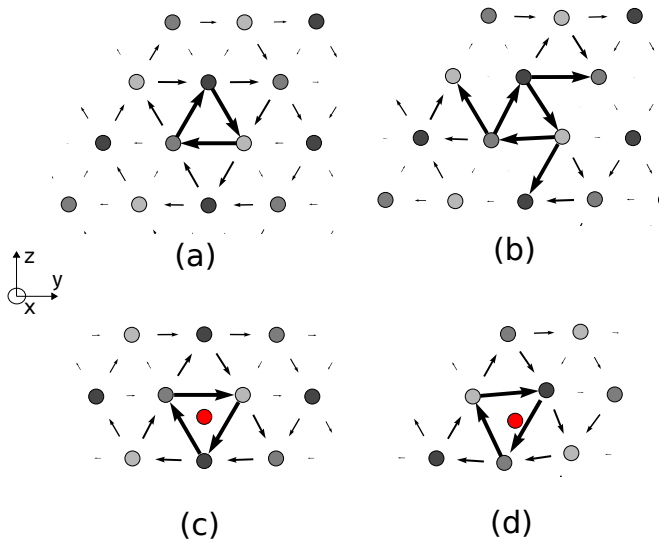


Figure 2.1: **Differential displacements of atoms in the dislocation core region.** See main text for interpretation of. Different structures were obtained: (a) compact core (DFT, all potentials except Lee and Henriksson); (b) degenerate core (Lee); (c) symmetrical core (DFT); (d) asymmetrical core obtained with hybrid potential and other potentials (see text). Circles represent the relaxed position of the atoms. Red circles represent carbon atoms. Head-up triangles correspond to easy positions, and head-down triangles correspond to hard positions.

Using this representation, the *easy* and *hard* core structures of screw dislocations present a characteristic pattern and can be easily recognized. Burgers circuits are also visible, as they are represented by closed circuits of head-to-tails arrows.

The compact, non-degenerate easy core structure, broadly accepted as the stable configuration in iron (Domain and Monnet, 2005; Ventelon and Willaime, 2007; Rodney et al., 2017), is shown in Fig. 2.1 (a). All potentials presented in table 2.1 were tested on this property by inserting a dislocation in an easy position in iron, and minimizing the atomic forces with a $1 \times 10^{-6}\,\mathrm{eV\,\AA^{-1}}$ tolerance. Almost all tested potentials predict a non-degenerate, easy compact core (shown in Fig. 2.1 (a)), in agreement with *ab initio* results. But the potential of Lee predicts a degenerate core shown in Fig. 2.1 (b), and the Henriksson potential favours a structure that is alike the hard structure, both results being in disagreement with *ab initio* data and making these potentials unsuited for the simulation of screw dislocations.

### 2.1.2 Carbon-induced core reconstruction

In the presence of carbon, the structure of dislocation cores in iron can be greatly modified, according to DFT calculations (Ventelon et al., 2015).

A dislocation relaxed with an array of carbon atoms placed every $\vec{b}$ in the octahedral position nearest to the dislocation core (denoted $O^{(1)}$ and shown in Fig. 2.2) spontaneously shifts to a hard position and adopts a *prismatic* configuration, where the three atomic columns of the core have the same atomic coordinates projected along the [111] direction. In this configuration, which is similar to the unstable hard configuration in pure iron (Dezerald, 2014), carbon atoms sit at the centre of the prisms and stabilize the hard core. The initial and force-minimized structures are illustrated in Fig. 2.3. This arrangement has similarities with the structure of cementite ($Fe_3C$) and octahedral sites. As seen in Table 2.2, the first nearest neighbour (1NN) Fe-C distances in the prismatic structure are close to the 1NN distance in cementite, and to the 2NN distance in octahedral sites in bulk iron[1]. The *core reconstruction* is not limited to the FeC system, but was also identified in other bcc metals (Lüthi et al., 2017) and with other interstitial solutes (Lüthi et al., 2018).

For all tested potentials, we observed a conversion from an *easy* to a distorted *hard* core structure as the dislocation was relaxed with C in the $O^{(1)}$ site. The observed structure is close to the *ab initio* structure, although distorted and asymmetrical (see Fig. 2.1 (d) for the

[1] As EAM potentials take interatomic distances as their only input, this overlapping brings the difficulty of accurately reproducing different environments which have similar interatomic distances with the same potential. This issue is partly addressed in the case of MEAM potentials, which also include an angular component (Baskes, 1992).

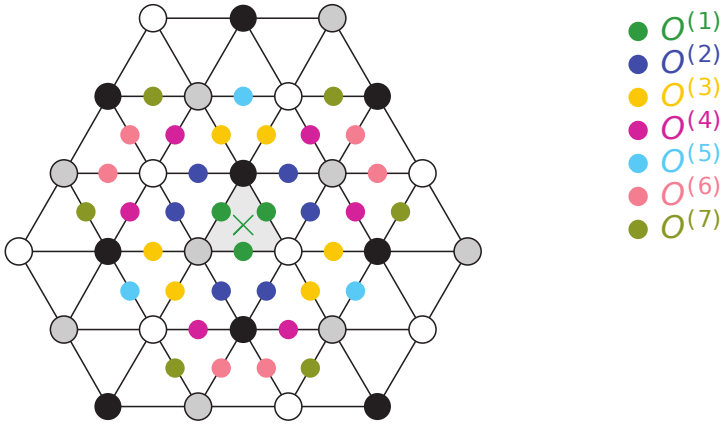


Figure 2.2: **Naming convention for octahedral sites around a screw dislocation (green cross).** Reproduced from (Lüthi, 2017).

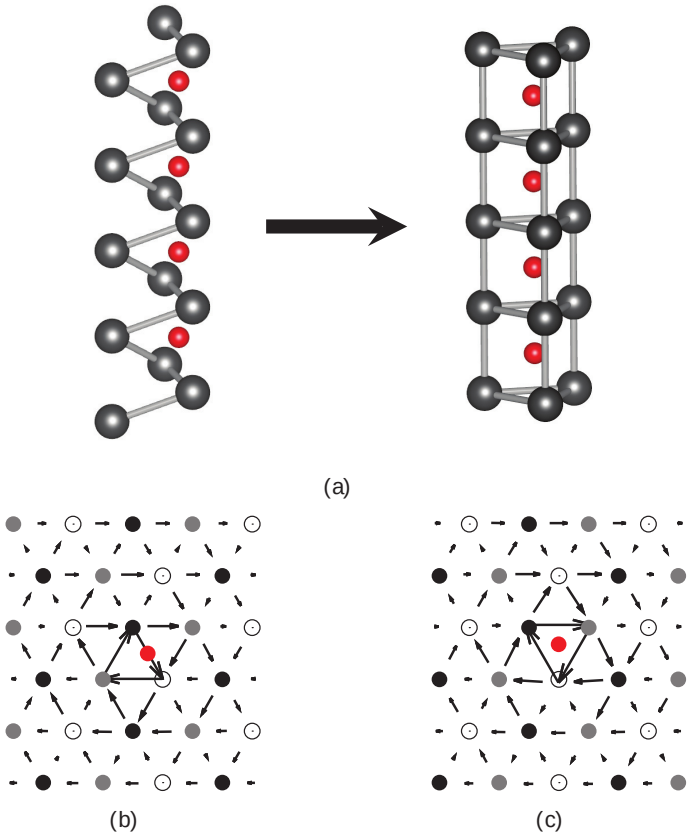


Figure 2.3: **Reconstruction of the dislocation core in the presence of C obtained with DFT.** (a) Dislocation core, with an array of C atoms in $O^{(1)}$ site every $b$, before (left) and after (right) performing an energy relaxation. (b) and (c) are the corresponding DD map for each system. Reproduced from (Lüthi, 2017).

structure obtained with the hybrid potential), as opposed to the symmetrical structure found by DFT calculation (Fig. 2.1 (c)). A 3D visualisation of the core structure and interatomic distances obtained with the Hybrid potential is presented in Fig. 2.4. The length of the longer side of the triangle (2.825 Å) is close to the equilibrium lattice parameter (2.814 Å).

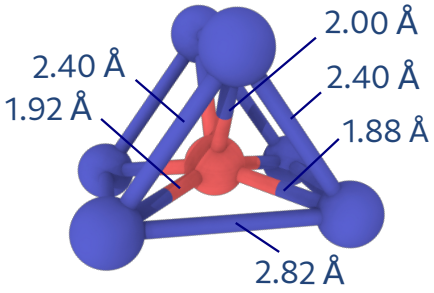


Figure 2.4: **3D visualization of the asymmetrical reconstructed core**. Obtained with the Hybrid potential, after relaxation with a C atom (red) in a $O^{(1)}$ site. Iron atoms are in blue. Interatomic bonds are represented for more clarity.

| | Octa. (bulk) | $P_{1b}$ | $Fe_3C$ |
|---|---|---|---|
| 1NN | 1.77 | 1.93 | 1.96–1.99 |
| 2NN | 1.97 | | |

Table 2.2: **Interatomic distances for different arrangements of Fe-C.** Fe-C distances in Å for the bulk octahedral configuration, the prismatic configuration with C atoms every $b$ noted $P_{1b}$, and in cementite $Fe_3C$, for first and second nearest neighbor (NN). Reproduced from Ref. (Lüthi, 2017).

DFT calculations also evidenced a similar reconstruction upon relaxation when C atoms are inserted in octahedral sites around the core, for distances as large as 3.5 Å (Lüthi, 2017), corresponding to the $O^{(7)}$ position. In our tests with interatomic potentials, the core reconstruction was observed when C is inserted in $O^{(2)}$ for the potentials of Lee and Liyanage only. In the case of Becquart, Veiga and Hybrid potential, the core is converted to a distorted degenerate core shown in Fig. 2.5. With other interatomic potentials, the presence of C in $O^{(2)}$ position did not involve a change of the core structure or a movement of the dislocation.

## 2.2 Peierls barrier

The potential proposed by Mendelev et al. (2003) was the first empirical potential to predict a non-degenerate compact easy core (Mrovec et al., 2011) in agreement with DFT. Though, it

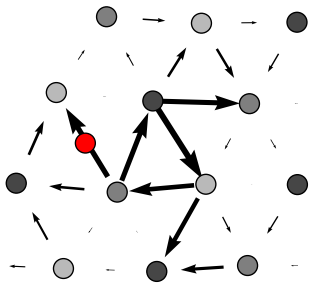

Figure 2.5: **Degenerate core structure induced by C, with the Hybrid potential.** Differential displacements of atoms in the dislocation core region after relaxation with an array of C atoms inserted in the $O^{(2)}$ every $b$.

features a metastable intermediate split-core structure (Gordon et al., 2010) associated with a bent trajectory between easy positions, as shown in Fig. 2.6. Due to this artefact, glide occurs by the nucleation of half-kinks with a low barrier, at odds with *ab initio* data both qualitatively and quantitatively. Attempts to artificially enforce the nucleation of full kink-pairs in NEB calculations of Wang et al. (2019) using the Becquart potential still resulted in ill-shaped barriers, with a metastable intermediate state. The potential developed by Gordon et al. (2011) aims at correcting the barrier shape, but still has a metastable split core (though less deep), and a barrier height close to 12 meV/$b$. A recent potential based on the Angular-Dependent Potential (ADP) formalism (Mishin et al., 2005), fitted with the help of machine learning techniques (Mishin, 2021) by Starikov et al. (2021) also predicts a metastable intermediate core structure, and is thus not usable for the simulation of screw dislocations.

The Peierls barrier predicted by the Liyanage potential was not available in the litterature, and was thus computed. We used the LAMMPS implementation of the NEB method to determine the Peierls barrier in the $(\bar{1}01)$ glide plane. NEB calculations are conducted using a force criterion for convergence of $1 \times 10^{-4}$ eV Å$^{-1}$, a spring force set to 0.1 eV Å$^{-1}$, with 48 replicas. The result is shown in Fig. 2.7. This potential, provides a poor description of the Peierls barrier, with a stable intermediate state which has a lower energy than the easy core.

A potential proposed by Proville et al. (2012) succeeded at providing the correct shape and height of the barrier, making it suitable for the simulation of screw dislocations. A re-parameterization of this potential was proposed more recently to make it suitable for simulations of C15 self-interstitial atom clusters (Alexander et al., 2020), but this was at the expense of dislocation properties, resulting in a underestimate of the Peierls barrrier. Several more sophisticated interatomic models predict a Peierls barrier with a single maximum, namely a Bond Order Potential by Mrovec et al. (2011) (40 meV/$b$), a Gaussian Approximation Potential developed by Maresca et al. (2018) (50 meV/$b$) or a Neural Network potential from

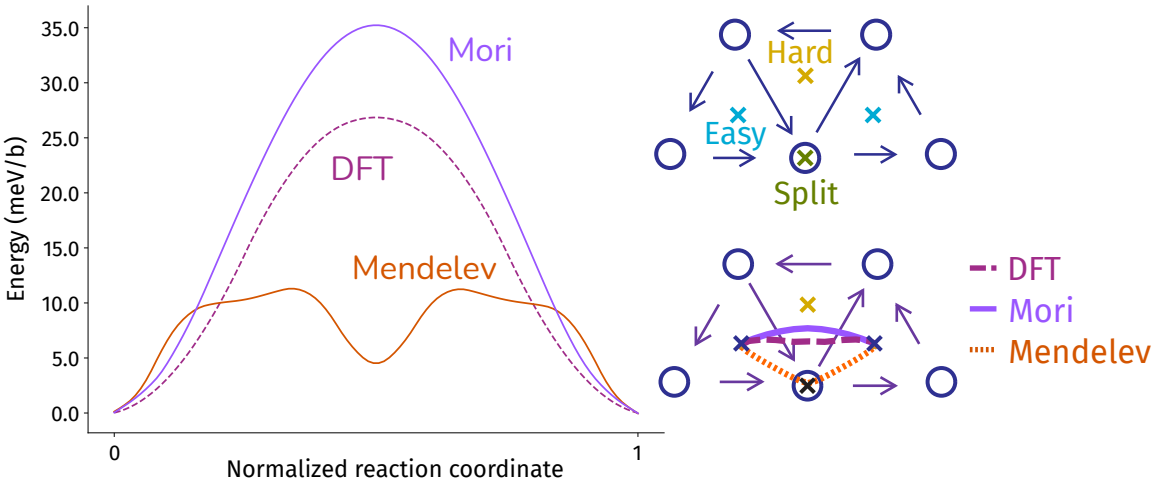


Figure 2.6: **Peierls barrier and corresponding core trajectory.** DFT data (Ventelon and Willaime, 2007) is compared to different potentials. Figure adapted from Ref. (Mori and Ozaki, 2020).

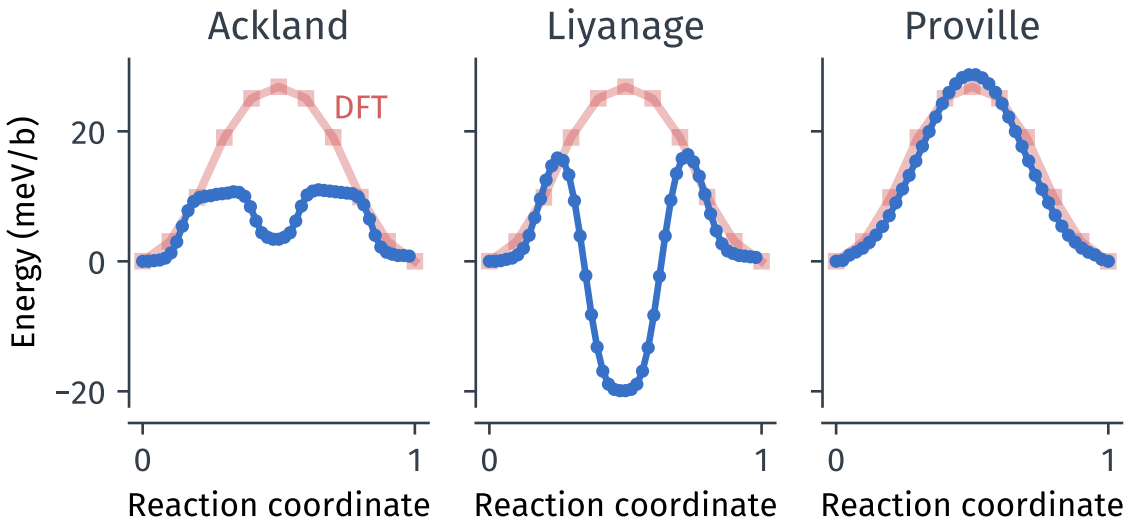


Figure 2.7: **Peierls barriers computed with different interatomic potentials.** Potentials used are indicated in each subplot title, and correspond to blue round symbols. *Ab initio* data from Ventelon et al. (2013) is represented as red squares.

Mori and Ozaki (2020) (36 meV/$b$). As an example, the Peierls barrier and corresponding dislocation trajectory computed with Mori potential is represented on Fig. 2.6. Even though they achieve a much better transferability than the Proville potential, these models are 3 to 5 orders of magnitude more computationally expensive (Starikov et al., 2021), making their use for simulations at the scale of millions of atoms prohibitive, as seen in Fig. 2.8.

At the time of writing, Proville potential was therefore the only potential to achieve quantitative agreement with the *ab initio* Peierls barrier with a low computational load, and was thus adopted by other authors (Narayanan et al., 2014; Shinzato et al., 2019; Ghafarollahi et al., 2019). A complementary discussion on Proville potential can be found in Chap. 3.

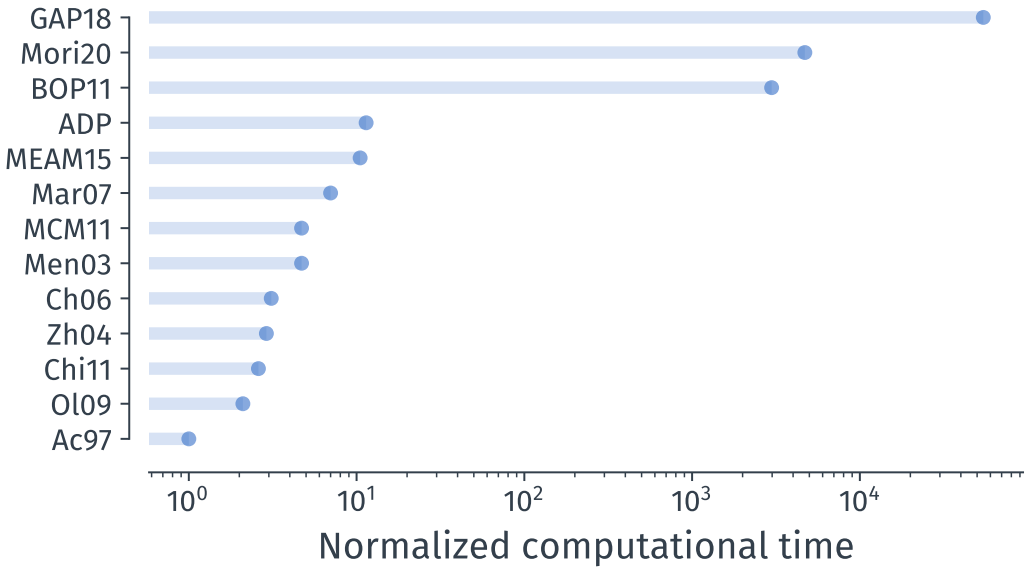


Figure 2.8: **Normalized computational time for different Fe interatomic potentials.** Time is normalized by $7.9 \times 10^{-7}$ s/atom/step. Data extracted from (Starikov et al., 2021), where we added our timing for the Mori NN potential (Mori and Ozaki, 2020), which is $\sim 10^3$ times slower than Mendelev. Potentials names follow the convention adopted in Ref. (Starikov et al., 2021).

## 2.3 Alloy properties

The task of developing interatomic potentials for Fe-C alloys is very complex, as describing pure species accurately is already challenging. As an example, the great diversity of phases and phase transformations found in iron (Ou, 2017; Meyer and Entel, 1998; Müller et al., 2007b; Song and Hoyt, 2012), carbon (de Tomas et al., 2019), and in the Fe-C phase

diagram (Okamoto, 1992) are hard to represent with potentials, especially considering the difficulty to fit potentials on free energy data (Ackland and Bonny, 2020; Ackland, 2002), instead of zero-temperature *ab initio* results. Available potentials can thus only provide a limited description of Fe-C alloys.

At zero Kelvin, most FeC potentials predict that carbon occupies octahedral sites of the bcc lattice -in agreement with *ab initio* calculations (Domain et al., 2004), which predict a higher energy for tetrahedral interstitials (2.14 eV) than octahedral (1.25 eV) (Liyanage et al., 2014). The migration energy for carbon across octahedral sites $E_m$ is thus 0.90 eV (Becquart et al., 2007). Potentials favoring tetrahedral occupation (Ruda et al., 2002) are to be avoided, especially to study the interaction of C and dislocation cores. Values of $E_m$ for potentials available in the litterature are presented in Fig. 2.9. The potentials of Liyanage and Henriksson strongly underestimate this value, resulting in a large overestimation of diffusion kinetics.

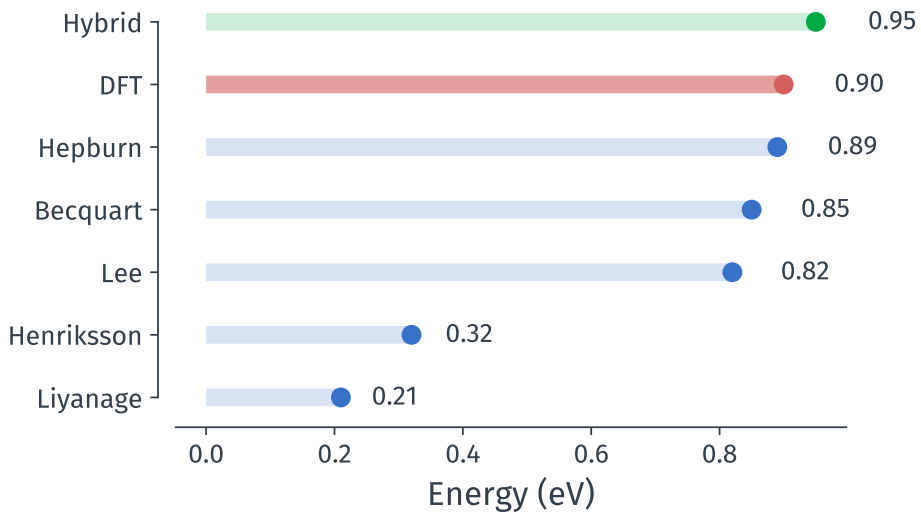


Figure 2.9: **Migration barrier for carbon between octahedral sites.** Data extracted from Refs. (Hepburn and Ackland, 2008; Becquart et al., 2007; Lee, 2006; Liyanage et al., 2014) compared to the DFT target value (Becquart et al., 2007).

### 2.3.1 Carbon-dislocation binding energy

The binding energy of carbon atoms to dislocations is of great importance in the mechanism of solute strengthening (Labusch, 1970; Maresca and Curtin, 2020), and is close to −0.7 eV according to *ab initio* methods in the Fe-C system (Lüthi, 2017) —denoting an highly attractive interaction—. It was calculated as the energy difference per Burgers vector between a

dislocation decorated by carbon atoms ($E_{d+C}$), evenly spaced at a distance $d_{cc}$ along the dislocation, and a dislocation in pure iron ($E_d$), minus the energy associated with the introduction of a carbon atom in bulk iron ($E_{b+C} - E_b$) (Lüthi et al., 2018):

$$E_{binding} = \frac{1}{2}[E_{d+C}(d_{cc}) - E_d] - [E_{b+C} - E_b]. \tag{2.1}$$

Here, $E_{b+C}$ is the energy per $b$ of a cell that contains one carbon atom in an octahedral position, and $E_b$ is the energy of the same cell with no solute atom (subscript b stands for bulk). The factor $1/2$ accounts for the fact that there are two dislocations in the cell.

As seen in Fig. 2.10, the obtained binding energies are negative, meaning an attraction of the carbon atoms to the dislocations, for all potentials except Hepburn potential. The magnitude of the energy varies widely between potentials, with Henriksson and Lee potentials being closest to *ab initio* results (Lüthi, 2017). Moreover, *ab initio* calculations showed that the binding energy is minimum for a distance between carbon atoms in the core of $3b$, which represents an optimum between the gain of adding a carbon atom in the core and the cost of placing the dislocation in a hard configuration between carbon atoms. Most potentials presented in Fig. 2.10 reproduce this feature, although with a minimum at $d_{cc} = 2b$ in most cases. The Hybrid potential reproduces the C-dislocation binding energy quantitatively for $d_{cc}$ larger than 1b.

### 2.3.2 Carbon-carbon binding energy in bulk Fe

In bulk iron, the interaction energy of carbon atoms sitting in octahedral sites has been calculated by *ab initio* methods (Becquart et al., 2007), as a function of the separation distance and crystallographic direction of the C-C pair. Here, we use the same simulation cell as in Ref. (Becquart et al., 2007) in order to determine the binding energy in the [111] direction predicted by interatomic potentials. The cell is fully periodic and contains 128 atoms of bulk iron. The binding energy is calculated as:

$$E_{binding}(d) = E_{C-C}(d) - E_b - 2[E_{b+C} - E_b], \tag{2.2}$$

where $E_{C-C}(d)$ is the energy of a cell that contains two carbon atoms in octahedral positions and separated by a distance $d$ in the [111] direction.

In DFT simulations, there is a repulsive interaction (0.09 eV) for carbon atoms separated by $1b$ along the [111] direction, and an attraction (−0.16 eV) for a separation of $2b$ (Becquart et al., 2007). The potentials presented in Fig. 2.11 show at best a partial agreement with these

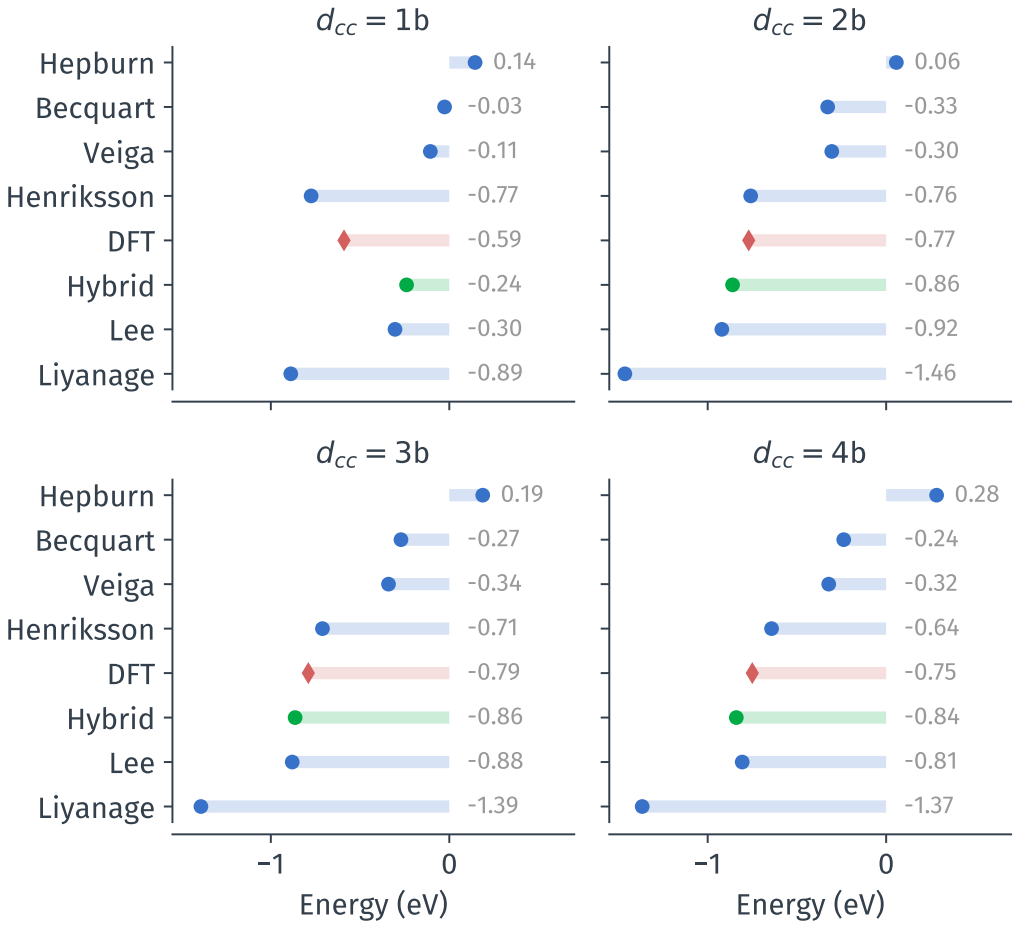


Figure 2.10: **Carbon-dislocation binding energy, as a function of carbon spacing $d_{cc}$ along the dislocation line.** Values obtained with different interatomic potentials are compared to *ab initio* data (Lüthi, 2017). Horizontal lines serve as guides for the eye.

data. In particular, the second neighbor repulsion is systematically underestimated.

Regarding the hybrid potential, the interaction energies are close to Becquart and Veiga potentials at a distance of 1b, but close to zero at 2b, instead of being attractive. The carbon-carbon interaction energy we obtained is thus not fully satisfactory compared to DFT. Though, it is negligible compared to dislocation core effects in this work, as we consider large C-C distances in bulk, due to the relatively low carbon concentration of the cells.

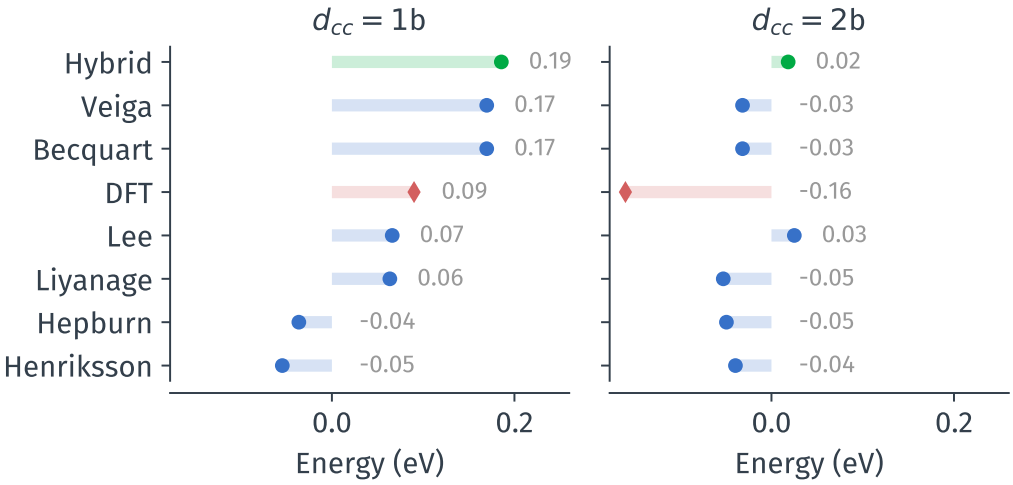


Figure 2.11: **Carbon-carbon binding energy in bulk iron as a function of carbon spacing $d_{cc}$ in the [111] direction.** Values obtained with different interatomic potentials are compared to *ab initio* data (Becquart et al., 2007).

### 2.3.3 Dipolar tensor

In bulk iron, interstitial carbon atoms sitting in octahedral positions cause a local anisotropic strain due to the anisotropy of the octahedral site. Within the framework of the linear elasticity theory, this strain induces in a cell of fixed volume, $V$, a stress increment given by the dipolar tensor $P_{ij}$ (Veiga et al., 2011):

$$\sigma_{ij} = -\frac{1}{V} P_{ij}. \tag{2.3}$$

One method to determine $P_{ij}$ is to measure $\sigma_{ij}$ in relaxed, triperiodic, simulation cells of varying volumes, in which a carbon atom is inserted in an octahedral position. We compared the dipolar tensor obtained with the hybrid potential and with Becquart potential. The former matched experimental values better, as seen in Fig. 2.12.

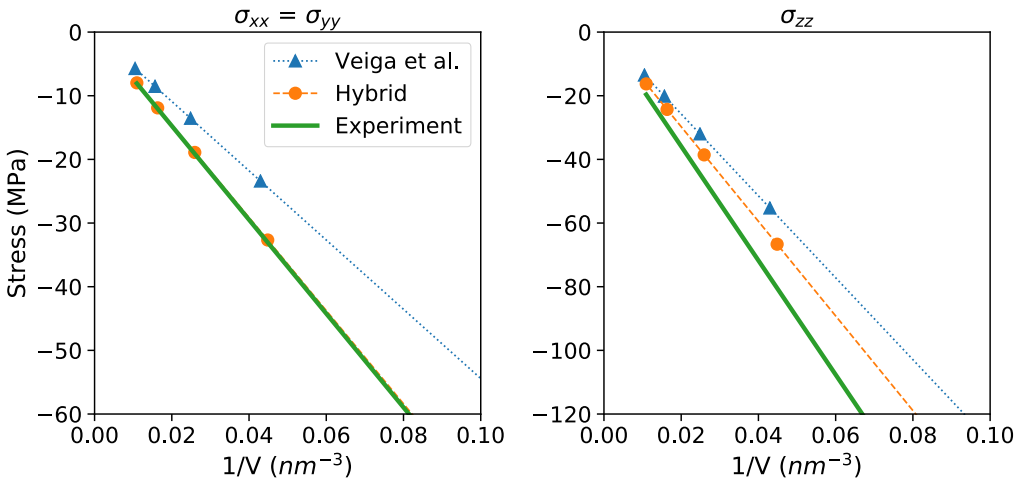


Figure 2.12: **Stress induced by the insertion of a carbon atom in an octahedral site as a function of the inverse volume of the simulation cell.** Experimental data are from (Schultz, 1968). Symbols correspond to our MD simulations. Dashed lines are linear regressions.

## 2.4 Construction of an hybrid interatomic potential

Here, we showed that Proville potential features a Peierls barrier in good agreement with DFT data (see Fig. 2.7), along with the correct dislocation core structure, but this potential is limited to pure iron. For most Fe-C properties, there is a relatively large gap between interatomic potentials and DFT values, and none of the potentials stand out. Yet, Veiga potential qualitatively agrees with DFT on carbon-carbon and carbon-dislocation binding energies. It was used in previous studies to investigate carbon-dislocation interactions, Cottrell atmospheres formation and locking mechanisms (Waseda et al., 2017; Veiga et al., 2015; Tchitchekova et al., 2014; Candela et al., 2020). Both Proville and Veiga potentials are EAM potentials derived from the seminal Mendelev potential (Mendelev et al., 2003). We thus propose here an hybridization of these potentials to combine their advantages, while keeping the properties of Proville potential in pure Fe.

In EAM potentials, the energy $E_i$ of an atom $i$, of species $\alpha$, is the sum of two terms within a cutoff distance: a pairwise interaction $\phi_{\alpha\beta}$ summed over all neighbors $j$ (species $\beta$); and the function $F_\alpha$ that represents the embedding of atom $i$ in the electron cloud formed by its neighbors. It is written as:

$$E_i = F_\alpha\left(\sum_{i\neq j}\rho_\beta(r_{ij})\right) + \frac{1}{2}\sum_{i\neq j}\phi_{\alpha\beta}(r_{ij}), \tag{2.4}$$

where $r_{ij}$ is the distance between atoms $i$ and $j$, and $\rho_\beta$ is the electron density function.

In order to combine Proville and Veiga potentials, we used a classical Gauge transformation (Ackland and Bonny, 2020), which consists in rescaling the electron density and embedding function of iron in a way that does not affect the Fe-Fe interaction. In iron, we define the electron density function $\tilde{\rho}_{Fe}$ and the embedding function $\tilde{F}_{Fe}(\rho)$ of the new hybrid potential as follows, based on the corresponding functions of the Proville potential which are identified by a $\star$ symbol:

$$\tilde{\rho}_{Fe} = A \times \rho^{\star}_{Fe} \tag{2.5}$$

$$\tilde{F}_{Fe}(\rho_{Fe}) = F^{\star}_{Fe}\left(\frac{\rho_{Fe}}{A}\right), \tag{2.6}$$

where $A$ is a constant. The function $\phi_{Fe-Fe}(r)$ was taken from Proville potential (Proville et al., 2012) with no modification. As a consequence, the interaction between iron atoms within the cutoff radius is the same as with the Proville potential:

$$\tilde{F}_{Fe}(\tilde{\rho}_{Fe}) = F^{\star}_{Fe}\left(\rho^{\star}_{Fe}\right) \tag{2.7}$$

This way, we emphasize that the hybrid potential has the same materials properties in pure iron as Proville potential. However, it must be noted that in the case of alloys, the electron density is modified, as all neighbors contribute to the term $\sum_{i\neq j}\rho_\beta(r_{ij})$, regardless of their species. All functions involving carbon, namely $\rho_C(r)$, $F_C(\rho)$, $\phi_{Fe-C}(r)$ and $\phi_{C-C}(r)$ were taken from the Veiga potential (Veiga et al., 2014) with no modification.

The introduction of parameter $A$ in Eq. 2.5 provides a degree of freedom, which was used to tune the hybrid potential in order to obtain the best agreement with the carbon-dislocation interaction energies computed with DFT. The result is shown in Fig. 2.10 and was obtained with $A = 0.55$.

In the original tabulated Proville potential, the electronic density function $\rho^{\star}$ becomes abruptly constant for $r$ <2 Å, resulting in a discontinuity in the forces around 2.0 Å. This discontinuity is confirmed when computing the energy of a dimmer of Fe atoms and its derivatives at a varying distance with LAMMPS. This result is available publicly in the online OpenKIM archive (Tadmor, 2020; Elliott and Tadmor, 2011). In bcc iron, the discontinuity is usually harmless as the shortest equilibrium interatomic distance, which corresponds to $b = 1/2[111]$, is close to 2.4 Å. But in the Fe-C system, octahedral sites have 1NN distances below 2 Å (see Table 2.2), possibly causing large errors in force integration and a shift of the total energy. As a simple way to correct for this discontinuity, we replace the original

tabulated values between 1.95 and 2.05 Å by a cubic spline using the `UnivariateSpline` method of the `SciPy 1.5.2` package.

The Hybrid potential is used throughout the rest of this work, with its parameter $A$ set to 0.55. In additional tests, we obtained a migration barrier for C interstitials of 0.96 eV, which is close to the *ab initio* value of 0.90 eV (Becquart et al., 2007), but with a rough energy landscape around the migration path between octahedral sites. We thus do not recommend using this potential for studies on diffusion mechanisms, or with large C concentrations where solutes occupy adjacent lattice sites.

## 2.5 Conclusion and recommendations

Interatomic potentials were tested in regard to different Fe and Fe-C properties, yielding the following conclusions:

**Performance** For the simulation of dislocations, only the most computationally efficient potentials can be used. They are potentials based on the EAM, MEAM or ADP formalisms. All tested Fe-C potentials follow these formalisms and are thus relatively fast.

**Dislocation core** Most tested potentials feature a compact non-degenerate core in iron, except the potentials of Lee and Henriksson. The core reconstruction induced by C is reproduced by most potentials, with artefacts.

**Peierls barrier** Proville potential provides the best quantitative agreement with DFT over all reviewed potentials. Excluding the most computationally expensive potentials, Proville is the only potential to agree qualitatively with DFT (single maximum). It is thus the only available potential for Fe to provide a physical representation of screw dislocations with good efficiency.

**C-dislocation binding energy** The potentials of Henriksson, Lee, and the Hybrid potential are the only ones to accurately reproduce the DFT value of the C-dislocation binding energy. Solute strengthening effects simulated with other potentials are expected to differ from DFT predictions.

**Energy landscape** The Hybrid potential features a rough energy landscape around the carbon migration path, and should therefore be used with caution for simulations involving the displacement of C. In this case, computational techniques that are highly

dependent on the local topology of the energy landscape (e.g. Hessian matrix diagonalization) might provide incorrect results.

Following these results, it appears that Proville potential is the only potential to enable large scale simulations of screw dislocations in iron in agreement with the Peierls barrier obtained with DFT, and with an acceptable computational load. But as any simplified interatomic model, it also has several downsides (Starikov et al., 2021) and does not describe "real-Fe": it poorly reproduces the phonon spectra for bcc Fe, the formation energy of self-interstitial atoms, or the energy of symmetric grain boundaries, and the kink pair nucleation enthalpy is underestimated (this value is compared to other methods in 3). As new fitting strategies based on machine learning give promising results (Mishin, 2021), novel potentials for Fe that outperform Proville, especially in terms of transferability, are expected to emerge over the coming years.

For the Fe-C system, there was no available potential with a single-humped Peierls barrier, leading us to recommend our hybridization of Proville and Veiga potential. While it also has drawbacks and is likely to find a limited use, it unlocks a major limitation of current potentials, allowing for the first time the simulation of carbon interacting with screw dislocations that move with the correct glide mechanism.

# 3 Thermally-activated glide of screw dislocations in pure bcc iron

Low-temperature plasticity of bcc metals is controlled by the mobility of screw dislocations (Caillard and Martin, 2003; Kubin, 2013; Proville and Rodney, 2020), which is limited by both the strong resistance of the bcc atomic lattice, and interactions with other defects (Bacon et al., 2009), among which are dislocations, grain boundaries, precipitates or solute atoms. In this chapter, the effect of the bcc lattice itself on dislocation motion is studied, while interactions between dislocations and interstitial carbon atoms will be discussed in Chap. 4.

## 3.1 Lattice resistance in bcc metals

In the bcc lattice projected in the (111) plane, the centers of the triangles formed by [111] atomic rows are high-symmetry positions for $\frac{1}{2}\langle 111\rangle$ screw dislocations (Kubin, 2013). The center of upward triangles (in the convention adopted in Fig. 3.1 (b)) is a position of minimum energy, denoted as *easy*, where the helicity is reversed compared to the perfect crystal. In downward triangles, the helicity of the screw dislocation cancels with the helicity of the crystal, and atoms of the core have the same coordinate along the [111] direction (Dezerald et al., 2016). This position is an energy maximum according to *ab initio* calculations (Ventelon and Willaime, 2007). Another high-symmetry position, called *split*, is obtained when the dislocation is located in the close vicinity of one [111] atomic row[1]. This position has a high energy according to DFT results, but it is a common artefact of interatomic potentials to feature a metastable split structure (see Fig. 2.6).

To move from one *easy* position to the next, the dislocation has to pass through a high-energy state located in the dividing plane defined by the *hard* and *split* positions (see Fig. 3.1 (b) and (c)). This position is a saddle point in the energy landscape and is associated to an energy barrier called the *Peierls barrier*, which has the same periodicity $d$ as the crystal lattice

[1] As each row is at the intersection of three different triangles, each split position exists in three different variants.

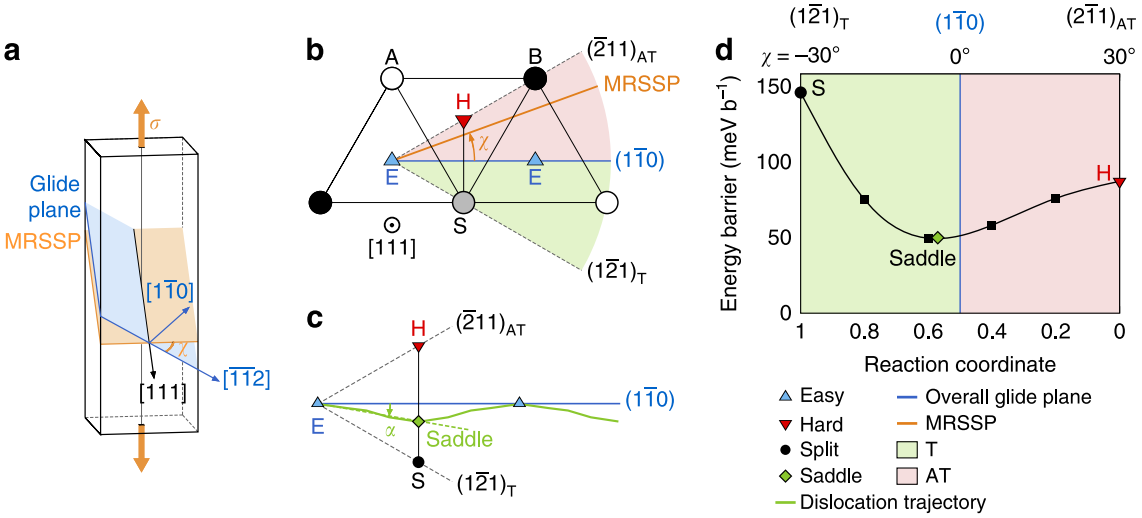


Figure 3.1: **Screw dislocation motion in the bcc lattice.** (a) Schematic representation of the (1$\bar{1}$0) glide plane and maximum resolved shear stress plane (MRSSP). (b) Projection of the BCC lattice in the (111) plane showing the high-symmetry dislocation positions (E, easy core; H, hard core; S, split core). (c) Example of dislocation trajectory (green line) calculated with DFT in Mo and. (d) Energy profile along the hard-split line calculated with DFT in Mo. Reproduced from Dezerald et al. (2016).

in the direction of glide. The maximum stress experienced by the dislocation along the barrier is called the *Peierls stress* and noted $\tau_P$.

*Ab initio* simulations showed that the position of the saddle state is deviated towards the split position by an angle $\alpha$ (see Fig 3.1(c)) rather than being midway between the hard and split. This is due to an assymetry of the energy landscape between the twinning region (T) where sits the split core, and antitwinning (AT) region where sits the hard core, illustrated in green and pink in Fig. 3.1 (Dezerald et al., 2014). While this deviation is low in the case of iron (Dezerald et al., 2016) ($\alpha = -1.7°$ in the absence of an applied stress), another common artefact of interatomic potentials for iron is to predict a large deviation (see Fig. 2.6): in the case of the Proville potential for iron, $\alpha \sim 24°$ (Dezerald, 2014).

THE KINK PAIR MECHANISM At finite temperature, thermal activation can help a short segment of the dislocation to cross the barrier, while it remains connected to the rest of the line by two non-screw segments called *kinks*, forming a *kink pair*. Under an applied stress, kinks experience a Peach-Koehler force that tends to move them in opposite directions along the line, thus expanding the kink pair as shown in Fig 3.2, and allowing the entire line to cross

the barrier[2]. At low temperature and applied stress, the kink pair mechanism is the preferred mechanism for dislocation glide (Kubin, 2013). Conversely, for levels of stress that are above the Peierls stress, the Peierls barrier vanishes (*i.e.* no thermal activation is required for dislocations to move) and dislocations move while remaining straight.

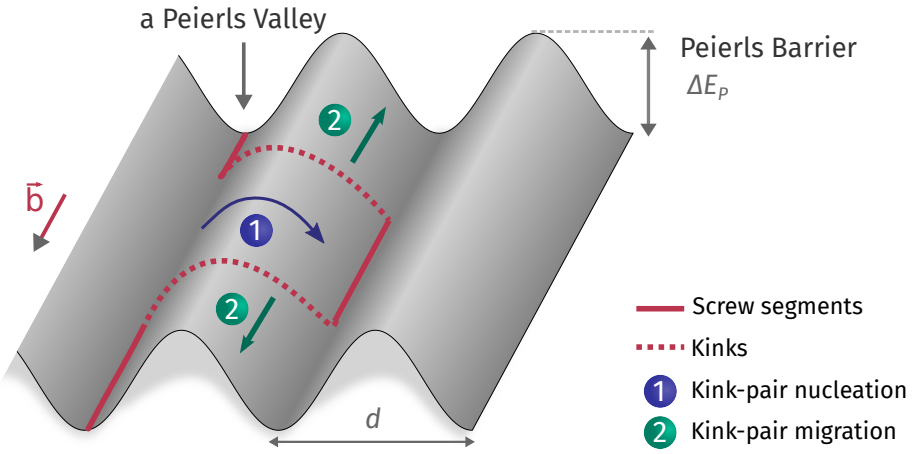


Figure 3.2: **Sketch of the nucleation and migration of a kink-pair.** The red line is a dislocation of burgers vector $\vec{b} = \frac{1}{2}[111]$. The periodic energy landscape on which the dislocation is gliding is represented by a sinusoidal gray surface. Green arrows represent kinks migration due to the Peach-Koehler force.

Under an applied shear stress, a plastic work $\tau bxL$ is dissipated when a dislocation of length $L$ moves by a distance $x$ in the glide direction, and we note the enthalpy for kink pair formation $\Delta H_{kp}$. In Fig. 3.3 (a), two examples of minimum enthalpy paths are represented, one with a low applied stress, and the other with a higher stress. In Fig. 3.3 (b), the stress-dependence of $\Delta H_{kp}$ for Proville potential is presented up to $\tau_P$. With increasing levels of stress, the difference between the equilibrium and saddle states for kink pair formation decreases and kinks become smaller, as shown in Fig. 3.4.

It is common to fit the evolution of $\Delta H(\tau)$ by a Kocks law (Kocks et al., 1975) of the form:

$$\Delta H(\tau) = \Delta H_0 \left(1 - \left(\frac{\tau}{\tau_P}\right)^p\right)^q, \tag{3.1}$$

where $0 < p \leq 1$ and $1 \leq q \leq 2$ are fitting constants and $\Delta H_0$ is the zero-stress barrier for kink pair nucleation. The low stress limit of the kink pair nucleation energy $\Delta H(\tau = 0)$, also

[2]In pure bcc metals, the *secondary Peierls barrier*, which is the energetic cost of propagating the kinks along the line, is negligible —while in alloys, kinks can be pinned by solute atoms (as described in Chap. 4). Kink-pair nucleation and subsequent propagation in pure metals is thus often simply designed as *kink pair nucleation* or *formation*.

noted $E_{kp}$ is ill-defined as with no applied stress, the kinks are only stabilized by their interaction with periodic images: the activated kink pair is therefore symmetrical, with a width that is one half of the simulation cell dimension $L$ in [111] direction, making $\Delta H(\tau = 0)$ L-dependent. The fitting parameter $\Delta H_0$ of the Kocks law provides an estimate of $\Delta H(\tau = 0)$ by extrapolation. The value obtained with Proville potential, close to 0.60 eV (Proville et al., 2012; Ghafarollahi and Curtin, 2020) can be compared to predictions of line tension models parameterized on *ab initio* data. Depending on the line tension model and *ab initio* parameterization, reported values for $E_{kp}$ are 0.86 eV (Proville et al., 2013), $E_{kp} = 0.91$ eV (Dezerald et al., 2016) (using the same tension model but different *ab initio* parameterization) and $E_{kp} = 0.73$ eV (Itakura et al., 2012) with a different model and *ab initio* code. A precise determination of $E_{kp}$ from experiments remains difficult (Dezerald et al., 2015) and leads to different estimates of $E_{kp}$ depending on the stress/temperature domain where experiments are conducted and on the analytical treatment use to extract $E_{kp}$. To avoid these issues, Dezerald et al. (2015) retained the lowest stress-high temperature values from Brunner and Diehl (1991) as a reference: 0.83 eV, even though it gives an underestimation of $E_{kp}$. Two recent potentials for Fe trained on *ab initio* data using machine learning methods yield $E_{kp} = 0.77$ eV and 0.84 eV (Goryaeva et al., 2021). The value obtained with Proville potential is therefore underestimated compared to other methods, with the effect of underestimating the lattice resistance to dislocation motion, and to possibly overestimate the relative effect of other concurrent thermally activated processes (*e.g.* interactions with defects).

## 3.2 Glide of screw dislocations

### 3.2.1 Atomistic simulations

We simulated the glide of a screw dislocation in a PAD simulation cell (see Fig. 1.2) under an imposed shear rate. Examples of stress strain curves obtained at different temperatures with the Proville potential are shown in Fig. 3.5. In dynamical simulations, the stress can be computed using the relation:

$$\tau_{xz} = \frac{F_x^+ - F_x^-}{2A} \tag{3.2}$$

where $F_x^{\pm}$ is the total force in the upper or lower slab (+ and − respectively), projected in the $\vec{x}$ direction (i.e. the glide direction) and A is the area of the free surfaces of the crystal, *i.e.* $A = L_x \times L_y$. The stress computed using Eq. 3.2 undergoes large oscillations (Rodney,

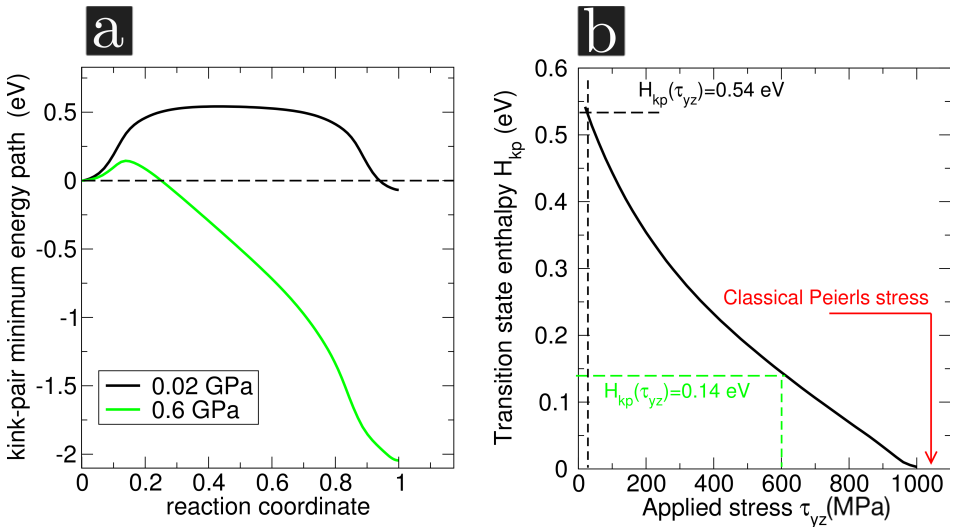


Figure 3.3: **Kink pair nucleation enthalpy.** (a) Minimum enthalpy path associated with the nucleation of a kink-pair, at two different levels of stress. (b) kink pair nucleation enthalpy as a function of the applied stress. All curves were obtained with Proville potential. Reproduced from Proville et al. (2012) (Supp. Materials).

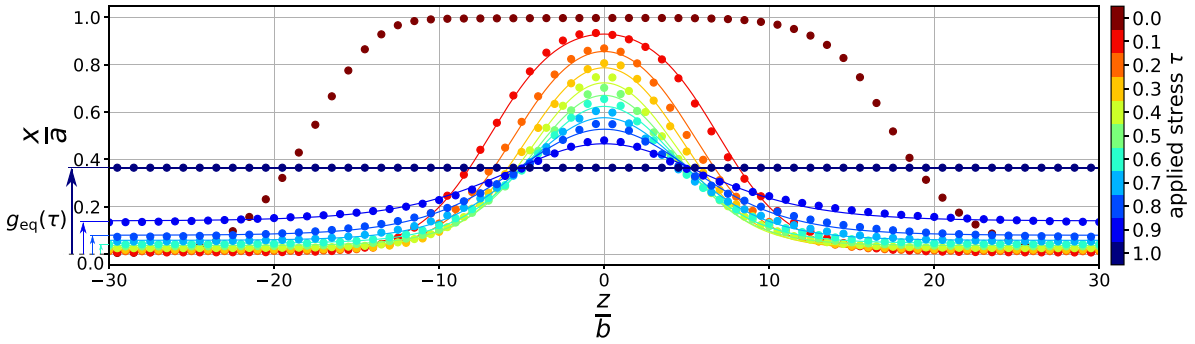


Figure 3.4: **Shape of the transition state for kink pair formation as a function of the applied stress, with Proville interatomic potential.** The equilibrium position of the initial straight dislocation $g_{eq}(\tau)$ is indicated on the lower left. $z/b$ is the position along the [111] direction normalized by the burgers vector length and $x/a$ the coordinate in the glide direction normalized by the distance between Peierls valleys. The stress $\tau$ is normalized by the Peierls stress $\tau_P$. Reproduced from Ghafarollahi and Curtin (2020).

2007), which are eliminated using a Savitzky-Golay filter[3] of order 1 (Savitzky and Golay, 1964), with a window of 51 points (the time difference between successive points is 0.5 ps). The shear stress can also be calculated as the internal stress of the cell $\tau_{xz}$ (named *pxz* in LAMMPS), multiplied by the fraction of the cell volume occupied by the crystal, resulting in less oscillations. We verified that depending on the method used to calculate the shear stress and the chosen average window length, variations of the average stress remained below 20 MPa for the typical stress levels of our MD simulations.

The flow stress is then extracted as the average of the successive peaks of stress in the plastic regime[4] (marked by round symbols). It can be seen that the flow stress decreases with the temperature, as glide is a thermally activated process, and that the peaks height can strongly fluctuate, as dislocation jump is a stochastic process. Five independent MD simulations with different initial atomic velocities were performed to obtain an accurate measure of the flow stress.

Due to the computational load associated with the resolution of classical dynamics equations, our MD simulations are limited to $\sim 10^{10}$–$10^{13}$ steps × atoms, corresponding *e.g.* to the $\sim 10^5$ atoms needed to model dislocation glide, simulated over $\sim 10^6$ time steps of 1 fs, for an overall simulated time of the order of 1 ns. In order to reach stress levels that are large enough to observe plastic events in such limited simulated time, high strain rate and/or temperature values are necessary. At low temperatures, typical MD simulations are therefore conducted at strain rates $\sim 10^{10}$ times larger than experimental conditions (see *e.g.* Proville and Rodney (2020) for a review on atomistic simulations of dislocations), leading to much higher flow stress values.

### 3.2.2 Kinetic models

Kinetic models based on the Transition State Theory (see Chap.1.2) can help compare MD simulations conducted at high shear rates to experimental conditions. In this section, we consider different models of dislocation glide based on the TST, which are then discussed in comparison to MD simulations.

[3] This type of smoothing filter uses a least-squares fits to polynomials on a moving window along the curve to smooth its variations while preserving the height of peaks better than a simple rolling average.

[4] Peaks are detected using the `scipy.signal.find_peaks` Python module with a prominence set to 15. Increasing this parameter has the effect of ignoring smaller peaks.

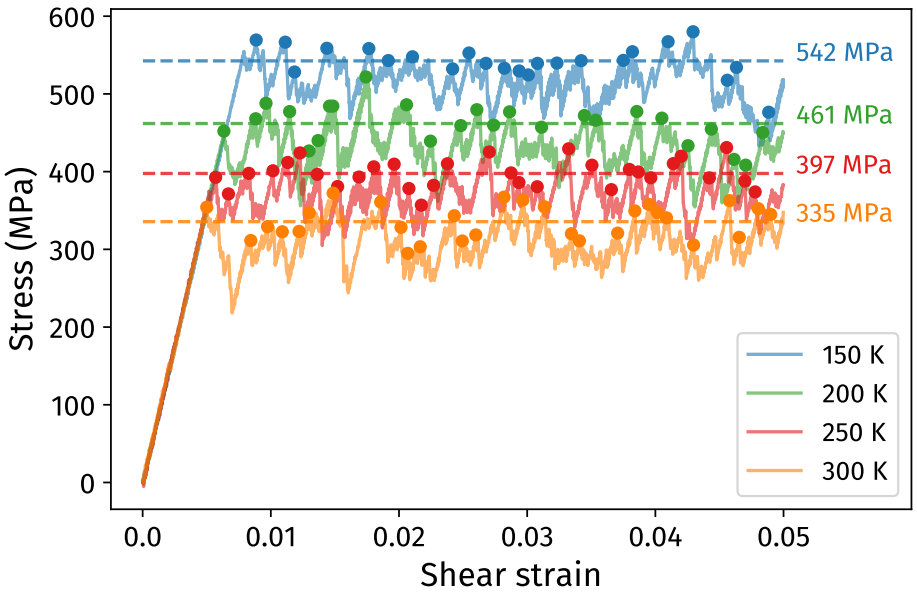


Figure 3.5: **Typical stress-strain curves from MD simulations, at different temperatures.** Simulations conducted with Proville potential with an imposed shear rate $\dot{\gamma} = 1 \times 10^7\ \mathrm{s}^{-1}$. Stress peaks are represented by circles. A dashed line represents the average of the peaks for each temperature (*i.e.* the computed flow stress).

### Thermally-activated forward-jump model

Considering a dislocation jumping from one Peierls valley to the next, the dislocation velocity $v$ is a funtion of the stress tensor $[\sigma]$ and temperature $T$:

$$v([\sigma], T) = \nu L e^{-\beta \Delta G_{kp}([\sigma], T)} \tag{3.3}$$

where $\Delta G_{kp}$ is the Gibbs free energy of nucleation for a kink-pair, $\nu$ is an attempt frequency assumed constant, $\beta = 1/(kT)$, and $L$ is the dislocation segment length available for kink pair nucleation. Although non-Schmid effects would be important to include in a comprehensive study (Christian, 1983; Dezerald et al., 2016; Kraych et al., 2019), we here only consider the effect of the *resolved shear stress* $\tau$ in the {110} glide plane of the dislocation, instead of the whole stress tensor $[\sigma]$.

Computing $\Delta G_{kp}$ remains notoriously difficult (Swinburne, 2021), especially given the dimensions of the system that need to be considered to model the nucleation of kink-pairs, which is beyond the limits of conventional methods (see Sec. 1.3.1). Several assumptions are classically used to simplify the calculation of $\Delta G_{kp}$, which will be discussed in regard to full Gibbs energy calculations allowed by the recent PAFI method and presented in this chapter.

The connection between the dislocation velocity given in Eq. 3.3 and the flow stress computed in strain-controlled simulations is obtained using Orowan's equation in the steady-state regime of deformation:

$$v = \frac{\dot{\gamma}}{\rho b} \tag{3.4}$$

where $\rho = 1/(L_y L_z)$ is the dislocation density.

Neglecting stress fluctuations between jump events and equating Eq. 3.3 and 3.4, the flow stress $\tau^*$ is solution of:

$$\frac{\dot{\gamma}}{\rho b} = vLe^{-\beta \Delta G_{kp}(\tau^*, T)}, \tag{3.5}$$

which can be written:

$$\Delta G_{kp}(\tau^*, T) = kT \log\left(\frac{\rho b v L}{\dot{\gamma}}\right). \tag{3.6}$$

For given simulation conditions, the dimensionless ratio $\Gamma = \frac{\rho b v L}{\dot{\gamma}}$ can be considered fixed as well as $T$, and the value of $\tau^*$ can be determined numerically if $\Delta G_{kp}$ is a known function of $\tau$ and $T$. Within this approach, it is customary to adjust the term $\nu$ to best match the MD data (Rodney, 2007), which is usually obtained with a frequency on the order of the Debye frequency, *i.e.* $\nu \sim 1 \times 10^{13}\ \mathrm{s}^{-1}$.

While it gives a simple way of modelling dislocation glide knowing only $\Delta G_{kp}$ (or an approximation), this model has issues at low stress levels, as it only considers the forward motion of the dislocation, and assumes the kink pair migration time negligible compared to nucleation time. In the limit of a low applied stress, backward jumps become more likely and must be accounted in the average velocity. In addition, kink propagation along the line is driven by the applied stress, and becomes limited under a low stress. For both reasons, the dislocation velocity should tend to zero for low stress levels, while in the above model, $v = \nu L \exp(-\beta \Delta G(0, T)) \neq 0$ at zero stress, which is unphysical.

#### Thermally-activated forward and backward-jump model

To account for the possibility of reverse-jumps at low stress (Nabarro, 2003), an additional term can be added to Eq. 3.3. To move backwards, the reverse energy barrier is $\Delta G_{kp}$ plus an additional energy cost due to the plastic work between the initial and final states $\tau b d L$,

which gives:

$$v = vL\left[e^{-\beta\Delta G_{kp}} - e^{-\beta\left(\Delta G_{kp}+\tau bdL\right)}\right] \tag{3.7}$$

When $\tau bdL \gg \Delta G_{kp}$, this expression is equivalent to Eq. 3.3. One consequence is that reverse jump can remain unlikely down to low stress levels in the case of long segments, thus not effectively reducing the dislocation velocity. Values of $\Delta G_{kp}$ will be given later in this chapter (*e.g.* in Fig. 3.12), but it can already be noted that its low-stress, low-temperature values are close to $\Delta H(\tau = 0) = 0.54\,\text{eV}$ (according to Fig. 3.3), and decrease with T and $\tau$. In Fig. 3.6, we present values of $\tau bdL$ as a function of the segment length $L$, showing that for long segments, the plastic work remains dominant even for stress levels as low as 5-10 MPa, making reverse jumps highly unlikely. Experimental flow stress measurements conducted at high-temperature typically feature long dislocation segments ($L \sim 1\,\mu\text{m}$), and low flow stress values, corresponding to a domain where $\Delta G_{kp}$ is reduced due to the temperature, and possibly negligible compared to $\tau bdL$. An estimation of experimental dislocation density from the work of Brunner and Diehl (1991) yields an estimate of $L \approx \frac{1}{\sqrt{\rho}} = 10^3$ to $10^4$ Burgers vectors. In our MD simulations in the other hand, where $L = 40$ b, the plastic work is much lower and backward jumps are more likely to happen under low stresses.

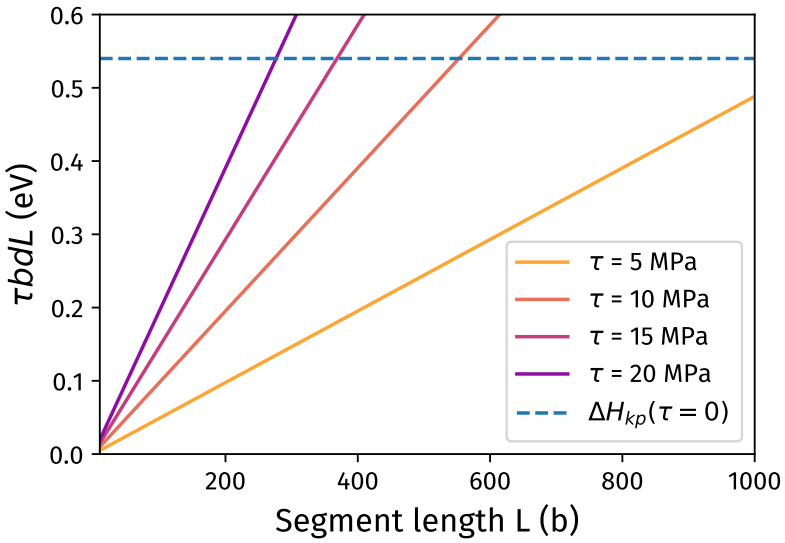


Figure 3.6: **Evolution of the plastic work $\tau bdL$ as a function of L, for different values of $\tau$.** For comparison, a dashed line represents the upper bound for $\Delta G_{kp}$ *i.e.* the zero-stress enthalpy $\Delta H_{kp}(\tau = 0)$ (see Fig. 3.3).

Writing $x = \beta\tau bdL/2$, Eq. 3.7 is equivalent to:

$$v = vLe^{-\beta\Delta G_{kp}}e^{-x}(e^{x} - e^{-x}) \tag{3.8}$$

Using $2\sinh(x) = e^{x} - e^{-x}$, we obtain the following formulation:

$$v = 2vL\sinh\left(\frac{\beta\tau bdL}{2}\right)e^{-\beta(\Delta G_{kp}+\tau bdL/2)} \tag{3.9}$$

Because of the sinh term, this model allows the velocity to tend to zero when $\tau$ tends to zero, as forward and backward jumps are equally probable under zero stress. Here, the flow stress $\tau^*$ verifies:

$$\Delta G(\tau^*, T) = kT\log\left(\frac{2\rho bvL}{\dot{\gamma}}\sinh\left(\frac{\beta\tau^* bdL}{2}\right)e^{-\beta\tau^* bdL/2}\right), \tag{3.10}$$

which can be solved numerically. The $e^{x}$ term in sinh can cause numerical overflow, and better stability is therefore achieved by rewriting it as:

$$\Delta G(\tau^*, T) = kT\log\left(\frac{\rho bvL}{\dot{\gamma}}\left(1 - e^{-\beta\tau^* bdL}\right)\right), \tag{3.11}$$

to obtain values of $\tau^*$ knowing $\Delta G(\tau^*, T)$.

#### Dislocation glide model by Po et al. (2016)

The low-stress domain can also be understood as a low kink migration velocity $v_k(\tau, T)$ domain, where kink pair expansion is the limiting feature, even if there are many kink nucleation events along the line *e.g.* at high temperature or for long segments. Since lattice resistance on kinks is negligible in pure bcc metals, kink velocity is limited by phonon drag and can be written as:

$$v_k = \frac{\tau b}{B(T)} \tag{3.12}$$

where the effective drag coefficient is $B(T) = B_0 + B_1(T)$. $B(T)$ depends on the temperature in the general case, but is approximately constant in the case of screw dislocations, *i.e.* $B_1 = 0$ (Po et al., 2016). The value $B_0 = 9.8 \times 10^{-4}$ Pa s was determined for screw dislocations in tungsten based on the work of Stukowski et al. (2015) and the Frenkel-Kontorova model from Swinburne et al. (2013). In this work, we use the same value as a rough estimate for our calculations in iron with satisfactory results, even though a precise determination of $B_0$ would be valuable. Reducing the value of $B_0$ would result in a higher kink velocity, and a softening at high temperatures where kink migration is dominant (see below), with no

significant change of the model predictions at low temperature. The dislocation velocity is expressed as:

$$v = hJ_{kp}X \tag{3.13}$$

where $J_{kp}$ is the kink pair nucleation rate obtained from the classical kink-diffusion theory of Hirth and Lothe (1982) and is proportional to $v_k$, and $h$ is the kink height. $X$ is the length available for kink pair nucleation, which is the total segment length $L$ if it can only support one kink pair (which is typical of MD simulations). For longer segments, it corresponds to the average distance between existing kink-pairs $\lambda$, which is obtained from the equilibrium concentration of kink-pairs (Hirth and Lothe, 1982), as a function of $\Delta G_{kp}$:

$$\lambda = 2ae^{\beta\Delta G_{kp}/2} \tag{3.14}$$

where $a$ is the crystal lattice parameter. An effective measure of $X$ is therefore obtained by the geometrical average $X = \lambda L/(\lambda + L)$.

The main result of the velocity law proposed by Po *et al.* is an expression of dislocation velocity that accounts for both the low and high stress regime, written:

$$v = v_k \frac{2h}{a} \frac{L}{2ae^{\beta\Delta G_{kp}/2} + L} e^{-\beta\Delta G_{kp}/2}. \tag{3.15}$$

Note that $v$ is proportional to $\tau$ through the term $v_k$, giving a null velocity when the applied resolved shear stress is zero. Isolating $\Delta G_{kp}$ and introducing Orowan's equation as above, we obtain:

$$\Delta G_{kp}(\tau^*, T) = 2kT \log\left(\frac{1}{4a}\left(\sqrt{L^2 + \frac{16hL\rho b^2\tau^*}{\dot{\gamma}B(T)}} - L\right)\right). \tag{3.16}$$

The models presented above all require the knowledge of $\Delta G_{kp}$, which is usually approximated using hypothesis presented below. A comparison of the models introduced in this section and a discussion of their limits will then be presented in § 3.2.4.

### 3.2.3 Classical assumptions in Harmonic TST

While the harmonic assumption on atomic vibrations considerably simplifies the evaluation of the Gibbs energy (Vineyard, 1957)—which can be decomposed in an enthalpic and entropic contribution that are independent of the temperature—, further approximations are often necessary to evaluate the entropic term. For large systems, harmonic entropy calculations are indeed limited by both the computational time and shared-memory cost associated

with the diagonalization of the full Hessian matrix (Proville et al., 2012). Gilbert et al. (2011) proposed to fit $\Delta H_{kp}$ based on MD simulations of dislocation glide, while neglecting the effect of entropy. While it results in accurate velocity predictions, such approach uses a large number of numerical fitting parameters and does not provide an understanding of the physical mechanisms.

### Constant activation entropy

The simplest approach is to assimilate the activation entropy as a constant noted $\Delta S_0$, yielding $\Delta G = \Delta H - T\Delta S_0$. In the case of a thermally activated velocity model (Eq. 3.3), the constant $\Delta S_0$ can be included in the prefactor as:

$$v = \nu L e^{-\beta(\Delta H(\tau) - T\Delta S_0)} = \nu L e^{\Delta S_0/k} e^{-\beta \Delta H(\tau)} = \nu^* L e^{-\beta \Delta H(\tau)}, \tag{3.17}$$

where the constant $\nu^*$ is an effective attempt frequency which can be fitted to best match the MD data. However, as the model of Po *et al.* does not have an attempt frequency term (see Eq. 3.15), we set $\nu = 2 \times 10^{13}\,\mathrm{s}^{-1}$ and only change the value of $\Delta S_0$ for clarity in the comparison between models.

If this approximation has been validated for a specific dislocation by comparison with MD simulations of the glide of Lomer dislocations in Al (Rodney, 2007), there are evidence of temperature dependence of energy barriers for other dislocation processes, including dislocation nucleation (Warner and Curtin, 2009; Ryu et al., 2011), obstacle by-pass (Saroukhani et al., 2016) and cross-slip (Esteban-Manzanares et al., 2020). Moreover, the Gibbs free energy of a straight screw dislocation in BCC iron has also been shown strongly dependent on temperature (Gilbert et al., 2013).

### Meyer-Neldel law

Another classical approximation to include the evolution of the entropy without explicitly computing it is to invoke the Meyer-Neldel (MN) compensation rule (Yelon et al., 2006), which states that the activation entropy of a process is proportional to its activation enthalpy:

$$\Delta S = \Delta H / T_{MN} + \Delta S_0, \tag{3.18}$$

with $T_{MN}$ being a characteristic temperature and $\Delta S_0$ a constant. If $T_{MN}$ is positive, this means that an increase of $\Delta H$ leads to an increase of $\Delta S$, leading to a partial compensation in

the Gibbs energy $\Delta G = \Delta H - T\Delta S$. The Gibbs energy can then be written:

$$\Delta G_{kp}(\tau^*, T) = \Delta H\left(1 - \frac{T}{T_{MN}}\right) + \Delta S_0. \tag{3.19}$$

Similarily to Eq. 3.17, $\Delta S_0$ can be recasted in the $v^*$ term for thermally activated velocity laws.

Usually observed when varying a material parameter, as in the diffusion of different solutes in a given host matrix (Gelin et al., 2020) or magnetization reversals in memory elements of different composition (Desplat and Kim, 2020), the compensation law has also been reported for stress-driven processes in a given material, *i.e.* :

$$\Delta S\big([\sigma]\big) \propto \frac{\Delta H\big([\sigma]\big)}{T_{MN}}, \tag{3.20}$$

for instance for dislocation nucleation (Hara and Li, 2010), creep (Wang et al., 2013), cross-slip (Esteban-Manzanares et al., 2020) and twin motion (Sato et al., 2021) —and could similarily be used for kink pair nucleation.

Applications of the MN law in TST models include dislocation nucleation (Zhu et al., 2008; Amodeo et al., 2021) and glide (Clouet et al., 2021). Gelin et al. (2020) recently tracked down the origin of the compensation law in the harmonic regime to a systematic softening of low-frequency vibrational modes between the initial and activated states.

### 3.2.4 Comparison and discussion

In this section, we compare the flow stress predicted by each model introduced in Sec. 3.2.2, using values of $\Delta G$ determined using different classical assumptions, with flow stress values obtained from strain-rate controlled MD simulations. In MD simulations, $\rho = 4 \times 10^{15}\ \mathrm{m}^{-2}$, $L = 40b$, we take $\nu = 2 \times 10^{13}\ \mathrm{s}^{-1}$ and $\dot{\gamma}$ is set to $1 \times 10^{6}\ \mathrm{s}^{-1}$ or $1 \times 10^{7}\ \mathrm{s}^{-1}$, yielding respectively $\Gamma = \frac{\rho b \nu L}{\dot{\gamma}} = 2 \times 10^{5}$ and $2 \times 10^{4}$. Values of $\Delta H(\tau)$ are taken from Proville et al. (2012) (readily presented in Fig. 3.3).

Model comparison In Fig. 3.7 (a), we compare the three models as a function of T, all using the same Gibbs energy with a typical constant activation entropy $\Delta G_{kp} = \Delta H(\tau) - 7k_B \times T$. All models predict that the flow stress tends to the Peierls stress at 0 K, which is close to 1000 MPa for this potential (see Fig 3.3), and yield similar predictions at low temperature. At higher temperature, model predictions show different behaviors. With the simple forward-jump

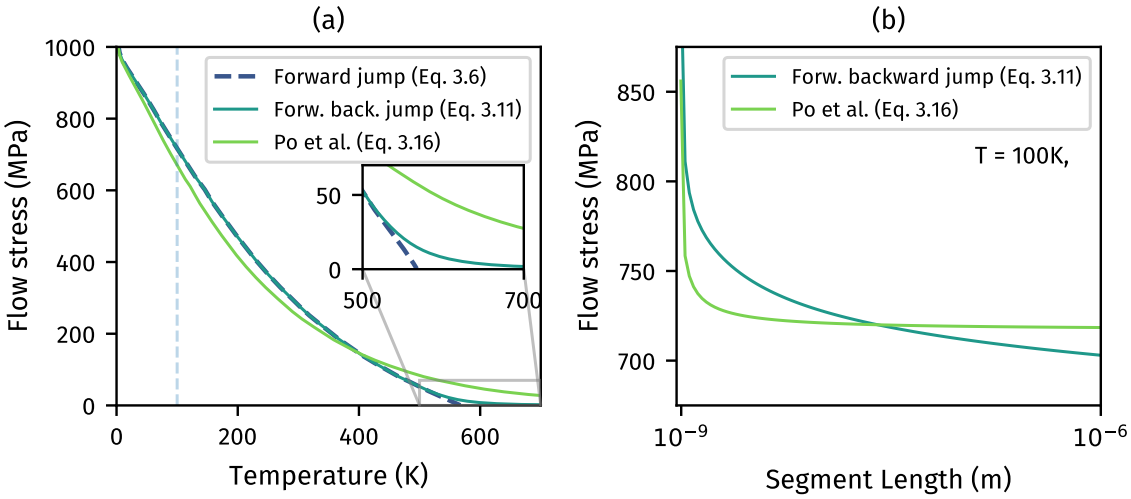


Figure 3.7: **Flow stress predicted using the different models of dislocation glide, as a function of (a) temperature and (b) the segment length (L).** In (a), $L = 40$ b ($\Gamma = 10^4$). In (b), the same conditions are simulated, but the value of $L$ varies.

model, the flow stress decreases until reaching a critical temperature $T_C$ which can be seen as the limit of the thermally-activated regime, before glide becomes athermal. $T_C$ satisfies Eq. 3.6 :

$$kT_C \log\left(\Gamma\right) = \Delta G\left(\tau^* = 0, T_C\right), \tag{3.21}$$

and corresponds to a null flow stress. We have here a well-defined athermal temperature, but plastic flow occurs due to the imposed shear rate (with a finite dislocation velocity $v = \dot{\gamma}/(\rho b)$), while the stress remains zero on average. This behavior is unphysical and is an artefact of the forward jump model, as dislocation glide by the kink pair mechanism can only occur when a non-zero stress $\tau$ allows the expansion of kinks. This issue is addressed by including the possibilty of backward jumps under a low stress. As a result, the athermal temperature $T_C$ is no longer rigorously defined. However, we see in Fig. 3.7 (a) that the difference between models is limited to only very low stresses, allowing to define $T_C$ by extrapolation, yielding the same $T_C$ as the forward model. As the two thermally activated models show no difference except for very low stress values, we do not use the simple forward jump model in the rest of this chapter, and refer to the forward-and-backward jump model as "thermally activated model".

With the model of Po *et al.*, the velocity is proportional to a kink velocity term: $v \propto v_k \propto \tau$ that enforces $v = 0$ if $\tau = 0$. With this model also, the limit of a null flow stress is never reached, and the stress decreases asymptotically at high temperature. At high temperature,

the decrease of the flow stress is slower than with the thermally activated model, making it more difficuly to extrapolate an athermal temperature from the low flow stress domain.

From the expression of the velocity in the model of Po *et al.* (Eq. 3.15), different regimes emerge, where the velocity is limited either by kink migration or kink pair nucleation. For long segments, where nucleation is readily achieved thanks to the great amount of available nucleation sites, or at high temperature where $\Delta G_{kp}$ is lowered, the average distance between kinks pairs is $\lambda$. Kink pair migration then consists in kinks crossing the distance $\lambda$ to annihilate on one another, with an average migration time $t_{mig} = \lambda/v_{\not k}$ which does not depend on $L$. In this domain, the flow stress is limited by kink migration, and is higher compared to the thermally activated model —which only accounts for nucleation— as seen in Fig. 3.7. On the other hand, if the segment length $L \ll \lambda$, *e.g.* in the case of a simulation cell with a short dislocation segment, kink migration will be faster, as it will stop after crossing the distance $L$. In addition, short segments provide only a low number of nucleation sites, which limits the kink pair nucleation rate. In this regime, kink nucleation becomes the limiting feature and $v$ depends on $L$ as both the nucleation time and the migration time $t_{mig} = L/v_{\not k}$ depend on L. These two regimes can be identified in the expression of the dislocation velocity (Eq. 3.15). Using the approximation $L \gg 2ae^{\beta\Delta G_{kp}/2}$ it is simplified as:

$$v = v_k \frac{2h}{a} \frac{L}{2ae^{\beta\Delta G_{kp}/2} + L} e^{-\beta\Delta G_{kp}/2} \sim v_k \frac{2h}{a} e^{-\beta\Delta G_{kp}/2}, \tag{3.22}$$

which is dependent on $L$ and corresponds to the regime where kink migration is limiting. If the contrary approximation $L \ll 2ae^{\beta\Delta G_{kp}/2}$ is used to simplify Eq. 3.15, we obtain:

$$v = v_k \frac{2h}{a} \frac{L}{2ae^{\beta\Delta G_{kp}/2} + L} e^{-\beta\Delta G_{kp}/2} \sim v = v_k \frac{2h}{a} L e^{-\beta\Delta G_{kp}}. \tag{3.23}$$

which is close to the velocity of the thermally-activated model (Eq. 3.3).

The ratio $L/\lambda$ which determines the limiting feature for dislocation velocity is plotted against $\Delta G_{kp}$ in Fig. 3.8, at different temperatures and for different values of $L$. The upper part of the plot corresponds to the regime where kink migration is limiting. For a given temperature and $L$, this is obtained with lower values of $\Delta G_{kp}(T, \tau)$, *i.e.* large applied stress and high temperatures which help kink pair nucleation.

In Fig. 3.7 (b), the flow stress predicted by each model is plotted as a function of $L$ for conditions typical of MD simulations (low temperature, high shear rate). In the short segment regime, both models predict a strengthening, as kink pair nucleation becomes the limiting process. With the model of Po *et al.*, a length-independent regime is obtained for long seg-

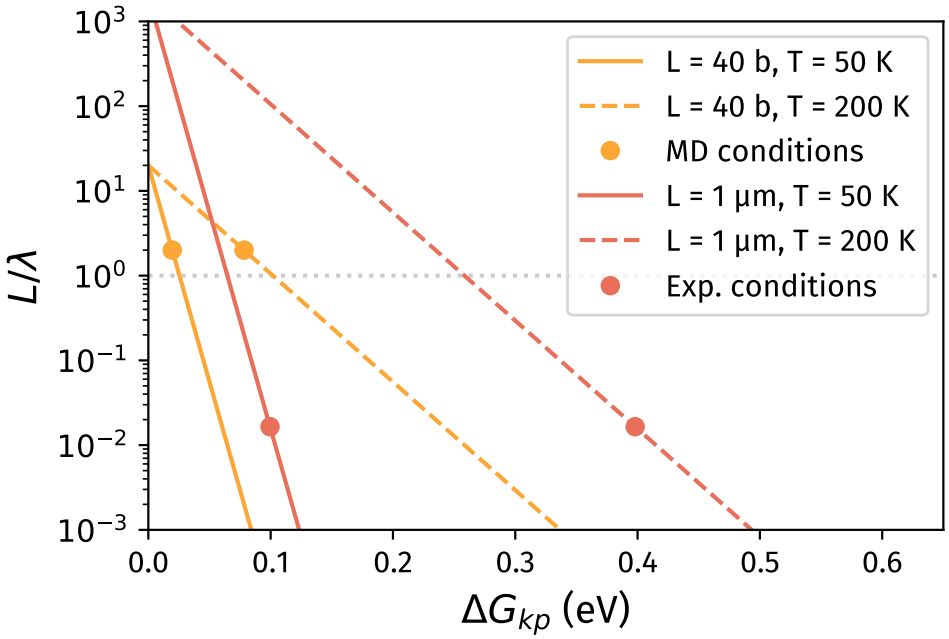


Figure 3.8: **Comparison of the terms $L$ and $\lambda = 2ae^{\beta\Delta G_{kp}/2}$ as a function of $\Delta G_{kp}$.** The term $L$ is dominant in the upper half of the plot, *i.e.* for low values of $\Delta G_{kp}$. Orange circles correspond to an estimation of $L/\lambda$ in typical MD simulations conditions ( $\rho = 4 \times 10^{15}\,\mathrm{m}^{-2}$, $L = 40b$, $\dot{\gamma} = 1 \times 10^{7}\,\mathrm{s}^{-1}$), while red dots correspond to typical experimental conditions ($\rho = 1 \times 10^{12}\,\mathrm{m}^{-2}$, $L = 1 \times 10^{-6}\,\mathrm{m}$, $\dot{\gamma} = 8.5 \times 10^{-4}\,\mathrm{s}^{-1}$).

ments. For the thermally activated model in the other hand, the flow stress slowly tends to zero as longer segments increase the nucleation probability without augmenting the kink migration time, which is neglected.

We emphasise that the kink migration or nucleation-limited regimes are not solely determined by the value of $L$, as $\lambda$ is a function of $\Delta G(\tau, T)$. In Fig. 3.8, it can be seen that the motion of a long segment of 1 µm can be limited by kink nucleation if $\Delta G$ is large( *i.e.* in the case of a low shear rate) or if the temperature is low[5].

Gibbs energy approximations In Fig. 3.9, we compare our MD data to the flow stress obtained based on both harmonic assumptions of $\Delta G_{kp}$ presented in Sec. 3.2.3, *i.e.* either a constant entropy, or a Meyer-Neldel law. Models presented side-by-side use the same expression of $\Delta G_{kp}$. It can be seen that assuming a constant entropy $\Delta S_0 = 7k_B$ yields good results at low temperature. The thermally activated model gives a discrepancy at higher temperature, which is larger with the model of Po *et al.* that predicts a slower decrease of the flow stress. We also tested a Meyer Neldel law to compute $\Delta G_{kp}$, which is presented in the second row of Fig. 3.9 with $T_{MN} = 500$ K. We can see that the agreement with MD data is made worse by introducing the MN law compared to the constant entropy assumption, as it makes the decrease of the flow stress much stiffer. The poor agreement strongly suggests that this system doesn't obey a Meyer-Neldel compensation rule.

These models are therefore not sufficient to explain the temperature evolution of the flow stress observed in the MD simulations. In addition, they are based on unchecked assumptions on $\Delta S$ whose effect is difficult to decorelate from the effect of the underlying velocity model. The temperature and stress dependence of $\Delta G_{kp}$ has been estimated by Gilbert et al. (2013) using thermodynamic integration with the potential of Mendelev, showing a strong stress and temperature dependence and marked anharmonicity. These results suggest that an improved agreement with MD data could be obtained by determining $\Delta G_{kp}$ more accurately. In the following, we use direct Gibbs energy calculations to determine $\Delta G_{kp}$, and implement our results in the well-established velocity models discussed in this section to verify the validity of commonly used expressions of $\Delta G_{kp}$, using a minimum of adjustable parameters.

[5]This is precisely the case encountered at the end of this chapter, when testing glide models on typical experimental conditions, based on Gibbs energies computed with the Proville potential.

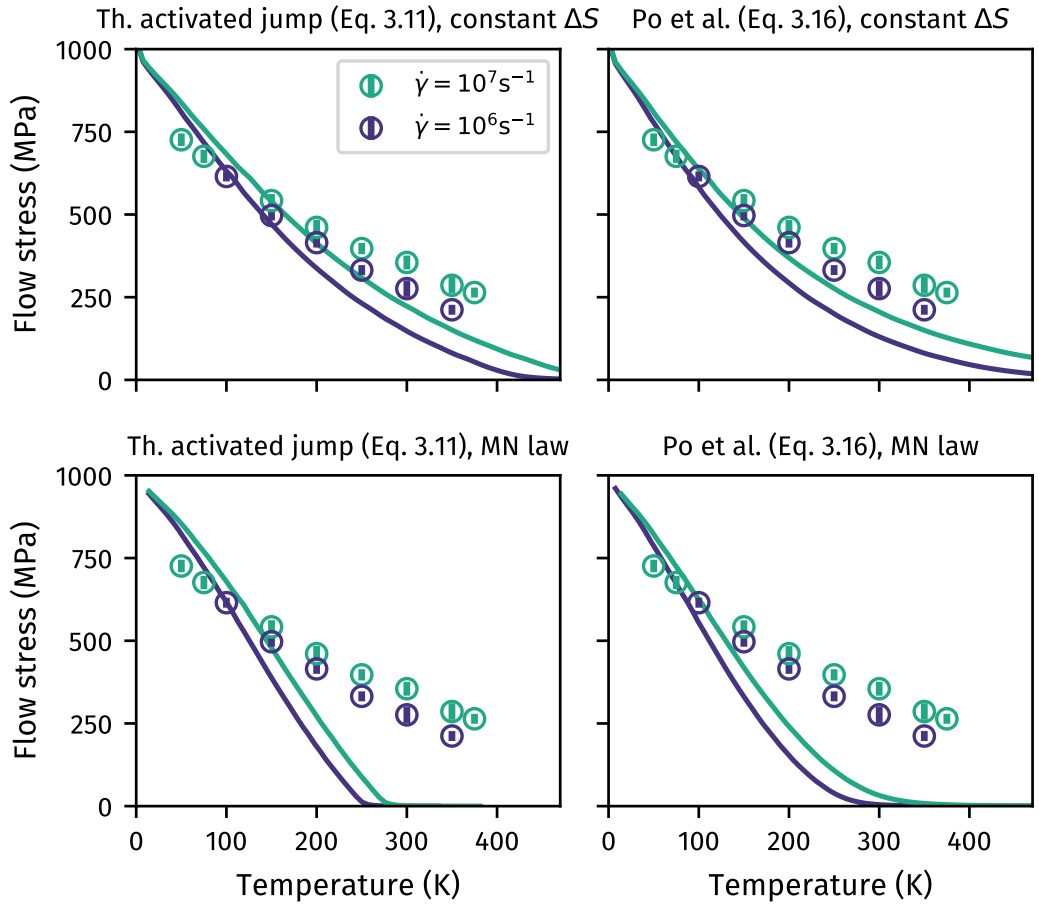


Figure 3.9: **MD flow stress data compared to model predictions assuming either a constant entropy or a Meyer Neldel law.** Each subplot presents the predictions of a model (thermally activated on the left, Po *et al.* on the right), for two different simulation conditions (continuous curves), and compared to corresponding MD simulations (symbols, same color corresponds to same conditions). When assuming a constant entropy, $\Delta S_0$ is set to $8.5 k_B$. For the MN law $\Delta S_0 = 6 k_B$, $T_{MN} = 500\,\mathrm{K}$.

## 3.3 Beyond the harmonic approximation

Approaches developed in the previous section are unable to accurately predict the flow stress at high temperature. The harmonic assumption which sets the basis of the harmonic TST is known to hold only at low temperatures, and anharmonic effects are expected to appear at higher temperature (Lesar et al., 1989; Gilbert et al., 2013; Sato et al., 2021; Swinburne, 2021). The PAFI method introduced in Sec. 1.3.1, which allows the evaluation of free enthalpy barriers associated with kink pair nucleation, is used in this section to explore a broad range of stress and temperature. Technical details regarding the PAFI method and our calculation methodology were already presented in Sec. 1.3.1. In our calculations, we use simulation cells that are twice smaller in the $z$ direction (*i.e.* the direction with no boundary conditions) compared to the MD simulations, in order to reduce the computational load. The cell dimensions are given by the following numbers of unit cells along $x$, $y$, $z$: $(N_x, N_y, N_z) = (40, 20, 20)$. Additional tests conducted with $(N_x, N_y, N_z) = (40, 15, 15)$ and $(40, 30, 20)$ showed no significant effect of the cell dimension in the $y$, and $z$ directions.

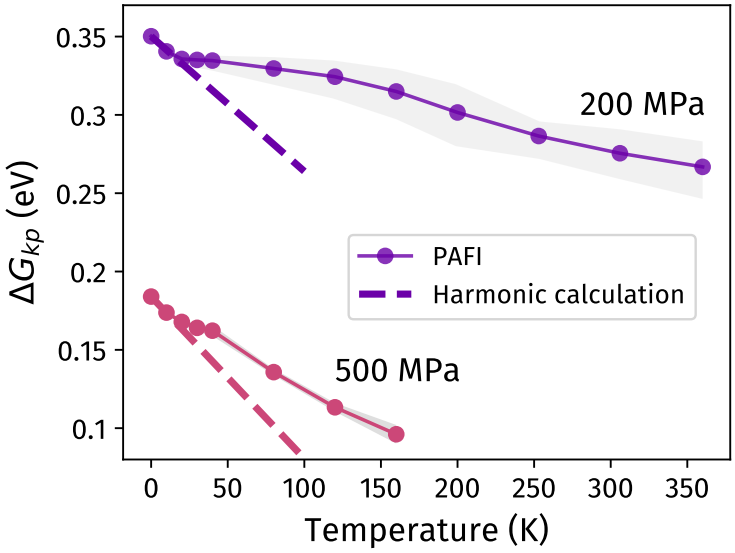


Figure 3.10: **Gibbs activation energy at low temperature, at 200 and 500 MPa.** PAFI calculations were conducted with a high level of accuracy, resulting in a narrow uncertainty domain (gray area). The results of harmonic entropy calculations conducted at 200 and 500 MPa are presented as dashed lines.

In Fig. 3.10, we present values of the free enthalpy of activation for kink pair nucleation $\Delta G_{kp}$ computed with applied stresses $\tau = 200$ MPa and 500 MPa as a function of temperature. $\Delta G_{kp}$ is calculated as the difference between the maximum and initial Gibbs energy along

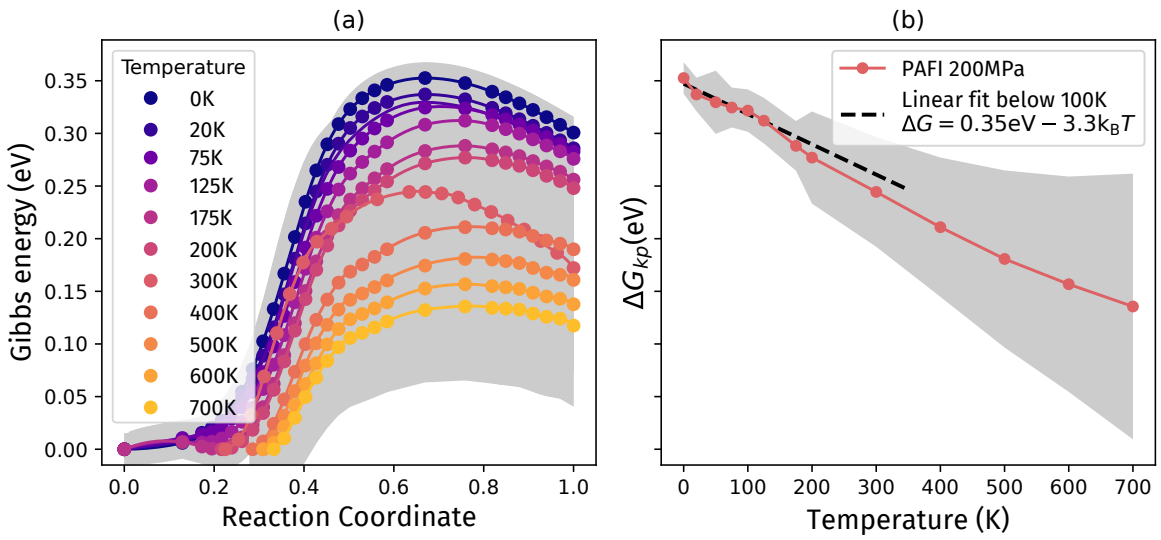


Figure 3.11: **Minimum Gibbs free energy paths associated with the nucleation of a kink pair under 200 MPa in Fe, at different temperatures.** (a) MGEP profiles: PAFI free energy data (symbols) and corresponding splines (lines). (b) Temperature evolution of the Gibbs energy of activation. A linear regression in the domain below 100 K is shown as a dashed line. Both plots share the same $y$ axis.

barriers such as those presented in Fig. 3.11 (a). In Fig. 3.10, the values of $\Delta G_{kp}$ computed with the PAFI method are also compared to the harmonic prediction obtained by diagonalization of the Hessian matrix (see Sec. 1.3). It appears that both methods are in agreement close to zero Kelvin, but quickly diverge as $\Delta G_{kp}$ becomes non-linear even at low temperature ($T \gtrsim 20$ K). This unexpected behavior means that harmonic entropy calculations, a well-established method for computing the low-temperature entropy (Vineyard, 1957) would lead to a strong overestimation of the activation entropy in this case, even at low temperature. The curvature of the energy landscape at the initial and activated states can therefore only be used very locally, limiting the harmonic regime to very low temperatures. When temperature allows the system to visit neighboring states around the equilibrium position, it experiences a curvature that differs from the one of an idealized harmonic surface. This overestimation of the entropy is likely due to a roughness of the potential energy landscape predicted by Proville potential and to locally flat regions in the energy landscape of the interatomic potential, which could be an artefact of the interatomic potential.

Nevertheless, the observed non-linearities remain small compared to the variations caused by the stress or the temperature. In Fig 3.11, it can be seen that the overall curves remain close to a linear behavior at low temperature. We have therefore linearized the $\Delta G_{kp}$ data at

temperatures below 100 K, giving an approximation of $\Delta S = -\partial G_{kp}/\partial T$ assimilated to a constant. This close-to-linear domain is alike a harmonic regime, with the difference that it does not directly derive from the vibrational modes around the initial and activated states. We also emphasise how the small deviations from linearity at low temperatures affect the computed activation entropy, making such calculations very challenging. To be able to measure these small variations in Fig. 3.10, we improved the precision of the Gibbs energy calculations by increasing the number of independent samplings, resulting in a narrow uncertainty domain (represented by a light grey region in Fig. 3.12) that allows to capture all non-linearities, but with a high computational load. The linearization that we propose can thus also be seen as a pragmatic approach to save computational resources by neglecting small non-linearities.

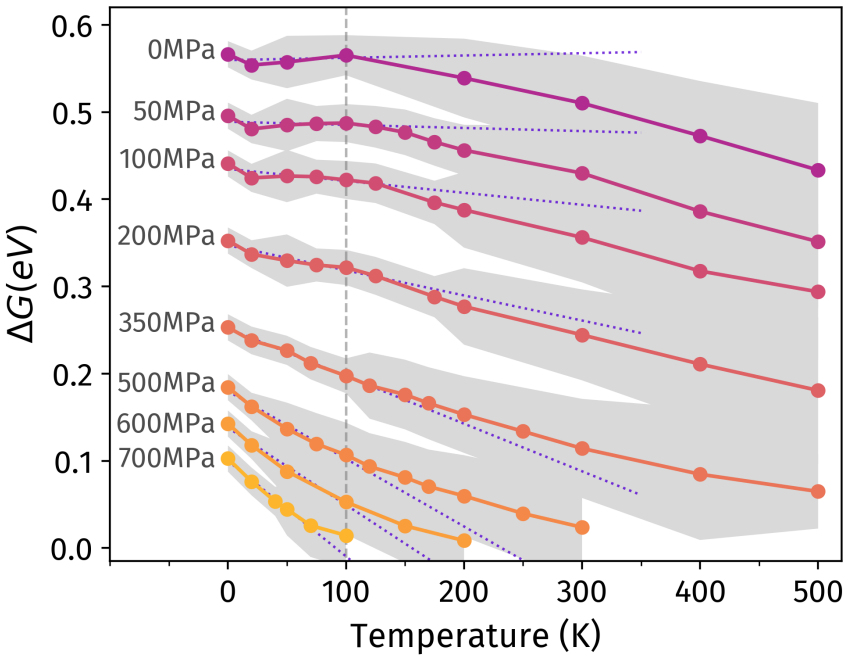


Figure 3.12: **Gibbs free energy of nucleation of a kink pair in iron as a function of temperature.** PAFI data obtained for each level of stress are shown as symbols. Linear regressions below 100 K are shown as (dotted lines).

In Fig. 3.12, we present values of $\Delta G_{kp}$ computed over a large range of stresses and temperatures. As expected, $\Delta G_{kp}$ decreases when the temperature or the applied stress increase. Also note that the sampling error is larger than in Fig 3.10, as less sampling repetitions were realized to save computation time and explore more stress/temperature conditions. For all tested values of the stress, the variations of $\Delta G_{kp}$ remain close to linear below 100 K, as highlighted by the blue dotted lines. The *effective* activation entropy $\Delta S_{reg}$ obtained from

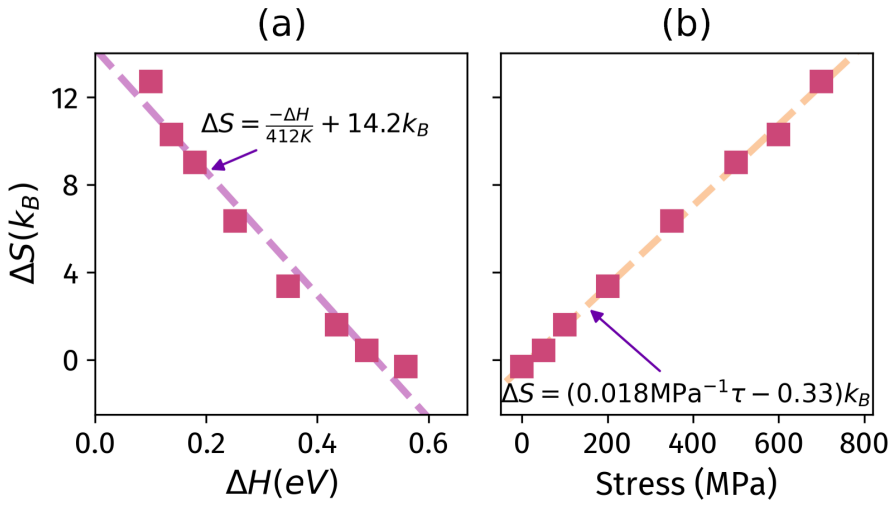


Figure 3.13: **Effective activation entropy $\Delta S$ as a function of (a) the activation enthalpy $\Delta H_{kp}$ and (b) the shear stress $\tau$.** The slopes of linear regressions of Fig. 3.12 are plotted as a function of the activation enthalpy in (a) and stress in (b) (square symbols), and fitted to: (a) an inverse Meyer-Neldel entropy-enthalpy relation (Eq. 3.18), (b) a linear stress-activation entropy relation.

low-temperature linear regressions is reported in Fig. 3.13 as a function of both the activation enthalpy $\Delta H_{kp}$ and the stress. It appears that $\Delta S_{reg}$ varies by several $k_B$, which contrasts with the approximation of a constant activation entropy. In addition, a clear proportionality is observed in both cases, which can be seen as two manifestations of a same effect, as $\Delta H_{kp}$ varies close to linearly with the stress (see Fig. 3.3). At low temperature, $\Delta S$ can therefore be expressed either as $\Delta S = \frac{-\Delta H_{kp}}{T_{MN}} + \Delta S_0$ with $T_{MN}$ positive, corresponding to an inverse Meyer Neldel behavior, or as a function of the stress $\Delta S = \alpha\tau + \Delta S_0$. The parameterization of both equations is presented in Fig. 3.13. Interestingly, the inverse Meyer Neldel behavior seen at low temperature corresponds to a *reinforcement* effect between enthalpy and entropy, in contrast to the classical compensation effect.

In Fig. 3.14, we implemented an *inverse* Meyer Neldel law in the glide models of Sec. 3.2.2 using the parameterized value of $T_{MN}$ and $\Delta S_0$, respectively 484 K and $12.3k_B$. Again, both models presented side-by-side use the same expression of $\Delta G_{kp}$. With the inverse MN law, both models yield a satisfactory agreement with MD data. The thermally activated model appears slightly more accurate, and its predictions go through the error bar of most data points. We emphasize that this result is obtained with no adjustable parameter in the case of the model of Po *et al.*, and with $\nu$ as the only adjustable parameter in the case of the thermally activated model (which was set to the same value $\nu = 5 \times 10^{10}$ s$^{-1}$ throughout this

chapter). Both models are reasonably accurate within the entire range of temperature and shear rates presented here. These results suggest that the temperature dependence of the flow stress seen in low temperature MD simulations can be explained within the framework of the harmonic TST, using the inverse MN law. At higher temperature, anharmonicity is expected, as a deviation from linearity of the Gibbs energy is seen in Fig. 3.12.

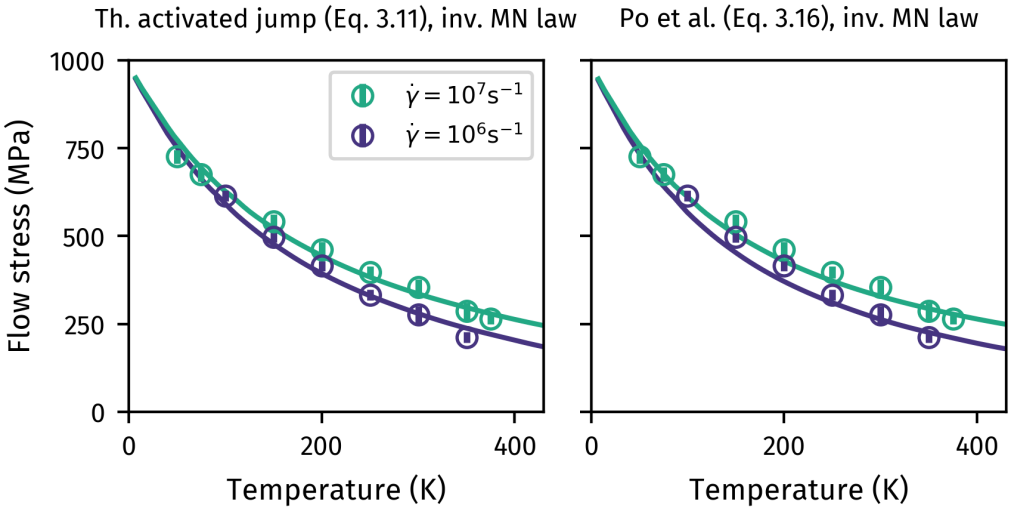


Figure 3.14: **MD flow stress data compared to models predictions using an *inverse* Meyer Neldel law.** Each subplot presents the predictions of a model (thermally activated on the left, Po *et al.* on the right), for two different simulation conditions (continuous curves), and compared to corresponding MD simulations (symbols, same color corresponds to same conditions).

Beyond the linear regime, a deviation from linearity is indeed observed in Fig. 3.12, corresponding to an *anharmonic regime* where $\Delta G_{kp}$ decreases non-linearly. We have checked that for the moderate stresses and temperatures considered here, both usually discussed anharmonic effects, i.e. thermal dilatation and weakening of the elastic moduli (Ryu et al., 2011), do not affect the energy barriers. The main effect is probably a widening of the activated kink pair (Swinburne and Marinica, 2018), which results in a deviation of the MGEP at finite temperature from the zero-Kelvin MEP. Interestingly, we see in Fig. 3.12 that at low applied stresses, $\Delta G_{kp}$ decreases faster than the linear regression while it is the opposite at high applied stresses. This implies that using a linear approximation at high temperatures may result in either over- or underestimating the dislocation velocity depending on the applied stress, resulting in erroneous curvature of flow stress curves in Fig. 3.14 compared to MD.

The evolution of $\Delta G_{kp}$ as a function of the applied stress is shown in Fig 3.15. At all

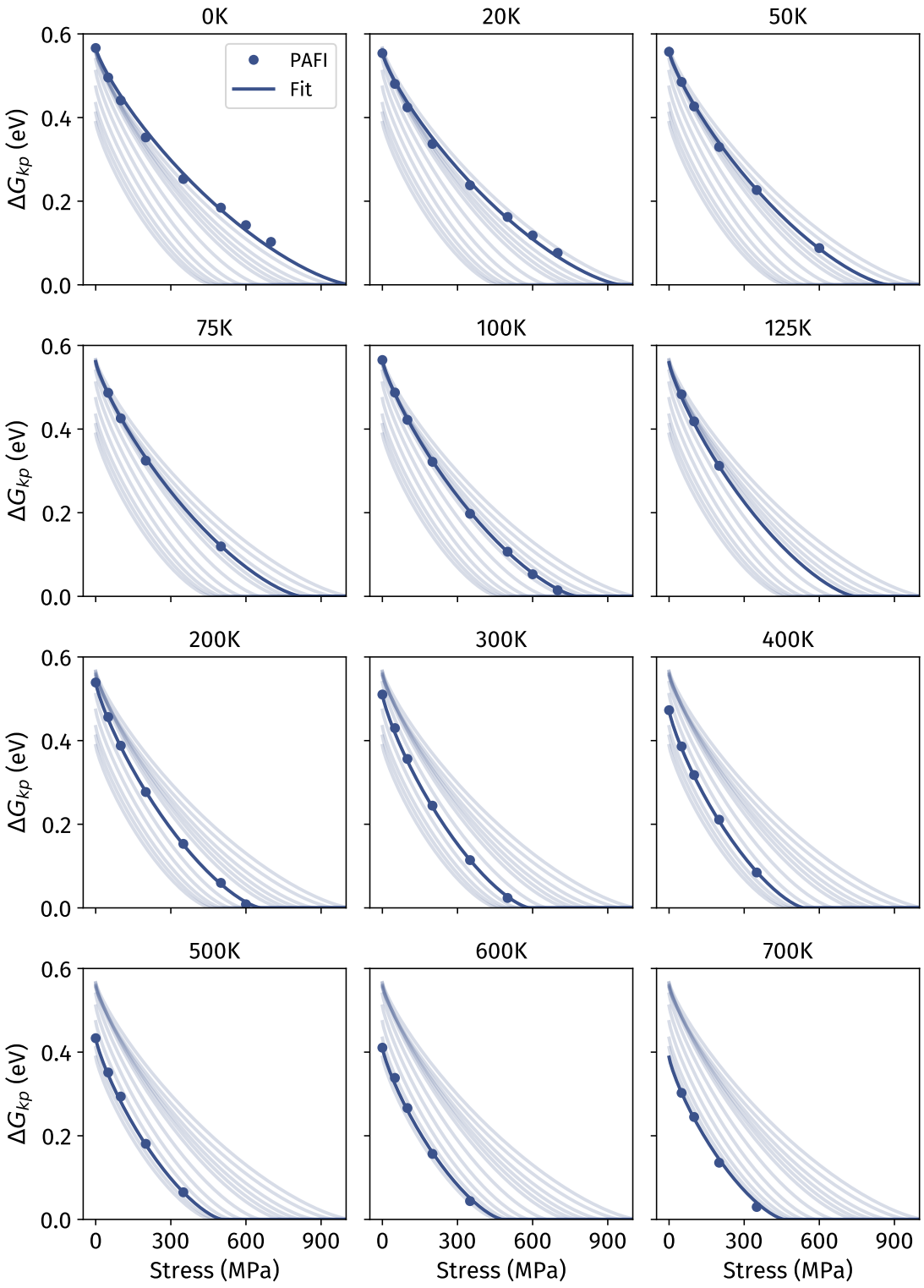


Figure 3.15: **Gibbs free energy of nucleation of a kink pair as a function of stress.** PAFI data (symbols) is fitted to Eq. 3.24, giving a set of parameters given in Tab 3.1. Each temperature data is represented in a different subplot, with the corresponding fit shown as a dark solid line. All curves are reported in the background of other sublots as light gray lines for easier comparison.

temperatures (including the anharmonic regime), the data can be accurately fitted by a phenomenological approach, using a modified Kocks law (Kocks et al., 1975):

$$\Delta G_{kp}(\tau, T) = \Delta G_0(T)\left(1 - \left(\frac{\tau}{\tau_P(T)}\right)^p\right)^q, \tag{3.24}$$

with:

$$\tau_P(T) = \frac{a}{T + T_0} + b, \tag{3.25}$$

and $\Delta G_0(T) = \Delta G_0 - T \times G_T$, with $\Delta G_0 = 0.6\,\mathrm{eV}$ and $G_T = 2 \times 10^{-4}\,\mathrm{eV\,K^{-1}}$. Here, $\tau_P(T)$ is analogous to the zero-temperature Peierls stress for a finite temperature $T$, since it verifies

$$\Delta G\big(\tau_P(T), T\big) = 0. \tag{3.26}$$

At low temperature (*i.e.* below $\sim$ 100 K), $\tau_P(T)$ is strongly temperature-dependent, and becomes constant at higher temperature, as reflected by Eq. 3.25. The obtained set of fitting parameters $a, b, T_0, p, q$ in Fe are given in Tab. 3.1. For temperatures below 100 K, a linear fit gives the best match to the data. The corresponding fit is shown as a function of the stress in Fig. 3.15. It can be seen that the proposed expression is able to fit Gibbs energy data within a wide range of temperature and stress in the anharmonic domain. With Eq. 3.24 and 3.25, we propose a phenomenological expression of $\Delta G_{kp}(\tau, T)$ that accounts for anharmonic effects encountered at high temperature.

We used Eq. 3.24 to compute $\Delta G_{kp}$ and determine the flow stress of iron using the two models previously discussed, with the results presented in Fig. 3.16. Following the approach of Fig. 3.14, models predictions are compared with MD data. As can be seen, the agreement of the anharmonic models with MD data is very satisfactory, and data points are well predicted by the models. We note that the agreement with MD is only very slightly improved compared to the harmonic inverse MN law, which appears accurate enough, especially considering its great simplicity. However, at higher temperature, we expect the anharmonic model to better predict the flow stress. But MD simulations could not be conducted at higher temperature to verify this assumption, due to the instability of the dislocation, which tends to exit the simulation cell through the free surfaces when the temperature reaches 400 K in our simulation setup.

The values of $\Delta G_{kp}$ obtained with PAFI (Eq. 3.24) can also be used to compare the predictions of the different models to experimental flow stress data, *e.g.* from Brunner and Diehl (1991). It must be noted that in the low temperature limit, a well-known discrepancy appears

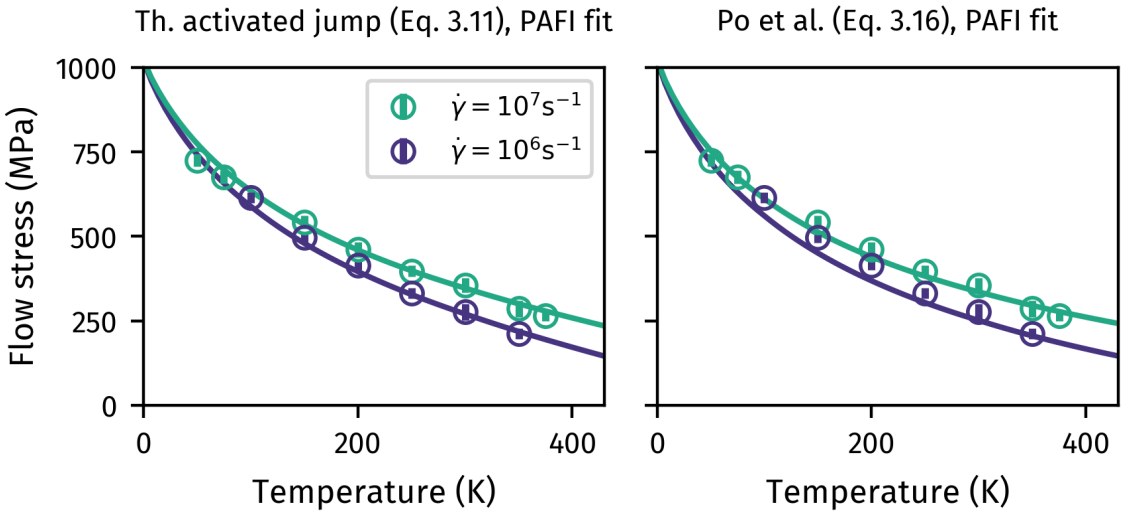


Figure 3.16: **MD flow stress data compared to models predictions using our Gibbs free energy calculations.** Each subplot presents the predictions of a model (thermally activated on the left, Po *et al.* on the right), for two different simulation conditions (continuous curves), and compared to corresponding MD simulations (symbols, same color corresponds to same conditions).

| Parameter | Value | Unit |
|---|---|---|
| $a$ | $1.44 \times 10^5$ | MPa/K |
| $b$ | 299 | MPa |
| $T_0$ | 200 | K |
| $p$ | 0.83 | – |
| $q$ | 1.42 | – |

Table 3.1: **Fitting parameters obtained by adjusting Eq. 3.24 to PAFI data in iron.**

between the 0 K extrapolation of experimental flow stress data, which is close to 0.4 GPa in iron (Kubamoto et al., 1979), and predictions of classical TST models, which are close to 1 GPa (Fig. 3.3). Several authors proposed to correct this discrepancy either phenomenologically (Domain and Monnet, 2005) or by accounting for the effect of dislocations junctions (Bulatov and Cai, 2002), collective dislocation dynamics effects (Gröger and Vitek, 2007) or quantum effects (Proville et al., 2012). While these processes are of great importance, their integration is beyond the scope of the present work. In order to compare relative variations, we plot experimental and simulated data on separate scales (Clouet et al., 2021). Another caveat of comparison to experimental data is the estimation of the segment length $L$ and dislocation density $\rho$ (Brunner and Diehl, 1991). Here, we take $L = 1\,\mu\text{m}$, $\rho = 1 \times 10^{12}\,\text{m}^{-1}$, $\dot{\gamma} = 8.5 \times 10^{-4}\,\text{s}^{-1}$ and use value of $\nu = 5 \times 10^{10}\,\text{s}^{-1}$ used previously.

In Fig 3.17, we compare experimental flow stress data to the predictions of both dislocation glide models, based on our parameterization of Eq. 3.24. Both models yield similar predictions in this case, as we have $L/\lambda \sim 10^{-2}$, *i.e.* glide is limited by kink pair nucleation. It can be seen that this parameterization allows the models to reproduce well the overall *relative* evolution of the experimental flow stress. The *athermal* temperature $T_C$ which marks the end of the thermally activated regime is well defined with both models with this set of conditions, even though the definition of $T_C$ has been discussed in this chapter (see Sec. 3.2.4). The difference between model predictions and experiments is mainly due to an underestimation of the athermal temperature, leading to a discrepancy that gets larger with increasing temperature. While this result is encouraging for the integration of entropic and anharmonic effects in kinetic models of dislocation glide, a more realistic comparison to experimental data would benefit from the integration of the low-temperature effects mentioned above, as well as the use of a more realistic interatomic potential. In addition, neither our implementation of the thermally activated model nor of the model of Po *et al.* include non-schmid effects which are well-known to play a role in experimental conditions (Spitzig and Keh, 1970; Hale et al., 2015; Stukowski et al., 2015; Kraych et al., 2019; Clouet et al., 2021).

## 3.4 Conclusions

In this chapter, we discussed different dislocation velocity models and tested their validity using MD simulations. The tested models notably differ by their complexity, ranging from a simple forward-jump model to the more comprehensive approach of Po et al. (2016) which takes into account the kink migration velocity and the equilibrium density of kink pairs along

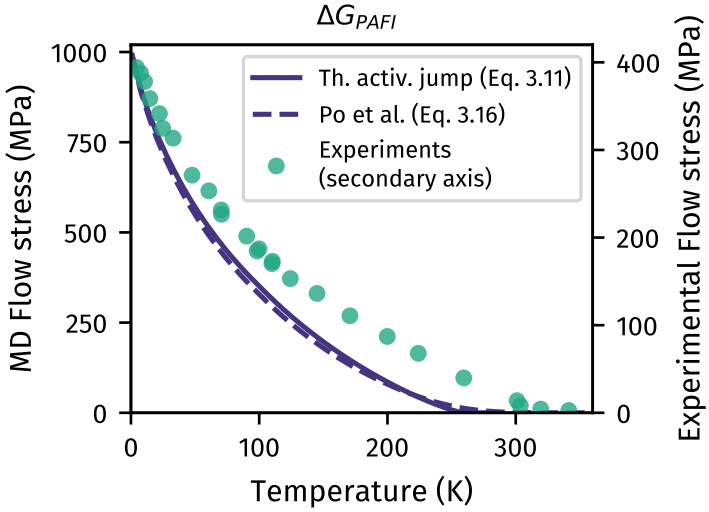


Figure 3.17: **Experimental flow stress compared to models predictions.** Experimental data from Brunner and Diehl (1991) is compared to the predictions of the thermally activated model, which uses our parameterization of Eq. 3.24. Note that experimental data is plotted on a separate axis to account for the usual low-temperature discrepancy between TST models and experiments.

long segments.

When comparing to MD simulations, the accuracy of the predictions depends for a larger part on the assumptions used for the calculation of $\Delta G_{kp}$, often more than on the velocity model itself. Comparison to MD also shows that common assumptions, such as a constant entropy, or the Meyer-Neldel law, fail to reproduce the flow stress of iron at high temperatures. We used a novel free energy integration method (PAFI) to evaluate $\Delta G_{kp}$ beyond the harmonic domain, showing strong anharmonic effects, and non-linearity at temperatures as low as 20 K that quickly diverge from the predictions of HTST methods based on a diagonalization of the Hessian matrix. Using the PAFI method, the Gibbs energy was computed in a large range of stresses and temperatures and fitted with simple laws to be implemented in kinetic models. The flow stress predicted using this fitted law is in excellent agreement with MD simulations up to temperatures that are above the room temperature.

PAFI data also show that the Gibbs activation energy tends to follow an inverse Meyer-Neldel behavior at temperatures below 100 K. Implementing an inverse Meyer-Neldel law parameterized on our Gibbs energy data yields a satisfactory agreement with flow stress values obtained from MD simulations up to the high temperatures. Complementary analysis of atomic vibration modes obtained by diagonalization of the Hessian matrix was performed

following the approach of Gelin et al. (2020) as an attempt to understand the physical origins of this inverse Meyer-Neldel behavior. The results show that when the applied stress (and conversely, the enthalpy) changes, the vibrational modes of the iron matrix (*i.e.* delocalized in the simulation cell) are affected. We observe that in contrast to the observations of Gelin et al. (2020), the softening peak seen in the difference of vibrational density of states (VDOS) between the initial and activated states is increased when the enthalpy *decreases*, resulting in an *increase* of the activation entropy. However, the strong deviation of the Gibbs energy from the HTST prediction starting at 20 K raises questions on the validity of these observations above very low temperatures. As the distance between the initial and activated states in configurational space is reduced when the stress is close to the Peierls stress (as the critical kink is then only a small buldge, as seen in Fig. 3.2), we expect the activation entropy to decrease in the high stress domain. We were able to confirm this prediction with complementary HTST calculations using the EAM4 potential for tungsten (Marinica et al., 2013). But the same calculations conducted in iron revealed that $\Delta S$ increases even more stiffly under a high stress, corresponding to a softening of vibration modes, which is likely a local artefact of the interatomic potential.

At this point, this work is limited by the realism of the Proville interatomic potential. The strong anharmonicity of the potential at moderate temperature, as well as the non-linearity that appears at low temperature raise questions on the realism of the potential. These results should thus be confirmed with other interatomic potentials for iron that are valid for the simulation of dislocations, such as the recently developed machine learning-based potentials from Goryaeva et al. (2021). These potentials show an excellent agreement with the *ab initio* Peierls barrier and kink-pair nucleation energies derived from *ab initio*-parameterized line tension models.

## 3.5 Perspectives for the PAFI method

The PAFI method has shown a great efficiency for free-energy calculations, compared either to classical harmonic approaches or to recent developments in free energy calculation methods (Grabowski and Zotov, 2021). In the future, this method could be generalized to a broad range of thermally activated processes, allowing a better understanding of these processes as well as more accurate predictions. Using this type of method, new interatomic potentials could be automatically compared to *free* energy data obtained *e.g.* with ab initio methods (Ackland, 2002; Zhang et al., 2018; Grabowski et al., 2019), while it is common to

benchmark potentials on zero-kelvin properties, which offers no guarantee that predictions remain valid at high temperature.

Several improvements to the PAFI method could be proposed to make it more easily usable by the community and faster. A first limitation of the method in its current state is its sensitivity to the density of knots along the initial minimum energy path (MEP), which must be sufficiently high in regions where the free energy varies strongly, to avoid integration error that would be caused by discontinuities of the free energy gradient. Here, we avoided this issue by using a large number (20-30) of NEB replicas and PAFI hyperplanes to compute each barrier, but this approach is highly inefficient and a similar result could be obained with less hyperplanes placed at optimal positions. One difficulty is that the position of the regions where the free energy varies strongly cannot be anticipated from 0 K calulations, as the position of the initial and transition states are typically shifted with increasing temperature (see Fig. 3.18). This issue could be addressed by adding knots on-the-fly at optimal positions where large free energy gaps remain, *e.g.* by adapting approaches used for adaptative NEB path construction (Kolsbjerg et al., 2016). The hyperplane associated with a new knot is then defined by spline interpolation of the MEP, or using the free end NEB method for a more precise result, which allows to find a minimum energy path between non-equilibrium positions.

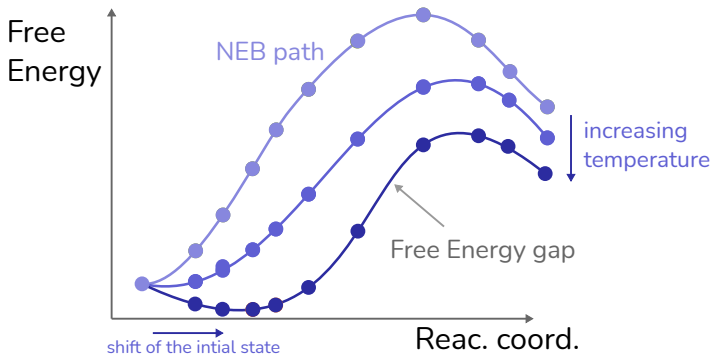


Figure 3.18: **Sketch of the distribution of knots along a free energy barrier at different temperatures.** As the temperature increases, the MFEP is more and more deviated from the MEP and the difference between successive knots can become large.

Another current limitation of the method is the time nedded to perform the several hundreds of independent samplings that are necessary to compute a barrier with a good precision. The parallelization scheme of PAFI, shown in Fig. 1.6, allows to run several samplings on the same hyperplane simultaneously, each on a different *worker* (group of CPUs), connected

by the Message Passing Interface (MPI) with a perfect parallel scaling (*i.e.* no time is lost in communication between workers, as they are fully independent). While offering a simple way of starting a large number of simulations simultaneously and to collect their results, this approach uses a fixed number of workers, meaning that all CPUs have to be requested at once in shared high performance computing (HPC) platforms. On a busy computing platform, this results in a long queue time until all requested CPUs are available. On the other hand, if more CPUs are available on the plateform, only the requested number is used, thus not fully exploiting the available resources. These limitations could be lifted by submitting an independent job for each worker (or groups of workers) of all hyperplanes to the schedueler at once, which will then be allocated depending on the available resources. This would in addition allow to use computing nodes that are not designed for distributed parallel calculations, *i.e.* which are not connected by a high-performance network such as an Infiniband network or do not have a MPI library installed. Workflow managers (see *e.g.* Rocklin (2015); Huber et al. (2020); Köster et al. (2021)) could be used to automatically submit and track jobs on HPC platfoms with minimum code addings to PAFI.

# 4 Screw dislocation pinning by interstitial carbon in iron

The presence of interstitial carbon atoms can affect the thermally-activated nucleation and subsequent propagation of kink-pairs, even with low concentrations of solutes (Caillard, 2011). While theories of solute hardening are well established in substitutional alloys (Patinet and Proville, 2008; Varvenne et al., 2017), their application to interstitials remains difficult due to strong solute-dislocation interactions in the core region. In this chapter, we investigate the effect of interstitial carbon on dislocation mobility in Fe-C with atomistic simulations, confirming a powerful locking effect of carbon. We propose a model of dislocation pinning based on our model of dislocation glide in Fe (Chap. 3), which explains the origin of the strengthening effect induced by carbon.

## 4.1 Introduction

The addition of carbon in iron to improve mechanical properties is at the basis of steel metallurgy (Berns and Theisen, 2008). For dilute alloys, the change of mechanical properties at low temperature is related to the interaction between solute atoms and dislocations[1]. In substitutional alloys, solutes have a low mobility and dislocations can be considered as moving through a field of fixed obstacles (Zhao and Marian, 2018). With interstitials on the other hand, like carbon in iron, solutes are mobile and able to diffuse. The elastic field of dislocations favors their segregation around dislocation lines, forming Cottrell atmospheres (Cottrell and Bilby, 1949) that were evidenced experimentally using atom probe techniques (Blavette et al., 1999; Wilde et al., 2000). Cottrell atmospheres can greatly reduce the mobility of dislocations, which necessitate a high stress to escape their atmosphere and be set into motion (Schoeck and Seeger, 1959). This effect is known as static strain ageing, and is

[1] In more concentrated alloys, other phases can appear depending on their stability as predicted by the phase diagram. Here, we focus on low-carbon ferritic steel.

typically associated with an important yield drop at the beginning of the plastic domain (Kubin et al., 1992), caused by the collective depinning of dislocations from carbon. In a domain of deformation rate and temperature where dislocations and carbon move at a comparable velocity, a regime of *serrated flow* is observed (dynamic strain ageing) where atmospheres are able to catch up with dislocations before they can move any further (Zhao et al., 2020) (see *e.g.* Fig. 4.1). Cottrell atmosphere formation kinetics and mobility are therefore important to predict the mechanical properties of aged steel and the plastic flow in the serrated flow regime. Atomistic simulations of their formation using atomistic Monte Carlo approaches were conducted by Waseda et al. (2017) and Candela et al. (2020) (Fig. 4.2), providing insights on the filling of lattice sites near the dislocation. Molecular dynamics simulations of decorated dislocations expose a powerful pinning effect of carbon, which increases the unpinning stress more than 10-fold compared to a solid solution of low concentration (Veiga et al., 2015).

When solutes are homogeneously distributed in solid solution, a hardening and a softening are observed experimentally depending on the temperature domain (Caillard, 2011), as represented schematically in Fig. 4.3.

Several solute strengthening theories were proposed to explain the strengthening in random solid solutions of substitutional atoms, based on interactions between dislocations and solutes at the atomic scale (Patinet and Proville, 2008; Varvenne et al., 2017). A classical conception of hardening, which is typical of fcc metals, is attributed to the bowing of elastic dislocation lines between pinning points under the applied stress (Foreman and Makin, 1966), which increases until it reaches either a critical angle $\phi_C$ for weak obstacles, or until segments on each side of the obstacle collide, resulting in their annihilation, in the case of strong obstacles. In bcc metals, due a large Peierls barrier, this mechanism does not apply as straight dislocation segments are favored and glide is allowed by the kink pair mechanism (see Sec. 3.1). In this case, strengthening can be explained by an attractive interaction between the solutes and the dislocation, impeding dislocation glide. Several authors implemented the solute-dislocation interaction in analytical models of substitutional alloys (Labusch, 1970; Suzuki et al., 1991; Patinet and Proville, 2008; Varvenne et al., 2017; LaRosa et al., 2019; Maresca and Curtin, 2020; Rao et al., 2021; Ghafarollahi et al., 2019), or simulations based on the Kinetic Monte Carlo (KMC) method (Zhao and Marian, 2018). Recently, Zhao et al. (2020) proposed KMC simulations of interstitial W-O alloys, parameterized on DFT simulations (Zhao et al., 2019), that were able to reproduce dynamical strain ageing behavior. A central parameter in these approaches is the dislocation–solute binding energy which depends on the interatomic potential used. Predictions of different interatomic potentials are compared to *ab initio* values in Sec. 2.3.1.

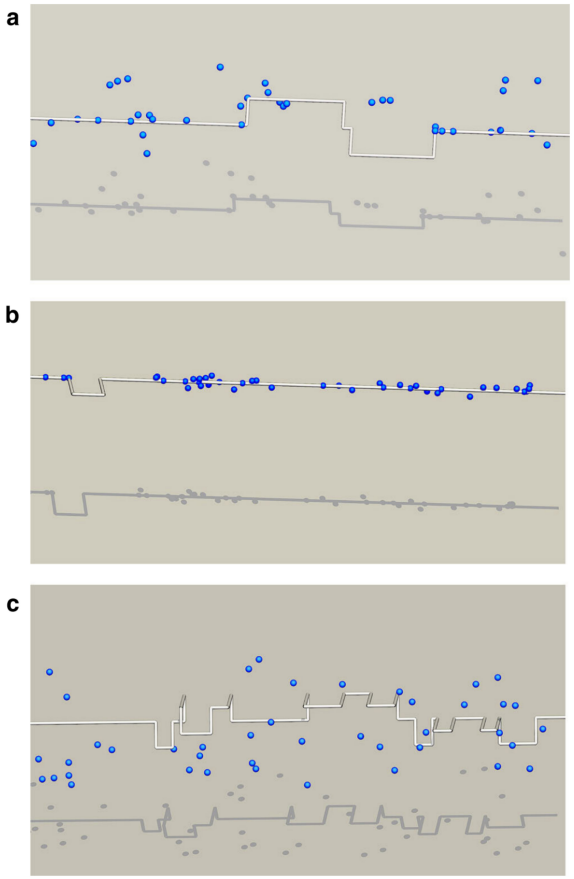


Figure 4.1: **Snapshots from KMC simulations of a screw dislocation in tungsten interacting with interstitial oxygen atoms**, showing different dynamical regimes: (a) with fast solute diffusion, the dislocation and solutes motion are uncorrelated, (b) for comparable solutes and dislocation velocities, solutes are able to segregate to the core and pin the dislocation before it can unpin and move further, (c) when solutes diffusion is slow, the dislocation moves in a field of static obstacles. Reproduced from (Zhao et al., 2020).

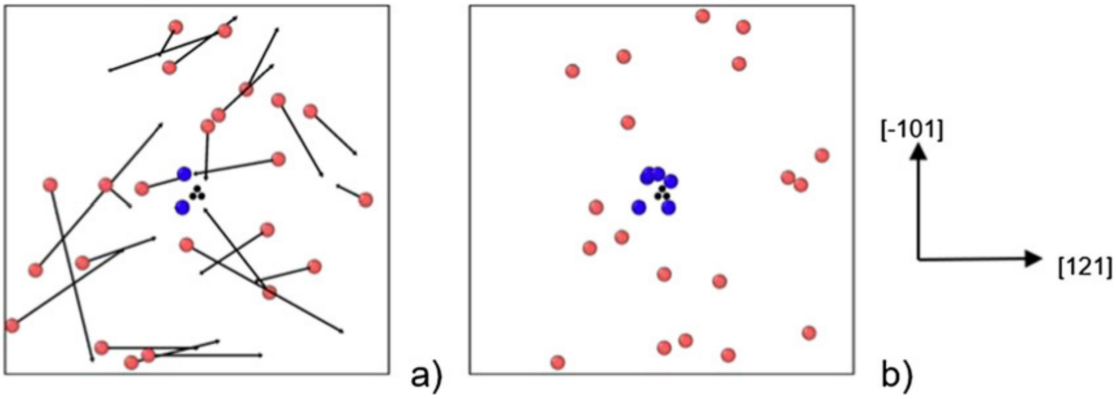


Figure 4.2: Initial (a) and final (b) configurations of a mixed-lattice kinetic Monte Carlo simulation containing a screw dislocation (the core is represented by three black dots) and 25 C atoms (spheres) at 300 K. Black arrows in (a) represent the displacement of atoms between (a) and (b). Reproduced from (Candela et al., 2020).

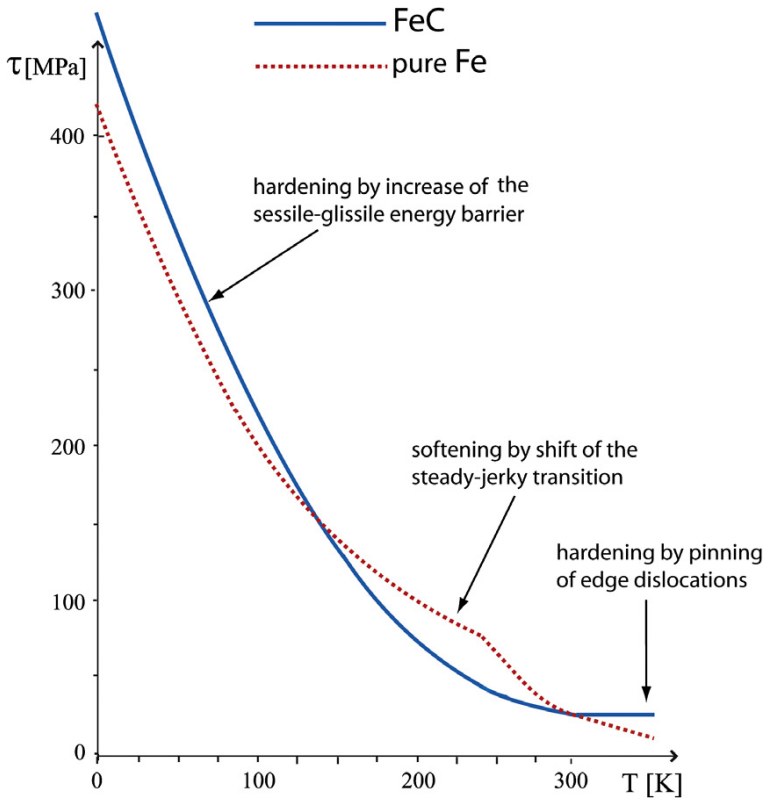


Figure 4.3: **Softening and hardening effects due to carbon addition.** Figure reproduced from Caillard (2011).

With interstitials, local effects of solutes on the dislocation core were evidenced in DFT calculations (Ventelon et al., 2015; Lüthi et al., 2018), presented in Fig. 2.3. It consists in the stabilization of a prismatic core structure unstable in pure Fe and other bcc metals (Lüthi et al., 2017), evidenced with C and with other interstitial solutes in iron (Lüthi et al., 2018). Due to its low mobility (Lüthi, 2017), this reconstructed, prismatic core is expected to control the plasticity of bcc interstitial alloys when solutes are mobile and decorate the dislocations (Hachet et al., 2020). But DFT simulations remain limited by their high computational cost as studies at a larger scale are necessary.

MD simulations were also used to study the effect of carbon on non-screw dislocations in iron Tapasa et al. (2007); Veiga et al. (2011); Waseda et al. (2017); Zamzamian et al. (2019); Ishii et al. (2013), but simulating its effect on screw dislocations remains challenging. Screw dislocation locking by carbon was simulated using MD Veiga et al. (2015); Khater et al. (2014) and energetic computations Becquart et al. (2007); Clouet et al. (2008); Hanlumyuang et al. (2010), showing a dramatic reduction of dislocation mobility, linked to a higher kink-pair nucleation enthalpy Wang et al. (2019). However, the interatomic potentials used in these studies show a poor agreement with dislocation properties in iron computed with DFT —including the shape and height of the Peierls barrier— which makes their conclusions open to question. In chapter 2, we compared Fe-C potentials from the literature and proposed a novel potential which allows the simulation of screw dislocations interacting with carbon. In Chap. 3, we investigated the temperature dependance of the flow stress in iron, and determined that using this potential, the harmonic approximation remains valid up to the ambiant temperature in typical MD simulations conditions. At higher temperatures in the Fe-C system, a different regime of deformation is seen experimentally, attributed to the effect of edge dislocations that become less mobile than screws (Caillard, 2011).

Based on the hybrid interatomic potential developed in Chap. 2, it becomes possible to simulate by MD the glide of screw dislocations in random solid solutions of C atoms, at low temperature. Simulations of a full solid solution are used to assess the importance of short-range core interactions compared to long-range elastic ones. A detailed analysis of an elementary pinning configuration, where a screw dislocation interacts with C atoms of varying separation is also performed. For this, we use a combination of MD simulations, saddle-point search methods and a statistical model of the unpinning stress based on the harmonic transition state theory (HTST).

## 4.2 Dislocation mobility in a solid solution

We start by simulating the glide of a screw dislocation interacting with a random solid solution of C atoms. In order to observe several pinning-unpinning events in the course of a MD simulation, and the combined effect of several C atoms along the dislocation, we set the concentration to 0.52 at%, i.e. 1000 solute atoms in a box containing 192000 Fe atoms. It was created by inserting carbon atoms in octahedral sites randomly selected in the PAD simulation cell. Considering the short simulated time (a few nanoseconds) and the investigated temperatures, carbon atoms are not able to diffuse and are considered immobile in the rest of this chapter.

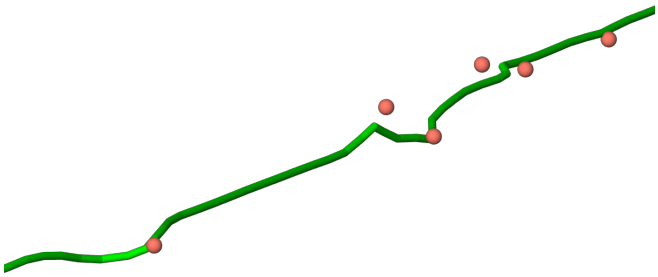

Figure 4.4: **Dislocation line (green) adopting a complex three-dimensional kinked structure in presence of carbon atoms (red spheres).** Only the solutes closest to the dislocation are represented for clarity. The dislocation line was identified using the DXA algorithm (Stukowski et al., 2012).

Using the DXA algorithm (Stukowski et al., 2012), we can visualize the position of the dislocation line in MD simulations. Due to the high carbon-dislocation binding energy, nucleation of kink-pairs in directions where carbon atoms are present is favoured, which includes cross-slip planes. This results in strongly locked configurations, as illustrated in Fig.4.4, where the dislocation line connects all neighbouring C atoms, with segments extended in different planes giving the dislocation a three-dimensional shape.

Typical stress-strain curves are shown in Fig. 4.5 (a). As shear is increased at a constant rate, the internal stress raises linearly before the flow stress is reached, or each time the dislocation is in a pinned configuration. After each unpinning event, the stress drops as the dislocation rapidly glides in the cell to the next obstacle, resulting in a strongly serrated stress-strain curve. Unpinning stresses are on the order of 600 MPa at 300 K, compared to a flow stress of about 350 MPa in pure Fe (the stress-strain curve in pure Fe is shown in gray

in Fig. 4.5 (a)). The strengthening can emerge from three mechanisms in the region of the core (Maresca and Curtin, 2020): i) solutes block the kink migration along the line, ii) the interaction between kinks in different planes result in cross-kink pinning, and iii) the nucleation of double-kinks on segments between solutes can become harder, especially with a reconstructed dislocation core (see section 4.3.2). The local conversion of the dislocation core to a prismatic structure in the neighbourhood of carbon atoms is indeed observed in dynamic simulations, as illustrated in Fig. 4.6. As the interplay between the different strengthening mecanisms make solid solution simulations too complex to analyse, simplifications are needed. In order to confirm the importance of short-range solute-dislocation interactions, we artificially created a carbon-free volume around the glide plane as illustrated in Fig. 4.5 (b). Solute atoms outside this volume are left unchanged between the different simulations. In Fig. 4.5 (a), we compare the stress-strain curves obtained with a full solid solution ($n_{planes} = 0$), and a carbon-depleted zone around the dislocation glide plane comprised of $n_{planes}$ atomic planes on both sides. In the case $n_{planes} = 2$, the vicinity of carbon atoms attracts the dislocation, which cross slips and gets pinned to the carbon, resulting in a strenghtening that is comparable to the full solid solution. When $n_{planes}$ is larger than 4 (corresponding to approximately 8 Å), the stress level reveals no significant strengthening in comparison to pure iron (green curve). This advocates for a pinning mainly controlled by short-range interactions.

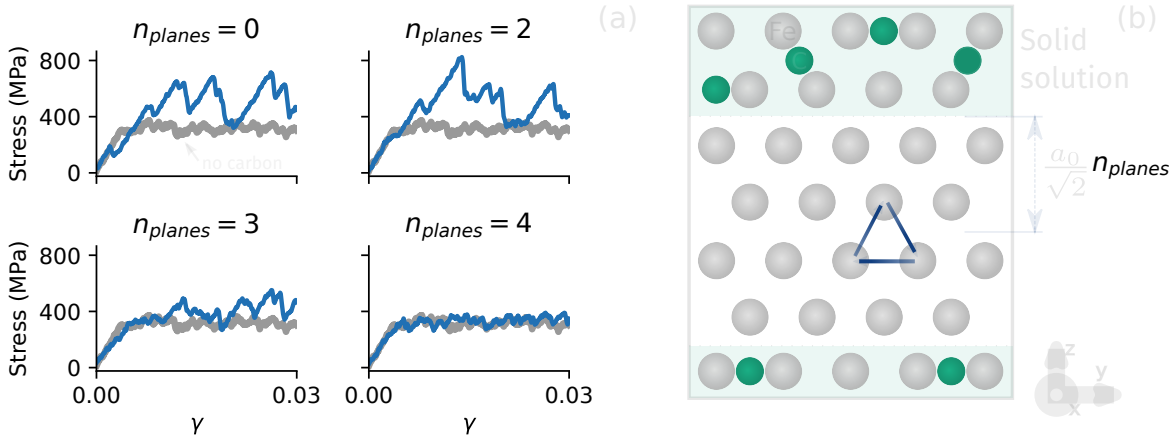


Figure 4.5: **Constant shear rate simulations with a carbon-depleted zone around the glide plane.** (a) Stress-strain curves during constant shear-rate MD simulations of random solid solutions at 300 K. Blue lines represent simulations in which a carbon depleted zone of $n_{planes}$ atomic planes above and below the glide plane was created, as illustrated in (b). The carbon concentration is 0.52 at when $n_{planes} = 0$. The gray line in (a) represents the same deformation test conducted in pure Fe.

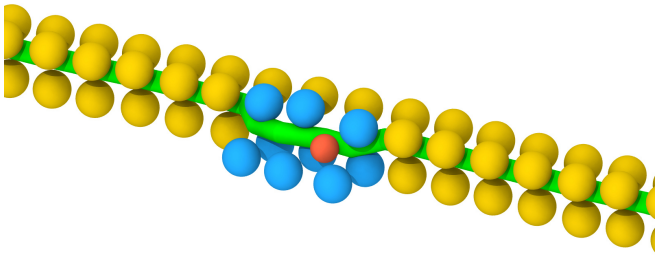

Figure 4.6: **Local conversion of the screw dislocation core during a dynamical simulation.** The smaller red atom is a carbon atom, while all others are iron atoms. Iron atoms that adopt a distorted prismatic structure near the carbon atom, are highlighted in blue. The dislocation line obtained using the DXA algorithm is shown in green. For clarity, only core atoms are shown.

## 4.3 Unpinning from an array of C atoms

Given the complexity of dislocation glide in a random solid solution seen in previous section, we defined a model system when a screw dislocation detaches from an array of carbon atoms directly located in its core. This allows to exclude cross-kink pinning, and the effect of mid- and long-range interactions, to focus on the elementary unpinning process. For these simulations, two C atoms were inserted in second-nearest octahedral positions along the dislocation line (denoted $O^{(2)}$, see Fig. 2.2), aligned in the [111] direction inside the dislocation glide plane to avoid cross-slip. Due to the periodic boundary conditions in the [111] direction, the carbon atoms form an infinite one-dimensional array with a spacing between carbon atoms defined by two lengths: $\ell$ and $L$, with $\ell \leq L$ as illustrated in Fig. 4.7 (a).

Fig. 4.7 details the full unpinning processes of a dislocation, with the corresponding stress-strain curve, simulated with $\ell = 10\,b$, $L = 30\,b$ at 40 K. A step-by-step visualisation of the MD simulation can be decomposed in 6 successive images shown in Fig. 4.7 (a). The dislocation is initially in the Peierls valley before the C atoms (step 1). It transits to the valley just after the C atoms (step 2) at a relatively low stress of about 250 MPa, which is marked by a slight stress drop highlighted by a dashed circle in Fig. 4.7 (b). The magnitude of the stress drop is $\Delta\tau = \mu\rho bd$ ($d$ is the distance Peierls valleys) and correspond to the plastic work associated with the first jump. This configuration is the true pinning configuration, which resists dislocation motion until a high applied stress of about 950 MPa. At this point, a kink

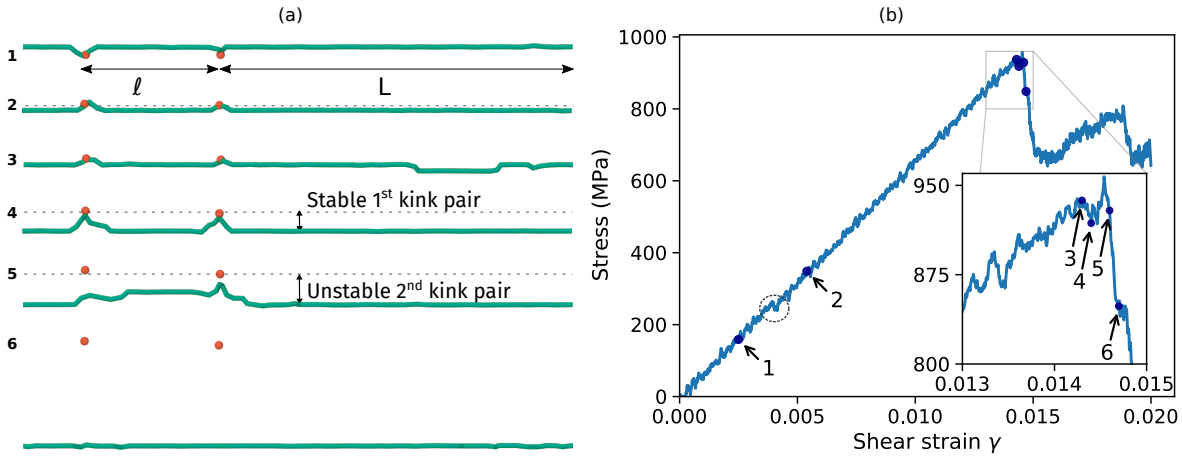


Figure 4.7: **Unpinning process for a dislocation pinned by two carbon atoms.** (a) Snapshots taken at typical stages. The dislocation line is in green, carbon atoms are red spheres. Dashed lines serve as a visual guide. (b) Corresponding stress-strain curve. Numbers in (b) refer to the images in (a). Carbon atoms are separated by $\ell = 10b$ along a $40b$-dislocation. The MD simulation was conducted at 40 K to reduce thermal fluctuation, for 2 ns with a strain rate of $1 \times 10^7$ s$^{-1}$.

pair forms on the longer $L$ segment (step 3). The kink height is one Peierls valley, although it appears on Fig 4.7 (a) as a half kink due to an artefact of the DXA algorithm. Between steps 3 and 4, double kinks have nucleated on both the short $\ell$ and long $L$ segments and expanded along the entire available segment length. They have however stopped at the C atoms that acted as strong obstacles blocking their annihilation[2]. Step 4 is followed by a short period of stress increase, which suggests that this atomic configuration is stable under the applied stress, i.e. the two kinks on both sides of the C atoms cannot annihilate, at least on short timescales. Between steps 4 and 5, a second double kink nucleates on the longer segment, which causes unpinning followed by a large stress drop on the stress-strain curve in Fig. 4.7 (b).

C atoms are therefore strong enough obstacles to block the annihilation of kinks despite the strong attractive kink-kink elastic interactions. The nucleation of a second kink pair is needed, which creates a kink with a height of two Peierls valleys. This extended kink is able to cross the C atom (left C atom in step 5 of Fig. 4.7 (a)), leading to the unpinning of the entire dislocation. Moreover, nucleation of kink-pairs is a thermally-activated process, such that

[2]This effect is observed even though the annihilation of two opposite kinks would lead to a large energy gain, which can be estimated from the drop of enthalpy in the last stage of the Peierls barrier under stress (for 0.6 GPa the Fig. 3.3 (a)), and which is likely higher than the energy of the carbon in the dislocation. This result suggests that there is a high energy barrier for the kinks to cross the carbon, which is larger than the barrier of nucleation on top of the nucleated kink pair.

the unpinning stress $\tau^*$ is a random variable affected by the random seed used to assign the initial atomic velocities. This effect is illustrated in Fig. 4.8. To account for this, we performed $n$ repetitions for each MD simulation with different random seeds ($n$ ranging from 5 to 20), and we compute the average unpinning stress $\tau^*$ and its uncertainty $\sigma/\sqrt{n}$, where $\sigma$ is the standard deviation of a series of $n$ independent measurements of $\tau^*$.

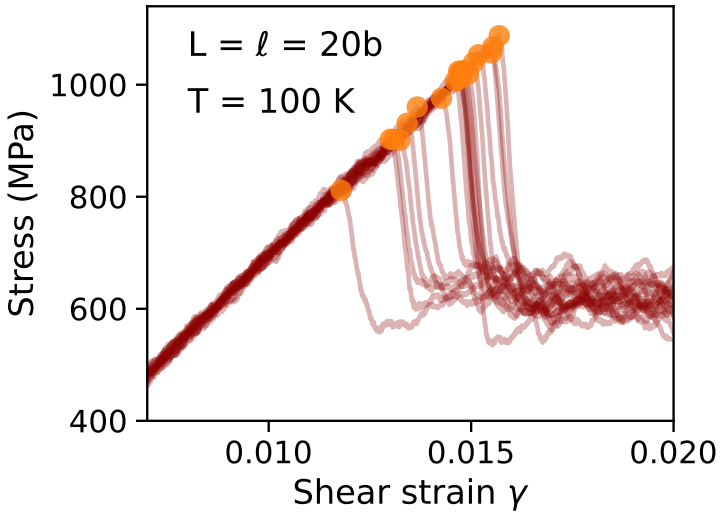


Figure 4.8: **Effect of the random initial velocity on the unpinning stress.** Stress-strain curves obtained with one C atom with $L = 40$b, and with two C atoms $\ell = L = 20$b at 100 K. 20 different random seeds are used for the initial atomic velocities. The unpinning stress $\tau^*$ is marked by orange circles.

### 4.3.1 Effect of solutes spacing

We investigated the effect of solute spacing by varying $\ell$ and $L$ on dislocations of varying $\ell+L$ lengths. However, we have seen that the length of the shorter $\ell$ segment has a negligible effect, such that all results can be presented in Fig. 4.9 as a function of $L$ only. The figure also contains the flow stress computed in pure iron, which does not show any significant dependence on the dislocation length $L$. This is coherent with the fact that without obstacles, the flow stress depends only logarithmically on $L$. The reason is that the flow stress is solution of Orowan equation $\dot{\gamma} = \rho b v$, with $\rho$ the density of mobile dislocations (here $\rho = 1/L_y L z$) and $v$, the dislocation velocity. As introduced in Sec. 3.2.2, the velocity $v$ of a dislocation of length $L$ can be expressed by a thermally activated forward-jump model:

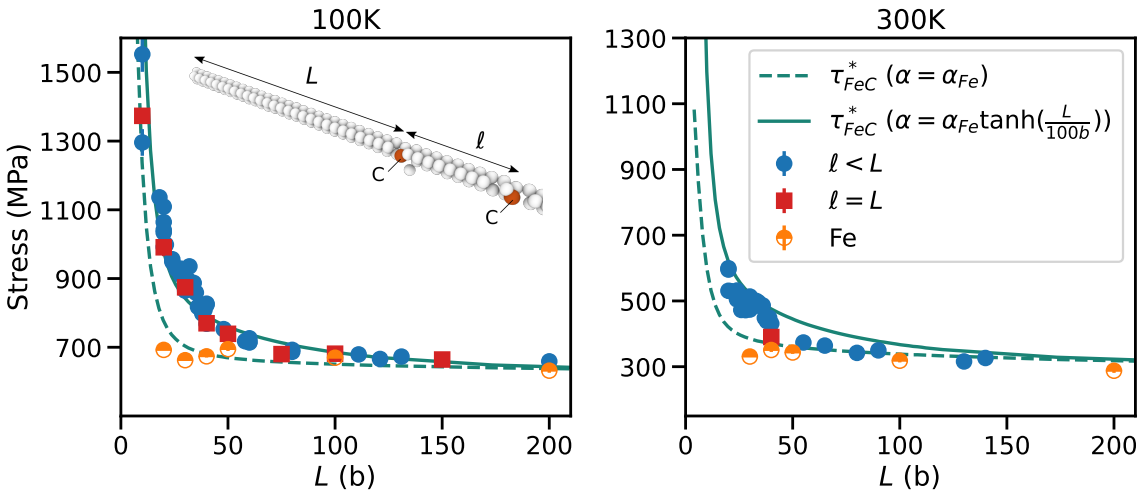


Figure 4.9: **Dependence of the average unpinning stress on the largest dislocation segment length** $L$. MD at (a) 100 K and (b) 300 K. Blue circles are when $\ell < L$, red squares when $\ell = L$. Half-filled orange symbols refer to the flow stress in pure iron computed by MD in cells of different lengths $L$. The dashed and solid lines are predictions of a statistical model (see text for details).

$$v = vL \exp\Big(-\frac{\Delta G_{kp}(\tau^*, t)}{k_B T}\Big) \tag{4.1}$$

where $v$ is an attempt frequency and $\Delta G_{kp}$ is the Gibbs activation energy. The flow stress $\tau^*$ is thus solution of

$$\Delta G_{kp}(\tau^*, t) = k_B T \log\Big(\frac{v\rho bL}{\dot{\gamma}}\Big), \tag{4.2}$$

which depends only logarithmically on $L$. When used with correct values of $\Delta G_{kp}$, this simple model showed very good agreement with MD data in Chap. 3. One caveat of this model is its low-stress limit, which does not prevent the flow stress from going to zero as neither reverse jump or kink migration is taken into account. However, this issue is irrelevant in the high-stress, low-temperature domain considered in the following, where this model yields good results.

By way of contrast, the average unpinning stress in presence of C atoms shows a very strong $L$-dependence when $L$ 100 $b$. $\tau^*$ reaches more than 1 GPa when solutes are closest, meaning that the stress required to overcome them is more than twice the flow stress and is actually even higher than the 0 K Peierls stress in pure Fe (~ 1 GPa). This demonstrates the powerful locking capability of an array of C atoms, with a spacing in the range 5 to ~ 50 $b$ when the temperature is small enough that the solute atoms cannot follow the dislocation

in its glide. This very strong pinning for closely spaced C atoms is consistent with DFT calculations (Lüthi et al., 2018). For larger C spacings, the unpinning stress reduces to the flow stress in pure iron and no strengthening or weakening is observed when $L \gtrsim 100\ b$.

In addition, as mentioned above, the data show only a small difference in $\tau^*$ whether the dislocation is pinned by evenly ($\ell = L$, red squares) or unevenly spaced C atoms ($\ell \leq L$, blue circles). The latter case was investigated by repeated simulations with different values of $\ell$, ranging between 0 and $L$, which is why different data points share the same $L$ in Fig. 4.9. The reason for a negligible influence of the $\ell$ segment is that unpinning is controlled by the nucleation of the second kink pair (step 5 of Fig. 4.7), which has a higher probability to occur on the longer $L$ segment.

### 4.3.2 Effect of C atoms on kink pair nucleation enthalpy

#### NEB calculations

In order to better understand the origin of the very strong pinning induced by the C atoms at short distance, we used the NEB method to identify the minimum energy paths that connect the different stages of unpinning identified in MD simulations (i.e stages presented in Fig. 4.7 (a)), followed with an ART convergence to identify precisely the saddle configurations. We consider here the case $L = \ell$ where only one C atom needs to be inserted in the simulation cell. The reference state for the NEB calculations, $S_0$, is constructed in the same way as in the dynamic simulations, by inserting a C atom in an $O^{(2)}$ site, and relaxing the system. Final states are constructed by introducing the dislocation in different Peierls valleys in the glide direction. The initial NEB path was obtained by linear interpolation between the initial and final state.

Equilibrium and activated states for a dislocation with $L = 30\ b$ at an applied stress of 600 MPa are shown in Fig. 4.10 (a), with the corresponding energy barriers in Fig. 4.10 (b). Note that the enthalpy globally decreases due to the work of the applied stress, which tilts the potential energy landscape.

The unpinning process involves the successive nucleation of two kink-pairs, between $S_1$ and $S_2$ and between $S_2$ and $S_3$. As can be seen in Fig. 4.10 (a), the kink-pairs in the activated states ($S_1^\star$ and $S_2^\star$) have not formed at the C atom, but rather in-between the C atom and one of its periodic images. The configuration $S_2$ contains two kinks on either side of the C atom. It is metastable. This confirms the MD observation that kinks of opposite signs cannot spontaneously annihilate when there is a C atom in-between them. The enthalpy barrier to form this first kink pair is noted $\Delta H_1$. A second barrier of height $\Delta H_2$ has to be overcome

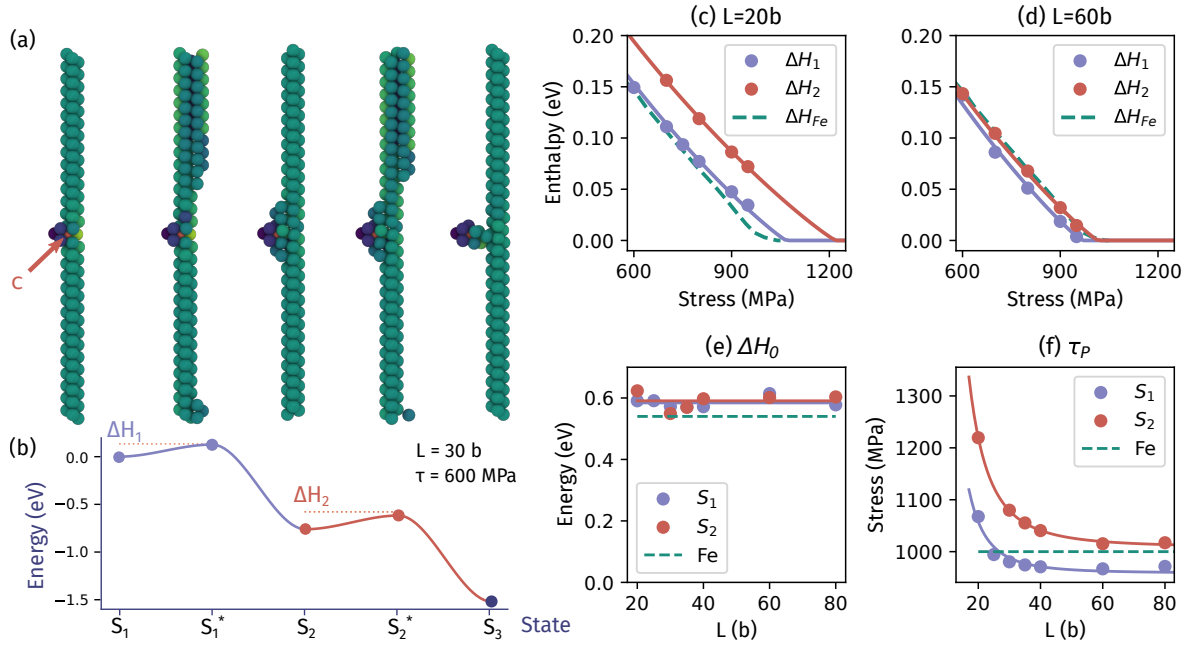


Figure 4.10: **NEB calculations of the two-step unpinning process of a dislocation from a row of C atoms.** (a) Successive metastable and activated states during the interaction process. Atoms of the core are identified using the centrosymmetry parameter (Kelchner et al., 1998). (b) Sketch of the corresponding energy profile. (c) and (d) show the activation enthalpies of both transitions (circles) for two different solute separations. The solid lines are fits using Kocks' law (Eq. 4.9). (e) and (f) show the fitted parameters $\Delta H_{0,i}$ and $\tau_{P,i}$ of Kocks' law. Solid lines in (e) and (f) represent the average of $\Delta H_0$ and a fit of $\tau_P$ using Eq. 4.10 for both transitions. Dashed lines in (c) to (f) represent the corresponding quantities in pure iron.

to form a second kink pair (state $S_2^\star$) and release the dislocation. This also confirms the MD observation that a kink crossing two Peierls valleys can overcome a C atom and unpin the dislocation. The next valleys (not shown here) are crossed with activation barriers close to that in pure Fe, $\Delta H_{\mathrm{Fe}}$.

Fig. 4.10 (c,d) show examples of activation barriers for dislocation lengths $L = 20$ and 40 $b$ as well as in pure Fe. When $L$ is small (20 $b$), we observe a significant increase of $\Delta H_2$ compared to $\Delta H_1$, which on the other hand remains close to $\Delta H_{\mathrm{Fe}}$. Therefore, the C atom does not affect significantly the nucleation of the first kink-pair, but the presence of this kink pair which cannot annihilate because of the C atom makes nucleation of the second kink pair much harder. This increase is at the origin of the strengthening seen in the MD simulation. Conversely, larger values of $L$ (60 $b$) yield almost no change compared to pure iron. When the C atoms are widely separated, the kink-pairs, which form away from the C atoms, no longer feel the presence of the solute atoms. We note a slight decrease of $\Delta H_1$, implying that the C atoms help somewhat the nucleation of the first kink-pair. But since $\Delta H_2$, which controls the unpinning, matches $\Delta H_{\mathrm{Fe}}$, no softening is produced, as confirmed by the MD simulations. This is different from substitutional solid solutions, where solutes can help the nucleation of kink-pairs and induce a softening effect (Ghafarollahi et al., 2019).

### Statistical model

In order to connect the energy barriers with the MD simulations, we used a statistical model based on the TST to predict the average unpinning stress. This model is adapted from Ref. (Rodney, 2007), which considered thermally-activated glide in absence of obstacles.

The central quantity of the statistical model is the survival probability, $W(t, t')$, the probability that the system in a metastable state at time $t$ remains in that state until $t'$.

$$W_i(t, t') = \exp\left(-\int_t^{t'} p_i(\dot{\tau}_0 u)\, du\right) \tag{4.3}$$

In the present case, we need to consider two survival probabilities: $W_1$ in $S_1$ and $W_2$ in $S_2$. The probability that, starting at $t = 0$ in an unstrained system, the dislocation is still pinned at time $t$ is expressed as:

$$W(t) = W_1(0, t) - \int_0^t \frac{\partial W_1}{\partial t'}(0, t^\star) W_2(t^\star, t) dt^\star, \tag{4.4}$$

where the first term is the probability that the dislocation is still in state $S_1$ at time $t$ and the

second term is the probability that the dislocation jumps from $S_1$ to $S_2$ at time $t^\star \in [0,t]$ but then remains in $S_2$ until $t$. The survival probabilities depend on the transition rate, i.e. the probabilities per unit time, $p_{i=1,2}(\tau, L, T)$, that the dislocation jumps from $S_1$ to $S_2$ ($i = 1$) and from $S_2$ to $S_3$ ($i = 2$). These rates are functions of the dislocation length $L$ and the temperature $T$ as well as the internal stress $\tau$. Since the MD simulations are stain-rate controlled, the stress increases linearly with time, at a rate $\dot{\tau}_0 = \mu\dot{\gamma}$, where $\mu$ is the shear modulus. The survival probability is then expressed as:

$$\begin{aligned} W(t) = &\exp\Big(-\int_0^t p_1(\dot{\tau}_0 u)\,du\Big) \\ &+ \int_0^t \Big[p_1(\dot{\tau}_0 t^*)\exp\Big(-\int_0^{t^*} p_1(\dot{\tau}_0 u)\,du\Big)\exp\Big(-\int_{t^*}^t p_2(\dot{\tau}_0 u - \Delta\tau)\,du\Big)\Big]\,dt^*. \end{aligned} \tag{4.5}$$

The probability to unpin at time $t$ is given by $\omega(t) = -dW/dt$ and the average unpinning stress is thus:

$$\langle \tau^\star \rangle = \mu\dot{\gamma}\int_0^\infty t\omega(t)dt \tag{4.6}$$

To compute $\langle \tau^\star \rangle$, we thus need to express the rates, $p_{i=1,2}(\tau, L, T)$. Within the TST, they are written as:

$$p_i(\tau, L, T) = \nu L \exp\Big(\frac{-\Delta G_i(\tau, L, T)}{kT}\Big) \tag{4.7}$$

where $\nu$ is the attempt frequency and $\Delta G_i$ is the Gibbs activation energy of the process.

As extensively discussed in Chap. 3, $\Delta G$ is notoriously difficult to compute and approximations are often used. While we were able to directly compute $\Delta G$ in the case of a dislocation gliding in pure iron, the present case is more complex and the use of the PAFI method remains challenging. In our tests, difficulties arise from the competition between carbon migration and kink pair formation, which both can happend during the constrained MD sampling done by PAFI. Technical concerns on how to inhibit carbon migration while not affecting crystal vibration modes remain difficult to address.

We therefore use approximations to compute $\Delta G_i$, based on the results obtained in pure Fe (see Chap. 3). We consider that $\Delta H$ and $\Delta S$ do not depend on $T$ and $\Delta H(\tau, L)$ is directly obtained from the zero Kelvin MEP computed in previous section. At low temperature, we derived a stress/entropy linear relation from our Gibbs energy calculations in Fe:

$$\Delta S \simeq k_B \alpha_{Fe} \tau \tag{4.8}$$

with $\alpha_{Fe} = 1.6 \times 10^{-2}\,\mathrm{MPa}^{-1}$, which compared well with MD simulations. Here, we also use

the attempt frequency $\nu = 5 \times 10^{10}\,\mathrm{s}^{-1}$ already used in Chap. 3.

Computing Eq. 4.7 requires a continuous expression of $\Delta H_i(\tau, L)$. For this purpose, we used again a classical Kocks law (Kocks et al., 1975):

$$\Delta H_i(\tau, L) = \Delta H_{0,i}(L)\left(1 - \left(\frac{\tau}{\tau_{P,i}(L)}\right)^p\right)^q \tag{4.9}$$

We found here sufficient to set the exponents $p = 0.6$ and $q = 1.1$ to the values obtained by fitting the kink pair formation enthalpy in iron with Proville potential and to only adjust $\Delta H_0$ and $\tau_P$. The fits are shown as continuous lines in Fig. 4.10 (c, d) while the values of $\Delta H_{0,i}(L)$ and $\tau_{P,i}(L)$ are reported in Fig. 4.10 (e, f). They represent the effect of the solute spacing on the activation enthalpy. We found $\Delta H_{0,1} \approx \Delta H_{0,2}$, independent of $L$ and only slightly larger than the value in pure iron (see Fig. 4.10 (e)). For the sake of simplicity, we used their average value, $\Delta H_{0,i}$, in the model. The effective Peierls stresses $\tau_{P,i}$ on the other hand strongly depends on the solute spacing and are different for the first and second barrier. As seen in Fig. 4.10(f), they can be accurately fitted as:

$$\tau_{P,i}(L) = \frac{a_i}{(L/b)^{b_i}} + c_i \tag{4.10}$$

with $a_1 = 7.89 \times 10^5$ MPa, $b_1 = 3.0$, $c_1 = 959$ MPa, $a_2 = 7.10 \times 10^5$ MPa, $b_2 = 2.7$, $c_2 = 1.01 \times 10^3$ MPa. The strong dependence of $\Delta H_2$ on L seen in Fig.4.10 (c) and (d) implies that short segments have a much reduced nucleation probability compared to larger segments, resulting in the negligible effect of $\ell$ observed in Sec. 4.3.1.

The unpinning stresses obtained from Eq. 4.5 with the continuous approximation of $\Delta H_i$ in Eq. 4.9 and the attempt frequency and activation entropy computed in pure iron are shown as a dashed line in Fig. 4.9. The model reproduces the strong pinning effect at short solute spacing, which is caused by the increased activation enthalpy, and the convergence to the flow stress in pure iron at large spacing. In-between, the model tends to underestimate the pinning stress.

Length-dependent entropy We have made a strong simplification by assuming that the activation entropy $\Delta S$ was not affected by the solute atoms. We can reasonably expect that the presence of solute atoms along the dislocation will affect the vibrational modes of the system and thus modify the activation entropy. We attempted to perform free energy barrier calculations with the PAFI method in the case of Fe-C, but faced difficulties as carbon tends to migrate to neighbouring sites during the sampling at finite temperature. In the limit of

short segments (*i.e.* a few Burgers vectors), the available length is small enough for the line to advances while remaining straight instead of forming a double kink. For this process, a much reduced activation entropy is expected compared to the kink pair mechanism, as (i) both the initial and activated states have a unique position due to the invariance in [111] direction, leading to a null configuational entropy and (ii) the vibration modes of two straight segments are likely to be less different than those of a straight line and a kink pair. For longer segments on the other hand, the behaviour of pure iron is recovered, and $\Delta S \sim \alpha_{Fe} k_B \tau$ at low temperature, which is independent of L. In order to assess the possible effect of an activation entropy which increases with $L$ and smoothly tends to the value of pure iron, we tested a simple phenomenological law $\alpha(L) = \alpha_{Fe} \tanh\left(\frac{L}{100b}\right)$ for both barriers.

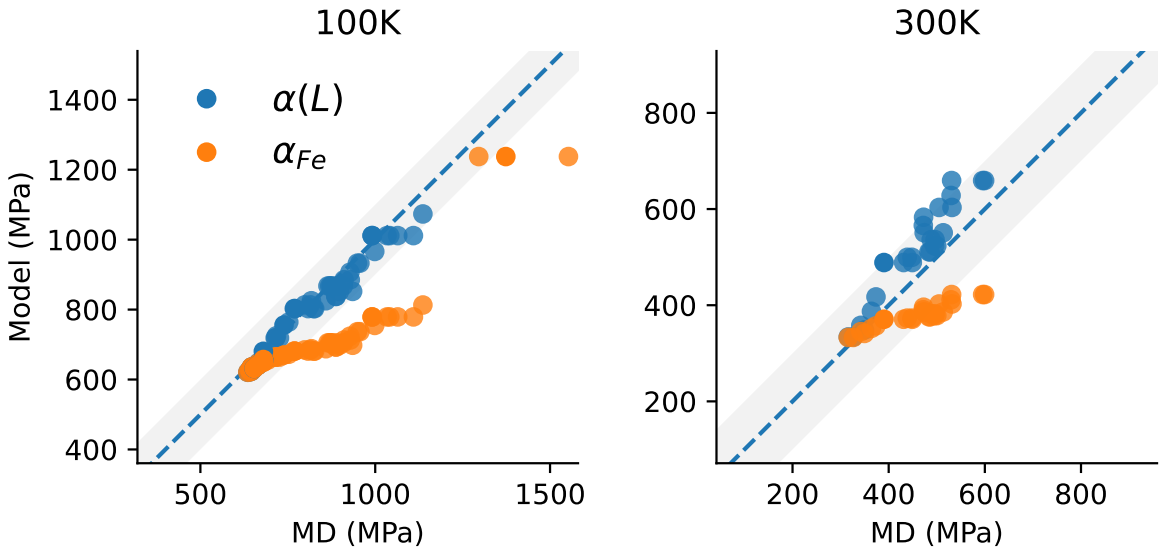


Figure 4.11: **Unpinning stress obtained in MD and predicted by the models.** The prediction of the model is compared with MD unpinning stress values at 100 K (left) and 300 K (right). Two hypothesis are tested for $\alpha$: the value previously determined in iron $\alpha_{Fe}$, and the phenomenological length-dependent law $\alpha(L)$.

This is again a simplification since we can expect the activation entropy to vary differently for both barriers. However, we can see in Fig. 4.9 where the prediction of the model with the length-dependent activation entropy is shown as a continuous line, that the simple phenomenological law greatly improves the agreement between the statistical model and the MD simulations. Fig. 4.11 allows to compare the prediction of the two models plotted on the same scale. This suggests that the activation entropy is reduced for closely-spaced defects, which is left to investigate in future work.

## 4.4 Conclusions

We used atomistic simulations to study the interaction of screw dislocations with interstitial carbon atoms in iron. Simulations of full solid solutions showed a strong locking caused by the short-range attraction between the dislocation and the solutes. The contributions of all carbon atoms close to the dislocation line result in a collective effect that amplifies the strengthening.

In order to clarify the origin of this strengthening and to overpass the difficulty to analyse such collective effect in MD simulation, we focus on elementary interaction processes between a screw dislocation and an array of carbon atoms. Based on enthalpy calculations, we built a statistical model which is able to reproduce MD results with good agreement. Though generally neglected, the effect of entropy discussed in Chap. 3 was again significant in the case of the Fe-C system. To take it into account, we incorporated a stress- and length-dependent harmonic activation entropy law using a phenomenological approach, to avoid explicitly computing the harmonic entropy. Indeed, diagonalizing the Hessian matrix for the many possible configurations would result in a high computational cost, and instabilities around the MEP already mentioned could flaw the results. A more detailed study, based on free energy calculations in the FeC system for different solute spacings and levels of stress, would be very valuable and is an important perspective of this work.

# Conclusion and perspectives

The addition of carbon in steels to improve mechanical properties make these alloys prone to ageing, which can be detrimental over long timescales, especially in the case of nuclear pressurized water reactors where it could limit the operation lifetime. Steel ageing is caused by the locking of dislocations by carbon solutes, which strongly impedes plastic deformation. In this work, we investigated atomic-scale mechanisms that enable the mobility of dislocations in iron and carbon steels, in order to develop a mobility law of dislocations in aged steels, transferable to larger-scale models.

Chapter 2: Assessment of interatomic potentials A first barrier for atomistic simulations of dislocations in the Fe-C system is the accuracy of available interatomic potentials. In Chap. 2, we tested all Fe-C empirical potentials available from the reference NIST database (Becker et al., 2013; Hale et al., 2018) on screw dislocations and alloy properties, with a special focus on the Peierls mechanism, the carbon-induced screw dislocation core reconstruction, and the carbon-dislocation binding energy. Our calculations show that all tested potentials fail to reproduce some or all of these properties accurately compared to reference *ab initio* data. We therefore implemented a simple combination of two EAM potentials for Fe and FeC with complementary properties, the Fe potential from Proville et al. (2012) and the Fe-C from Becquart et al. (2007) modified in Veiga et al. (2014), in a way that Fe-Fe interactions are unchanged compared to the potential of Proville et al. (2012). The resulting hybrid potential shows a satisfactory agreement with *ab initio* data, with the limited computational footprint of an EAM potential —while avoiding the heavy task of fitting a new interatomic potential from an *ab initio* dataset. This hybrid potential opens the way for atomistic simulations of carbon-dislocation interaction mechanisms, such as solute strenghthening.

However, one caveat of the hybrid potential is the roughness of its energy landscape along the carbon migration path between octahedral positions, which makes this potential unsuited for simulations involving diffusion mechanisms, where the potential of Becquart et al. (2007) remains preferred. At the time of writing, it appears that there is still no available poten-

tial suited for both screw dislocation glide and carbon diffusion simulations. The increasing use of machine learning methods for interatomic potentials development will likely help develop new potentials with better accuracy and transferability, thus overcoming the limitations discussed here, perhaps with a computational cost several orders of magnitude larger than classical EAM (see *e.g.* Mishin (2021) for a review).

Potentials testing remains a crucial methodological step, which is often overlooked and cannot be comprehensive, due to the heavy task of setting up calculations of many different properties, and multiple methods can often be used to determine the same property, possibly leading to different results. Projects such as the iprPy tool (Hale et al., 2018) or OpenKIM database (Elliott and Tadmor, 2011) address this issue by automating potential properties calculations, making useful results freely available, but they still lack many important material properties, and need to be extended by contributions from the community.

Chapter 3: dislocation glide in Fe In pure bcc iron, plastic deformation is controlled by the mobility of dislocations, which is limited by the lattice resistance at low temperature. In Chap. 3, we computed the flow stress of iron using shear-rate controlled MD simulations of isolated screw dislocations based on the potential of Proville et al. (2012). We tested several classical dislocation glide models based on the harmonic transition state theory as well as often-used assumptions for the calculation of the Gibbs energy of activation for kink pair nucleation (constant entropy, Meyer-Neldel law), which fail to reproduce our MD data in the entire range of temperature.

The recent *projected average force integrator* (PAFI) method enables direct Gibbs activation energy $\Delta G$ calculations for thermally-activated processes in large systems, with no assumption on the nature of atomic vibrations, *i.e.* unlocking the usual limitations of entropy calculations based on harmonic TST, which scale cubically with the number of atoms in the system, and become inaccurate at high temperature due to anharmonic effects (Swinburne, 2021). Calculations in a broad range of stresses and temperatures show a strong effect on $\Delta G$, with marked anharmonic effects. A deviation from harmonic TST calculations is observed starting at temperatures as low as 20 K, suggesting that harmonic calculations do not always provide an accurate picture of the Gibbs energy landscape in the vicinity of the initial and transition states, even at low temperature.

Since non-linearities remain small below ~100 K, the Gibbs activation energy was linearized to extract an effective activation enthalpy, which interestingly increases when the enthalpy decreases, corresponding to an inverse Meyer-Neldel behavior. Integrating the results

of PAFI simulations into kinetic models of dislocation glide, we obtained a much improved agreement with direct MD simulations compared to classical approaches. Using the inverse Meyer-Neldel law, we were are able to reproduce MD simulations up to 200-300 K. These results advocate for a better integration of entropic and anharmonic effects that are often overlooked in atomistic studies of crystal defects. In the present case, the low-temperature non-linearity could be caused by local irregularities of the Gibbs energy landscape of the potential of Proville et al. (2012), and should be verified using other atomic interaction models, such as the newly-developed machine-learning potential of Goryaeva et al. (2021).

PAFI is an efficient and versatile free-energy calculation method which can be very useful for the study of a broad range of thermally activated processes. Yet, this recent method still has to overcome some challenges to be more easily usable by the community and more efficient, especially regarding its sensitivity to the initial MEP or its parallelization scheme.

Chapter 4: dislocation glide and pinning in Fe-C In steels, dislocation mobility is limited not only by the lattice resistance but also by their interactions with interstitial carbon atoms. In Chap 4, we use the hybrid interatomic potential developed in Chap. 2 to simulate dislocations interacting with a random solid solution of carbon atoms.

Our simulations confirm a local reorganization of the dislocation core as previously evidenced in *ab initio* simulations, and a strong dislocation pinning caused by complex short-ranged carbon-dislocation interactions. In order to investigate the elementary pinning mechanisms, we studied the idealized case of a dislocation interacting with a row of carbon atoms, using a combination of MD simulations, saddle-point search techniques, and a harmonic TST kinetic model based on the calculations presented in Chap. 3. Our results indicate that carbon stabilizes the first kink pair by preventing kink annihilation, likely due to the local reconstruction of the dislocation core. As a result, a second kink pair has to form for the dislocation to unpin, with a markedly increased activation enthalpy. This effect causes a high strenghtening effect, with an unpinning stress that can be more than twice the flow stress of pure iron for closely-spaced solutes.

A more comprehensive investigation of entropic effects would be necessary, as these are affected by the presence of solutes, but remains challenging. Preliminary tests with the PAFI method revealed that under finite temperature and applied stress, carbon atoms tend to jump to other sites during the sampling. We presented a simple phenomenological approach to illustrate how a segment length-dependent activation entropy could improve the agreement with MD simulations, but Gibbs energy calculations in this system remain challenging,

and might require adaptations in the PAFI code. Yet, investigating anharmonicity in alloys would have a great interest for studies above room temperature *e.g.* on serrated flow (Zhao et al., 2020), where we expect anharmonic effects to be dominant. The present work remains limited by the accuracy of the interatomic potential we used, and further investigation, especially concerning entropic effects, is difficult without a more accurate potential for Fe-C. We have shown here that the elementary interaction process between a screw dislocation and carbon atoms involves the successive nucleation of two kink pairs, since a carbon atom is able to block a single kink and prevent its annihilation with a kink on the other side at least on MD timescale.

Our results in Fe and Fe-C could be combined and implemented in mesoscale models, which constitutes the next step towards a constitutive law of aged steel. In Fig. 1, the flowchart for multiscale simulation of plasticity proposed by Tipping (2010) is adapted to highlight the contribution of the present work, as well as connections to larger scale models. In particular, integrating both the effect of the lattice resistance at high temperature and the effect of interstitial solute (which could be treated using local rules) in kinetic Monte Carlo models of dislocation pinning as developed in Zhao and Marian (2018); Zhao et al. (2020); Shinzato et al. (2019) is the main perspective of this work to better understand the effect of carbon solutes. Such a model would allow the study of the complex and collective interplay between solute-dislocation interactions and stress-mediated solute diffusion leading to the formation of Cottrell atmospheres, over length- and time-scales unaccessible to MD simulations, more accurately than approaches fully based on harmonic theories.

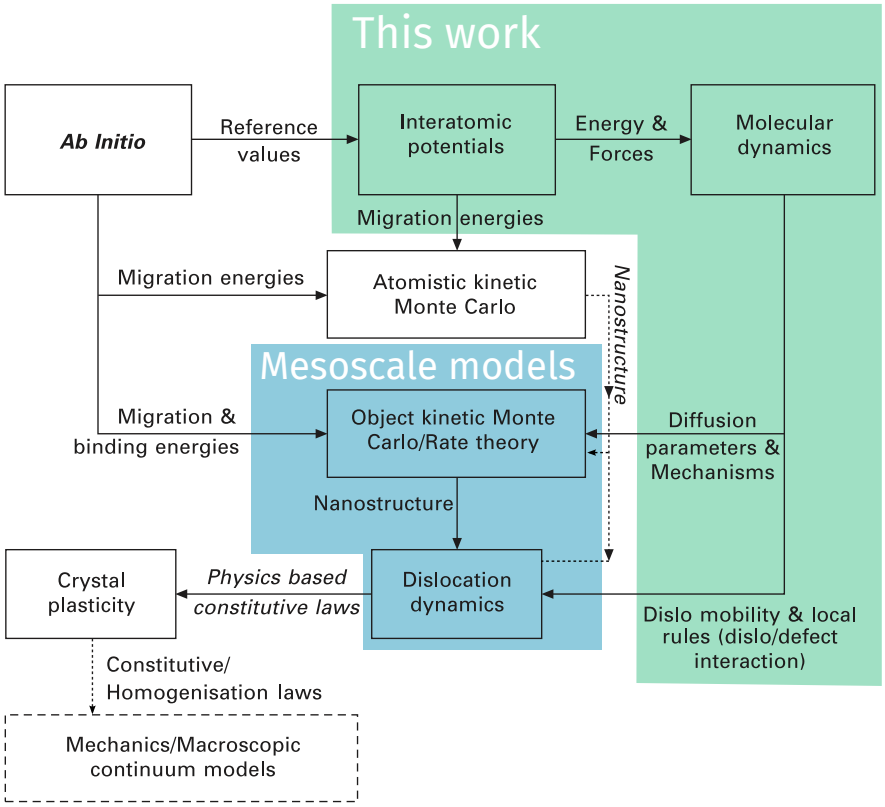


Figure 1: **Flowchart of multiscale modelling of plasticity** adapted from Tipping (2010). The contribution of the present work is emphasized (in green), as well as its main perspectives (in blue).

# Bibliography


Abraham, F. F., Broughton, J. Q., Bernstein, N., and Kaxiras, E. (1998). Spanning the continuum to quantum length scales in a dynamic simulation of brittle fracture. *Europhysics Letters*, 44(6):783–787.

Ackland, G. J. (2002). Calculation of free energies from ab initio calculation. *Journal of Physics Condensed Matter*, 14(11):2975–3000.

Ackland, G. J. and Bonny, G. (2020). Interatomic Potential Development. In *Comprehensive Nuclear Materials*, pages 544–572. Elsevier.

Ackland, G. J., Mendelev, M. I., Srolovitz, D. J., Han, S., and Barashev, A. V. (2004). Development of an interatomic potential for phosphorus impurities in $\alpha$ iron. *Journal of Physics: Condensed Matter*, 16(27):S2629.

Alexander, R., Proville, L., Becquart, C. S., Goryeava, A. M., Dérès, J., Lapointe, C., and Marinica, M.-C. (2020). Interatomic potentials for irradiation-induced defects in iron. *Journal of Nuclear Materials*, 535:152141.

Amodeo, J., Maras, E., and Rodney, D. (2021). Site dependence of surface dislocation nucleation in ceramic nanoparticles. *npj Computational Materials*, 7(60).

Ásgeirsson, V. and Jónsson, H. (2020). Exploring Potential Energy Surfaces with Saddle Point Searches. In *Handbook of Materials Modeling*, pages 689–714. Springer, Cham.

Bacon, D., Osetsky, Y., and Rodney, D. (2009). Chapter 88 Dislocation–Obstacle Interactions at the Atomic Level. In *Dislocations in Solids*, volume 15, pages 1–90.

Ballesteros, A., Ahlstrand, R., Bruynooghe, C., Von Estorff, U., and Debarberis, L. (2012). The role of pressure vessel embrittlement in the long term operation of nuclear power plants. *Nuclear Engineering and Design*, 243:63–68.

Barkema, G. T. and Mousseau, N. (1996). Event-based relaxation of continuous disordered systems. *Physical Review Letters*, 77(21):4358.

Barvinschi, B., Proville, L., and Rodney, D. (2014). Quantum Peierls stress of straight and kinked dislocations and effect of non-glide stresses. *Modelling and Simulation in Materials Science and Engineering*, 22(2):25006.

Baskes, M. I. (1992). Modified embedded-atom potentials for cubic materials and impurities. *Physical Review B*, 46(5):2727–2742.

Becker, C. A., Tavazza, F., Trautt, Z. T., and Buarque De Macedo, R. A. (2013). Considerations for choosing and using force fields and interatomic potentials in materials science and engineering. *Current Opinion in Solid State and Materials Science*, 17(6):277–283.

Becquart, C. S., De Backer, A., Olsson, P., and Domain, C. (2021). Modelling the primary damage in Fe and W: Influence of the short range interactions on the cascade properties: Part 1 – Energy transfer. *Journal of Nuclear Materials*, 547:152816.

Becquart, C. S., Raulot, J., Bencteux, G., Domain, C., Perez, M., Garruchet, S., and Nguyen, H. (2007). Atomistic modeling of an Fe system with a small concentration of C. *Computational Materials Science*, 40:119–129.

Berns, H. and Theisen, W. (2008). *Ferrous Materials*. Springer Berlin Heidelberg, Berlin, Heidelberg.

Bertin, N., Sills, R. B., and Cai, W. (2020). Frontiers in the Simulation of Dislocations. *Annual Review of Materials Research*, 50(1):1–28.

Bigger, J. R., McInnes, D. A., Sutton, A. P., Payne, M. C., Stich, I., King-Smith, R. D., Bird, D. M., and Clarke, L. J. (1992). Atomic and electronic structures of the 90°partial dislocation in silicon. *Physical Review Letters*, 69(15):2224–2227.

Blavette, D., Cadel, E., Fraczkiewicz, A., and Menand, A. (1999). Three-dimensional atomic-scale imaging of impurity segregation to line defects. *Science*, 286(5448):2317–2319.

Brown, W. M., Wang, P., Plimpton, S. J., and Tharrington, A. N. (2011). Implementing molecular dynamics on hybrid high performance computers–short range forces. *Computer Physics Communications*, 182(4):898–911.

Brunner, D. and Diehl, J. (1991). Temperature and Strain-Rate Dependence of the Tensile Flow Stress of High-Purity $\alpha$-Iron below 250 K. I. Stress/Temperature Regime III. *Physica Status Solidi (a)*, 124(2):455–464.

Bulatov, V. and Cai, W. (2006). *Computer Simulations of Dislocations*, volume 3. Oxford University Press.

Bulatov, V. V. and Cai, W. (2002). Nodal Effects in Dislocation Mobility. *Physical Review Letters*, 89(11):115501.

Caillard, D. (2011). An in situ study of hardening and softening of iron by carbon interstitials. *Acta Materialia*, 59(12):4974–4989.

Caillard, D. and Martin, J.-L. (2003). *Thermally Activated Mechanisms in Crystal Plasticity*, volume 8. Elsevier.

Candela, R., Gelin, S., Mousseau, N., Veiga, R. G. A., Domain, C., Perez, M., and Becquart, C. S. (2020). Investigating the kinetics of the formation of a C Cottrell atmosphere around a screw dislocation in bcc iron: a mixed-lattice atomistic kinetic Monte-Carlo analysis. *Journal of Physics: Condensed Matter*, 33(6):65704.

CEA-DEN (2014). *Les matériaux du nucléaire. Modélisation et simulation des matériaux de structure.* CEA Saclay, Éditions Le Moniteur.

Cereceda, D., Diehl, M., Roters, F., Raabe, D., Perlado, J. M., and Marian, J. (2016). Unraveling the temperature dependence of the yield strength in single-crystal tungsten using atomistically-informed crystal plasticity calculations. *International Journal of Plasticity*, 78:242–265.

Cereceda, D., Stukowski, A., Gilbert, M. R., Queyreau, S., Ventelon, L., Marinica, M. C., Perlado, J. M., and Marian, J. (2013). Assessment of interatomic potentials for atomistic analysis of static and dynamic properties of screw dislocations in W. *Journal of Physics Condensed Matter*, 25(8).

Cheng, B. and Ceriotti, M. (2018). Computing the absolute Gibbs free energy in atomistic simulations: Applications to defects in solids. *Physical Review B*, 97(5):54102.

Christian, J. W. (1983). Some surprising features of the plastic deformation of body-centered cubic metals and alloys. *Metallurgical Transactions A*, 14(7):1237–1256.

Clouet, E. (2020). *Ab Initio Models of Dislocations*, pages 1503–1524. Springer International Publishing, Cham.

Clouet, E., Bienvenu, B., Dezerald, L., and Rodney, D. (2021). Screw dislocations in BCC transition metals: From ab initio modeling to yield criterion. *Comptes Rendus Physique*, 22(S3):1–34.

Clouet, E., Garruchet, S., Nguyen, H., Perez, M., and Becquart, C. S. (2008). Dislocation interaction with C in $\alpha$Fe: A comparison between atomic simulations and elasticity theory. *Acta Materialia*, 56(14):3450–3460.

Cottrell, A. H. and Bilby, B. A. (1949). Dislocation theory of yielding and strain ageing of iron. *Proceedings of the Physical Society. Section A*, 62(1):49–62.

De, A., De Blauwe, K., Vandeputte, S., and De Cooman, B. (2000). Effect of dislocation density on the low temperature aging behavior of an ultra low carbon bake hardening steel. *Journal of Alloys and Compounds*, 310(1-2):405–410.

de Tomas, C., Aghajamali, A., Jones, J. L., Lim, D. J., López, M. J., Suarez-Martinez, I., and Marks, N. A. (2019). Transferability in interatomic potentials for carbon. *Carbon*, 155:624–634.

Desplat, L. and Kim, J.-V. (2020). Entropy-reduced retention times in magnetic memory elements: A case of the Meyer-Neldel Compensation Rule. *Physical Review Letters*, 125(10):107201.

Dezerald, L. (2014). *Modélisation ab initio des dislocations vis dans les métaux de transition cubiques centrés*. Thesis.

Dezerald, L., Proville, L., Ventelon, L., Willaime, F., and Rodney, D. (2015). First-principles prediction of kink-pair activation enthalpy on screw dislocations in bcc transition metals: V, Nb, Ta, Mo, W, and Fe. *Physical Review B*, 91(9):094105.

Dezerald, L., Rodney, D., Clouet, E., Ventelon, L., and Willaime, F. (2016). Plastic anisotropy and dislocation trajectory in BCC metals. *Nature Communications*, 7(1):11695.

Dezerald, L., Ventelon, L., Clouet, E., Denoual, C., Rodney, D., and Willaime, F. (2014). Ab initio modeling of the two-dimensional energy landscape of screw dislocations in bcc transition metals. *Physical Review B*, 89(2):024104.

Domain, C., Becquart, C. S., and Foct, J. (2004). Ab initio study of foreign interstitial atom (C, N) interactions with intrinsic point defects in $\alpha$ -Fe. *Physical Review B*, 69(14):144112.

Domain, C. and Monnet, G. (2005). Simulation of Screw Dislocation Motion in Iron by Molecular Dynamics Simulations. *Physical Review Letters*, 95(21):215506.

E, W., Ren, W., and Vanden-Eijnden, E. (2005). Finite Temperature String Method for the Study of Rare Events. *The Journal of Physical Chemistry B*, 109(14):6688–6693.

Elliott, R. S. and Tadmor, E. B. (2011). Knowledgebase of Interatomic Models (KIM) Application Programming Interface (API). https://openkim.org/kim-api.

Esteban-Manzanares, G., Santos-Güemes, R., Papadimitriou, I., Martínez, E., and LLorca, J. (2020). Influence of the stress state on the cross-slip free energy barrier in Al: An atomistic investigation. *Acta Materialia*, 184:109–119.

Foreman, A. J. E. and Makin, M. J. (1966). Dislocation movement through random arrays of obstacles. *Philosophical magazine*, 14(131):911–924.

Gelin, S., Champagne-Ruel, A., and Mousseau, N. (2020). Enthalpy-entropy compensation of atomic diffusion originates from softening of low frequency phonons. *Nature Communications*, 11(1):3977.

Ghafarollahi, A. and Curtin, W. A. (2020). Theory of double-kink nucleation in dilute BCC alloys. *Acta Materialia*, 196:635–650.

Ghafarollahi, A., Maresca, F., and Curtin, W. A. (2019). Solute/screw dislocation interaction energy parameter for strengthening in bcc dilute to high entropy alloys. *Modelling and Simulation in Materials Science and Engineering*, 27(8):1–28.

Gilbert, M. R., Queyreau, S., and Marian, J. (2011). Stress and temperature dependence of screw dislocation mobility in $\alpha$-Fe by molecular dynamics. *Physical Review B - Condensed Matter and Materials Physics*, 84(17):1–11.

Gilbert, M. R., Schuck, P., Sadigh, B., and Marian, J. (2013). Free energy generalization of the Peierls potential in iron. *Physical Review Letters*, 111(9).

Gordon, P. A., Neeraj, T., Li, Y., and Li, J. (2010). Screw dislocation mobility in BCC metals: the role of the compact core on double-kink nucleation. *Modelling and Simulation in Materials Science and Engineering*, 18(8):085008.

Gordon, P. A., Neeraj, T., and Mendelev, M. I. (2011). Screw dislocation mobility in BCC Metals: A refined potential description for-Fe. *Philosophical Magazine*, 91(30):3931–3945.

Goryaeva, A. M., Dérès, J., Lapointe, C., Grigorev, P., Swinburne, T. D., Kermode, J. R., Ventelon, L., Baima, J., and Marinica, M.-C. (2021). Efficient and transferable machine learning potentials for the simulation of crystal defects in bcc Fe and W. *Physical Review Materials*, 5(10):103803.

Grabowski, B., Ikeda, Y., Srinivasan, P., Körmann, F., Freysoldt, C., Duff, A. I., Shapeev, A., and Neugebauer, J. (2019). Ab initio vibrational free energies including anharmonicity for multicomponent alloys. *npj Computational Materials*, 5(1):80.

Grabowski, B. and Zotov, N. (2021). Thermally-activated dislocation mobility in bcc metals: An accelerated molecular dynamics study. *Computational Materials Science*, 200:110804.

Gröger, R. and Vitek, V. (2007). Explanation of the discrepancy between the measured and atomistically calculated yield stresses in body-centred cubic metals. *Philosophical Magazine Letters*, 87(2):113–120.

Hachet, G., Caillard, D., Ventelon, L., and Clouet, E. (2022). Mobility of screw dislocation in BCC tungsten at high temperature in presence of carbon. *Acta Materialia*, 222:117440.

Hachet, G., Ventelon, L., Willaime, F., and Clouet, E. (2020). Screw dislocation-carbon interaction in BCC tungsten: an ab initio study. *Acta Materialia*, 200:481–489.

Hale, L. M., Lim, H., Zimmerman, J. A., Battaile, C. C., and Weinberger, C. R. (2015). Insights on activation enthalpy for non-Schmid slip in body-centered cubic metals. *Scripta Materialia*, 99:89–92.

Hale, L. M., Trautt, Z. T., and Becker, C. A. (2018). Evaluating variability with atomistic simulations: The effect of potential and calculation methodology on the modeling of lattice and elastic constants. *Modelling and Simulation in Materials Science and Engineering*, 26(5):1–24.

Hanlumyuang, Y., Gordon, P. A., Neeraj, T., and Chrzan, D. C. (2010). Interactions between carbon solutes and dislocations in bcc iron. *Acta Materialia*, 58(16):5481–5490.

Hara, S. and Li, J. (2010). Adaptive strain-boost hyperdynamics simulations of stress-driven atomic processes. *Physical Review B*, 82(18):184114.

Henkelman, G., Uberuaga, B. P., and Jónsson, H. (2000). A climbing image nudged elastic band method for finding saddle points and minimum energy paths. *The Journal Of Chemical Physics*, 113(22):9901–9904.

Henriksson, K. O. E. and Nordlund, K. (2009). Simulations of cementite: An analytical potential for the Fe-C system. *Physical Review B - Condensed Matter and Materials Physics*, 79(14):1–6.

Hepburn, D. J. and Ackland, G. J. (2008). Metallic-covalent interatomic potential for carbon in iron. *Physical Review B - Condensed Matter and Materials Physics*, 78(16):1–6.

Hirth, J. P. and Lothe, J. (1982). Theory of dislocations. *Wiley, New York*.

Huber, S. P., Zoupanos, S., Uhrin, M., Talirz, L., Kahle, L., Häuselmann, R., Gresch, D., Müller, T., Yakutovich, A. V., Andersen, C. W., Ramirez, F. F., Adorf, C. S., Gargiulo, F., Kumbhar, S., Passaro, E., Johnston, C., Merkys, A., Cepellotti, A., Mounet, N., Marzari, N., Kozinsky, B., and Pizzi, G. (2020). AiiDA 1.0, a scalable computational infrastructure for automated reproducible workflows and data provenance. *Scientific Data*, 7(1):1–18.

IAEA (2019). *Nuclear Power Reactors in the World*. Number 2 in Reference Data Series. International Atomic Energy Agency, Vienna.

Ishii, A., Li, J., and Ogata, S. (2013). "Conjugate Channeling" Effect in Dislocation Core Diffusion: Carbon Transport in Dislocated BCC Iron. *PLoS ONE*, 8(4).

Ismail-Beigi, S. and Arias, T. A. (2000). Ab Initio Study of Screw Dislocations in Mo and Ta: A New Picture of Plasticity in bcc Transition Metals. *Physical Review Letters*, 84(7):1499–1502.

Itakura, M., Kaburaki, H., and Yamaguchi, M. (2012). First-principles study on the mobility of screw dislocations in bcc iron. *Acta Materialia*, 60(9):3698–3710.

Kelchner, C. L., Plimpton, S. J., and Hamilton, J. C. (1998). Dislocation nucleation and defect structure during surface indentation. *Physical review B*, 58(17):11085.

Kharecha, P. A. and Hansen, J. E. (2013). Prevented mortality and greenhouse gas emissions from historical and projected nuclear power. *Environmental Science and Technology*, 47(9):4889–4895.

Khater, H. A., Monnet, G., Terentyev, D., and Serra, A. (2014). Dislocation glide in Fe-carbon solid solution: From atomistic to continuum level description. *International Journal of Plasticity*, 62:34–49.

Kochmann, D. M. and Amelang, J. S. (2016). The Quasicontinuum Method: Theory and Applications. In *Springer Series in Materials Science*, volume 245, pages 159–193.

Kocks, U., Argon, A., and Ashby, M. F. (1975). Thermodynamics and kinetics of slip. *Progress in Materials Science*, 19:1–291.

Kolsbjerg, E. L., Groves, M. N., and Hammer, B. (2016). An automated nudged elastic band method. *Journal of Chemical Physics*, 145(9):94107.

Köster, J., Mölder, F., Jablonski, K. P., Letcher, B., Hall, M. B., Tomkins-Tinch, C. H., Sochat, V., Forster, J., Lee, S., Twardziok, S. O., Kanitz, A., Wilm, A., Holtgrewe, M., Rahmann, S., and Nahnsen, S. (2021). Sustainable data analysis with Snakemake. *F1000Research*, 10:33.

Kraych, A., Clouet, E., Dezerald, L., Ventelon, L., Willaime, F., and Rodney, D. (2019). Non-glide effects and dislocation core fields in BCC metals. *npj Computational Materials*, 5(1):109.

Kubamoto, E., Aono, Y., Kitajima, K., Maeda, K., and Takeuchi, S. (1979). Thermally activated slip deformation between 0.7 and 77 K in high-purity iron single crystals. *Philosophical Magazine A*, 39(6):717–724.

Kubin, L. (2013). *Dislocations, Mesoscale Simulations and Plastic Flow, Oxford Series on Materials Modelling 5*. Taylor & Francis.

Kubin, L. P., Estrin, Y., and Perrier, C. (1992). On static strain ageing. *Acta Metallurgica Et Materialia*, 40(5):1037–1044.

Labusch, R. (1970). A Statistical Theory of Solid Solution Hardening. *Physica Status Solidi (B)*, 41(2):659–669.

Laio, A. and Gervasio, F. L. (2008). Metadynamics: a method to simulate rare events and reconstruct the free energy in biophysics, chemistry and material science. *Reports on Progress in Physics*, 71(12):126601.

LaRosa, C. R., Shih, M., Varvenne, C., and Ghazisaeidi, M. (2019). Solid solution strengthening theories of high-entropy alloys. *Materials Characterization*, 151:310–317.

Lee, B.-J. (2006). A modified embedded-atom method interatomic potential for the Fe–C system. *Acta materialia*, 54(3):701–711.

Lee, B.-J., Baskes, M., Kim, H., and Koo Cho, Y. (2001). Second nearest-neighbor modified embedded atom method potentials for bcc transition metals. *Physical Review B*, 64(18):184102.

Lee, T., Baskes, M. I., Valone, S. M., and Doll, J. D. (2012). Atomistic modeling of thermodynamic equilibrium and polymorphism of iron. *Journal of Physics Condensed Matter*, 24(22):225404.

Lenzen, M. (2008). Life cycle energy and greenhouse gas emissions of nuclear energy: A review. *Energy Conversion and Management*, 49(8):2178–2199.

Lesar, R., Najafabadi, R., and Srolovitz, D. J. (1989). Finite-temperature defect properties from free-energy minimization. *Physical Review Letters*, 63(6):624–627.

Li, J. (2018). Vacancy formation and migration energy for bcc Fe. OpenKIM, https://openkim.org/cite/TE_424131500075_000.

Liyanage, L. S. I., Kim, S.-G., Houze, J., Kim, S., Tschopp, M. A., Baskes, M. I., and Horstemeyer, M. F. (2014). Structural, elastic, and thermal properties of cementite (Fe3 C) calculated using a modified embedded atom method. *Physical Review B*, 89(9):094102.

Lu, G. and Kaxiras, E. (2004). An Overview of Multiscale Simulations of Materials.

Lüthi, B. (2017). *Modélisation ab initio des interactions entre dislocations vis et solutés interstitiels dans les métaux de transition cubiques centrés*. Thesis.

Lüthi, B., Ventelon, L., Elssser, C., Rodney, D., and Willaime, F. (2017). First principles investigation of carbon-screw dislocation interactions in body-centered cubic metals. *Modelling and Simulation in Materials Science and Engineering*, 25(8):84001.

Lüthi, B., Ventelon, L., Rodney, D., and Willaime, F. (2018). Attractive interaction between interstitial solutes and screw dislocations in bcc iron from first principles. *Computational Materials Science*, 148:21–26.

Mainsant, A. (2018). *Trajectoires d 'évolution du mix électrique 2020-2060*. ADEME Editions.

Malek, R. and Mousseau, N. (2000). Dynamics of Lennard-Jones clusters: A characterization of the activation-relaxation technique. *Physical Review E*, 62(6):7723.

Maresca, F. and Curtin, W. A. (2020). Theory of screw dislocation strengthening in random BCC alloys from dilute to "High-Entropy" alloys. *Acta Materialia*, 182:144–162.

Maresca, F., Dragoni, D., Csányi, G., Marzari, N., and Curtin, W. A. (2018). Screw dislocation structure and mobility in body centered cubic Fe predicted by a Gaussian Approximation Potential. *npj Computational Materials*, 4(1):69.

Marinica, M.-C., Ventelon, L., Gilbert, M. R., Proville, L., Dudarev, S. L., Marian, J., Bencteux, G., and Willaime, F. (2013). Interatomic potentials for modelling radiation defects and dislocations in tungsten. *Journal of Physics: Condensed Matter*, 25(39):395502.

Mello, A. W., Nicolas, A., Lebensohn, R. A., and Sangid, M. D. (2016). Effect of microstructure on strain localization in a 7050 aluminum alloy: comparison of experiments and modeling for various textures. *Materials Science and Engineering: A*, 661:187–197.

Mendelev, M. I., Han, S., Srolovitz, D. J., Ackland, G. J., Sun, D. Y., and Asta, M. (2003). Development of new interatomic potentials appropriate for crystalline and liquid iron. *Philosophical Magazine*, 83(35):3977–3994.

Meyer, R. and Entel, P. (1998). Martensite-austenite transition and phonon dispersion curves of studied by molecular-dynamics simulations. *Physical Review B - Condensed Matter and Materials Physics*, 57(9):5140–5147.

Miller, R. E. and Tadmor, E. B. (2002). The Quasicontinuum Method: Overview, applications and current directions. *Journal of Computer-Aided Materials Design*, 9(3):203–239.

Mishin, Y. (2021). Machine-learning interatomic potentials for materials science. *Acta Materialia*, 214:116980.

Mishin, Y., Mehl, M. J., and Papaconstantopoulos, D. A. (2005). Phase stability in the Fe-Ni system: Investigation by first-principles calculations and atomistic simulations. *Acta Materialia*, 53(15):4029–4041.

Mori, H. and Ozaki, T. (2020). Neural network atomic potential to investigate the dislocation dynamics in bcc iron. *Physical Review Materials*, 4(4):040601.

Mousseau, N., Béland, L. K., Brommer, P., Joly, J.-F., El-Mellouhi, F., Machado-Charry, E., Marinica, M.-C., and Pochet, P. (2012). The Activation-Relaxation Technique: ART Nouveau and Kinetic ART. *Journal of Atomic, Molecular, and Optical Physics*, 2012:1–14.

Mrovec, M., Nguyen-Manh, D., Elsässer, C., and Gumbsch, P. (2011). Magnetic bond-order potential for iron. *Physical Review Letters*, 106(24):1–4.

Müller, M., Erhart, P., and Albe, K. (2007a). Analytic bond-order potential for bcc and fcc iron - Comparison with established embedded-atom method potentials. *Journal of Physics Condensed Matter*, 19(32).

Müller, M., Erhart, P., and Albe, K. (2007b). Analytic bond-order potential for bcc and fcc iron - Comparison with established embedded-atom method potentials. *Journal of Physics Condensed Matter*, 19(32).

Nabarro, F. R. (2003). One-dimensional models of thermal activation under shear stress. *Philosophical Magazine*, 83(26):3047–3054.

Narayanan, S., McDowell, D. L., and Zhu, T. (2014). Crystal plasticity model for BCC iron atomistically informed by kinetics of correlated kinkpair nucleation on screw dislocation. *Journal of the Mechanics and Physics of Solids*, 65(1):54–68.

Okamoto, H. (1992). The C-Fe (carbon-iron) system. *Journal of Phase Equilibria*, 13(5):543–565.

Ou, X. (2017). Molecular dynamics simulations of fcc-to-bcc transformation in pure iron: a review. *Materials Science and Technology*, 33(7):822–835.

Pachauri, R. K., Allen, M. R., Barros, V. R., Broome, J., Cramer, W., Christ, R., Church, J. A., Clarke, L., Dahe, Q., and Dasgupta, P. (2014). *Climate change 2014: synthesis report. Contribution of Working Groups I, II and III to the fifth assessment report of the Intergovernmental Panel on Climate Change*. Gian-Kasper Plattner.

Patinet, S. and Proville, L. (2008). Depinning transition for a screw dislocation in a model solid solution. *Physical Review B*, 78(10):104109.

Pinna, C., Lan, Y., Kiu, M. F., Efthymiadis, P., Lopez-Pedrosa, M., and Farrugia, D. (2015). Assessment of crystal plasticity finite element simulations of the hot deformation of metals from local strain and orientation measurements. *International Journal of Plasticity*, 73:24–38.

Plimpton, S. (1995). Fast Parallel Algorithms for Short-Range Molecular Dynamics. *Journal of Computational Physics*, 117(1):1–19.

Po, G., Cui, Y., Rivera, D., Cereceda, D., Swinburne, T. D., Marian, J., and Ghoniem, N. (2016). A phenomenological dislocation mobility law for bcc metals. *Acta Materialia*, 119:123–135.

Pollak, E. and Talkner, P. (2005). Reaction rate theory: What it was, where is it today, and where is it going? *Chaos: An Interdisciplinary Journal of Nonlinear Science*, 15(2):026116.

Proville, L. and Rodney, D. (2020). Modeling the thermally activated mobility of dislocations at the atomic scale. *Handbook of Materials Modeling: Methods: Theory and Modeling*, pages 1525–1544.

Proville, L., Rodney, D., and Marinica, M. C. (2012). Quantum effect on thermally activated glide of dislocations. *Nature Materials*, 11(10):845–849.

Proville, L., Ventelon, L., and Rodney, D. (2013). Prediction of the kink-pair formation enthalpy on screw dislocations in $\alpha$-iron by a line tension model parametrized on empirical potentials and first-principles calculations. *Physical Review B - Condensed Matter and Materials Physics*, 87(14):1–8.

Rao, S. I., Woodward, C., Akdim, B., Senkov, O. N., and Miracle, D. (2021). Theory of solid solution strengthening of BCC Chemically Complex Alloys. *Acta Materialia*, 209:116758.

Rocklin, M. (2015). Dask: Parallel Computation with Blocked algorithms and Task Scheduling. In Huff, K. and Bergstra, J., editors, *Proceedings of the 14th Python in Science Conference*, pages 130–136.

Rodney, D. (2004). Molecular dynamics simulation of screw dislocations interacting with interstitial frank loops in a model FCC crystal. *Acta Materialia*, 52(3):607–614.

Rodney, D. (2007). Activation enthalpy for kink-pair nucleation on dislocations: Comparison between static and dynamic atomic-scale simulations. *Physical Review B*, 76(14):144108.

Rodney, D., Ventelon, L., Clouet, E., Pizzagalli, L., and Willaime, F. (2017). Ab initio modeling of dislocation core properties in metals and semiconductors. *Acta Materialia*, 124(2017):633–659.

Romaner, L., Ambrosch-Draxl, C., and Pippan, R. (2010). Effect of Rhenium on the Dislocation Core Structure in Tungsten. *Physical Review Letters*, 104(19):195503.

Ruda, M., Farkas, D., and Abriata, J. (2002). Interatomic potentials for carbon interstitials in metals and intermetallics. *Scripta Materialia*, 46(5):349–355.

Ryu, S., Kang, K., and Cai, W. (2011). Entropic effect on the rate of dislocation nucleation. *Proceedings of the National Academy of Sciences*, 108(13):5174–5178.

Saroukhani, S., Nguyen, L. D., Leung, K. W. K., Singh, C. V., and Warner, D. H. (2016). Harnessing atomistic simulations to predict the rate at which dislocations overcome obstacles. *Journal of the Mechanics and Physics of Solids*, 90:203–214.

Sato, Y., Swinburne, T., Ogata, S., and Rodney, D. (2021). Anharmonic effect on the thermally activated migration of {10$\bar{1}$2} twin interfaces in magnesium. *Materials Research Letters*, 9(5):231–238.

Savitzky, A. and Golay, M. J. E. (1964). Smoothing and Differentiation of Data by Simplified Least Squares Procedures. *Analytical Chemistry*, 36(8):1627–1639.

Schoeck, G. and Seeger, A. (1959). The flow stress of iron and its dependence on impurities. *Acta Metallurgica*, 7(7):469–477.

Schultz, H. (1968). Point defects in body-centered cubic transition metals. *Materials Science and Engineering*, 3(4):189–219.

Shenoy, V. B., Miller, R., Tadmor, E. B., Rodney, D., Phillips, R., and Ortiz, M. (1999). An adaptive finite element approach to atomic-scale mechanics - The quasicontinuum method. *Journal of the Mechanics and Physics of Solids*, 47(3):611–642.

Shilkrot, L. E., Miller, R. E., and Curtin, W. A. (2002). Coupled Atomistic and Discrete Dislocation Plasticity. *Physical Review Letters*, 89(2).

Shilkrot, L. E., Miller, R. E., and Curtin, W. A. (2004). Multiscale plasticity modeling: Coupled atomistics and discrete dislocation mechanics. *Journal of the Mechanics and Physics of Solids*, 52(4):755–787.

Shinzato, S., Wakeda, M., and Ogata, S. (2019). An atomistically informed kinetic Monte Carlo model for predicting solid solution strengthening of body-centered cubic alloys. *International Journal of Plasticity*, 122(November 2018):319–337.

Sills, R. B., Bertin, N., Aghaei, A., and Cai, W. (2018). Dislocation networks and the microstructural origin of strain hardening. *Physical review letters*, 121(8):85501.

Song, H. and Hoyt, J. J. (2012). A molecular dynamics simulation study of the velocities, mobility and activation energy of an austenite-ferrite interface in pure Fe. *Acta Materialia*, 60(10):4328–4335.

Sovacool, B. K., Schmid, P., Stirling, A., Walter, G., and MacKerron, G. (2020). Differences in carbon emissions reduction between countries pursuing renewable electricity versus nuclear power. *Nature Energy*, 5(11):928–935.

Spitzig, W. A. and Keh, A. S. (1970). The effect of orientation and temperature on the plastic flow properties of iron single crystals. *Acta Metallurgica*, 18(6):611–622.

Starikov, S., Smirnova, D., Pradhan, T., Lysogorskiy, Y., Chapman, H., Mrovec, M., and Drautz, R. (2021). Angular-dependent interatomic potential for large-scale atomistic simulation of iron: Development and comprehensive comparison with existing interatomic models. *Physical Review Materials*, 5:63607.

Stukowski, A. (2010). Visualization and analysis of atomistic simulation data with OVITO–the Open Visualization Tool. *Modelling and Simulation in Materials Science and Engineering*, 18(1):015012.

Stukowski, A. and Albe, K. (2010). Extracting dislocations and non-dislocation crystal defects from atomistic simulation data. *Modelling and Simulation in Materials Science and Engineering*, 18(8):85001.

Stukowski, A., Bulatov, V. V., and Arsenlis, A. (2012). Automated identification and indexing of dislocations in crystal interfaces. *Modelling and Simulation in Materials Science and Engineering*, 20(8):85007.

Stukowski, A., Cereceda, D., Swinburne, T. D., and Marian, J. (2015). Thermally-activated non-Schmid glide of screw dislocations in W using atomistically-informed kinetic Monte Carlo simulations. *International Journal of Plasticity*, 65:108–130.

Suzuki, T., Takeuchi, S., and Yoshinaga, H. (1991). *Dislocation Dynamics and Plasticity*, volume 12 of *Springer Series in Materials Science*. Springer Berlin Heidelberg, Berlin, Heidelberg.

Swinburne, T. D. (2021). Uncertainty and anharmonicity in thermally activated dynamics. *Computational Materials Science*, 193(October 2020):110256.

Swinburne, T. D., Dudarev, S. L., Fitzgerald, S. P., Gilbert, M. R., and Sutton, A. P. (2013). Theory and simulation of the diffusion of kinks on dislocations in bcc metals. *Physical Review B - Condensed Matter and Materials Physics*, 87(6):1–15.

Swinburne, T. D. and Marinica, M.-C. (2018). Unsupervised calculation of free energy barriers in large crystalline systems. *Physical review letters*, 120(13):135503.

Tadmor, E. (2020). Verification Check of Dimer C1 Continuity v004, Open KIM.

Tapasa, K., Barashev, A., Bacon, D., and Osetsky, Y. (2007). Computer simulation of the interaction of carbon atoms with self-interstitial clusters in $\alpha$-iron. *Journal of Nuclear Materials*, 361(1):52–61.

Tchitchekova, D. S., Morthomas, J., Ribeiro, F., Ducher, R., and Perez, M. (2014). A novel method for calculating the energy barriers for carbon diffusion in ferrite under heterogeneous stress. *The Journal of chemical physics*, 141(3):34118.

Tipping, P. G. (2010). *Understanding and mitigating ageing in nuclear power plants: materials and operational aspects of plant life management (PLiM)*. Elsevier.

van der Giessen, E., Schultz, P. A., Bertin, N., Bulatov, V. V., Cai, W., Csányi, G., Foiles, S. M., Geers, M. G. D., González, C., Hütter, M., Kim, W. K., Kochmann, D. M., LLorca, J., Mattsson, A. E., Rottler, J., Shluger, A., Sills, R. B., Steinbach, I., Strachan, A., and Tadmor, E. B. (2020). Roadmap on multiscale materials modeling. *Modelling and Simulation in Materials Science and Engineering*, 28(4):043001.

Varvenne, C., Leyson, G., Ghazisaeidi, M., and Curtin, W. (2017). Solute strengthening in random alloys. *Acta Materialia*, 124:660–683.

Veiga, R., Perez, M., Becquart, C., Clouet, E., and Domain, C. (2011). Comparison of atomistic and elasticity approaches for carbon diffusion near line defects in $\alpha$-iron. *Acta Materialia*, 59(18):6963–6974.

Veiga, R. G., Becquart, C. S., and Perez, M. (2014). Comments on "atomistic modeling of an Fe system with a small concentration of C". *Computational Materials Science*, 82:118–121.

Veiga, R. G., Goldenstein, H., Perez, M., and Becquart, C. S. (2015). Monte Carlo and molecular dynamics simulations of screw dislocation locking by Cottrell atmospheres in low carbon Fe-C alloys. *Scripta Materialia*, 108:19–22.

Veiga, R. G. A., Perez, M., Becquart, C. S., and Domain, C. (2013). Atomistic modeling of carbon Cottrell atmospheres in bcc iron. *Journal of Physics: Condensed Matter*, 25(2):025401.

Ventelon, L. (2008). *Simulation ab initio des coeurs de dislocation vis dans le fer*. PhD thesis, Université Claude Bernard Lyon 1.

Ventelon, L., Lüthi, B., Clouet, E., Proville, L., Legrand, B., Rodney, D., and Willaime, F. (2015). Dislocation core reconstruction induced by carbon segregation in bcc iron. *Physical Review B - Condensed Matter and Materials Physics*, 91(22):1–5.

Ventelon, L. and Willaime, F. (2007). Core structure and Peierls potential of screw dislocations in $\alpha$-Fe from first principles: cluster versus dipole approaches. *Journal of computer-aided materials design*, 14(1):85–94.

Ventelon, L., Willaime, F., Clouet, E., and Rodney, D. (2013). Ab initio investigation of the Peierls potential of screw dislocations in bcc Fe and W. *Acta Materialia*, 61(11):3973–3985.

Vineyard, G. H. (1957). Frequency factors and isotope effects in solid state rate processes. *Journal of Physics and Chemistry of Solids*, 3(1-2):121–127.

Vítek, V., Perrin, R. C., and Bowen, D. K. (1970). The core structure of ½(111) screw dislocations in b.c.c. crystals. *Philosophical Magazine*, 21(173):1049–1073.

Wang, Y., Wang, X., Li, Q., Xu, B., and Liu, W. (2019). Atomistic simulations of carbon effect on kink-pair energetics of bcc iron screw dislocations. *Journal of Materials Science*, 54(15):10728–10736.

Wang, Y.-J., Ishii, A., and Ogata, S. (2013). Entropic effect on creep in nanocrystalline metals. *Acta materialia*, 61(10):3866–3871.

Warner, D. H. and Curtin, W. A. (2009). Origins and implications of temperature-dependent activation energy barriers for dislocation nucleation in face-centered cubic metals. *Acta Materialia*, 57(14):4267–4277.

Warner, E. S. and Heath, G. A. (2012). Life Cycle Greenhouse Gas Emissions of Nuclear Electricity Generation. *Journal of Industrial Ecology*, 16(SUPPL.1):S73–S92.

Waseda, O., Veiga, R. G., Morthomas, J., Chantrenne, P., Becquart, C. S., Ribeiro, F., Jelea, A., Goldenstein, H., and Perez, M. (2017). Formation of carbon Cottrell atmospheres and their effect on the stress field around an edge dislocation. *Scripta Materialia*, 129:16–19.

Wigner, E. (1938). The transition state method. *Transactions of the Faraday Society*, 34:29–41.

Wilde, J., Cerezo, A., and Smith, G. D. W. (2000). Three-dimensional atomic-scale mapping of a Cottrell atmosphere around a dislocation in iron. *Scripta Materialia*, 43(1):39–48.

Woodward, C. and Rao, S. I. (2002). Flexible Ab Initio Boundary Conditions: Simulating Isolated Dislocations in bcc Mo and Ta. *Physical Review Letters*, 88(21):216402.

Yelon, A., Movaghar, B., and Crandall, R. S. (2006). Multi-excitation entropy: its role in thermodynamics and kinetics. *Reports on Progress in Physics*, 69(4):1145.

Zamzamian, S. M., Hossein Feghhi, S. A., and Samadfam, M. (2019). A study on the mobility of 12⟨111⟩{01¯1} edge dislocation in low-carbon $\alpha$-Fe and its interactions with damage cascade: On picosecond time scale using molecular dynamics simulations. *Journal of Nuclear Materials*, 527:1–13.

Zepeda-Ruiz, L. A., Stukowski, A., Oppelstrup, T., Bertin, N., Barton, N. R., Freitas, R., and Bulatov, V. V. (2021). Atomistic insights into metal hardening. *Nature materials*, 20(3):315–320.

Zhang, X., Grabowski, B., Hickel, T., and Neugebauer, J. (2018). Calculating free energies of point defects from ab initio. *Computational Materials Science*, 148:249–259.

Zhao, J. Z., De, A. K., and De Cooman, B. C. (2000). Kinetics of Cottrell atmosphere formation during strain aging of ultra-low carbon steels. *Materials Letters*, 44(6):374–378.

Zhao, Y., Dezerald, L., and Marian, J. (2019). Electronic Structure Calculations of Oxygen Atom Transport Energetics in the Presence of Screw Dislocations in Tungsten. *Metals*, 9(2):252.

Zhao, Y., Dezerald, L., Pozuelo, M., Zhou, X., and Marian, J. (2020). Simulating the mechanisms of serrated flow in interstitial alloys with atomic resolution over diffusive timescales. *Nature Communications*, 11(1):1–8.

Zhao, Y. and Marian, J. (2018). Direct prediction of the solute softening-to-hardening transition in W-Re alloys using stochastic simulations of screw dislocation motion. *Modelling and Simulation in Materials Science and Engineering*, 26(4).

Zhu, T., Li, J., Samanta, A., Leach, A., and Gall, K. (2008). Temperature and strain-rate dependence of surface dislocation nucleation. *Physical Review Letters*, 100(2):25502.